Jordan Journal of Mechanical and Industrial Engineering (JJMIE)

JJMIE is a high-quality scientific journal devoted to fields of Mechanical and Industrial Engineering. It is published by Hashemite University in corporation with the Jordanian Scientific Research Support Fund.

SUBMISSION ADDRESS:

Dr. Ali M. Jawarneh, Editor-in-Chief
Jordan Journal of Mechanical & Industrial Engineering,
Hashemite University,
PO Box 330127, Zarqa, 13133 , Jordan
E-mail: jjmie@hu.edu.jo

Hashemite Kingdom of Jordan

Hashemite University

Jordan Journal of Mechanical and Industrial Engineering

JJMIE

An International Peer-Reviewed Scientific Journal

Financed by Scientific Research Support Fund

http://jjmie.hu.edu.jo/

ISSN 1995-6665

Jordan Journal of Mechanical and Industrial Engineering (JJMIE)

JJMIE is a high-quality scientific journal devoted to fields of Mechanical and Industrial Engineering. It is published by The Jordanian Ministry of Higher Education and Scientific Research in corporation with Hashemite University.

Introduction: The Editorial Board is very committed to build the Journal as one of the leading international journals in mechanical and industrial engineering sciences in the next few years. With the support of the Ministry of Higher Education and Scientific Research and Jordanian Universities, it is expected that a heavy resource to be channeled into the Journal to establish its international reputation. The Journal's reputation will be enhanced from arrangements with several organizers of international conferences in publishing selected best papers of the conference proceedings.

Aims and Scope: *Jordan Journal of Mechanical and Industrial Engineering* (JJMIE) is a refereed international journal to be of interest and use to all those concerned with research in various fields of, or closely related to, mechanical and industrial engineering disciplines. *Jordan Journal of Mechanical and Industrial Engineering* aims to provide a highly readable and valuable addition to the literature which will serve as an indispensable reference tool for years to come. The coverage of the journal includes all new theoretical and experimental findings in the fields of mechanical and industrial engineering or any closely related fields (Materials, Manufacturing, Management, Design, Thermal and Fluid, Energy, Control, Mechatronics, and Biomedical). The journal also encourages the submission of critical review articles covering advances in recent research of such fields as well as technical notes.

Guide for Authors

Manuscript Submission:
High-quality submissions to this new journal are welcome now and manuscripts may be either submitted online or email.

Online: For online and email submission upload one copy of the full paper including graphics and all figures at the online submission site, accessed via http://jjmie.hu.edu.jo. The manuscript must be written in MS Word 2010 Format. All correspondence, including notification of the Editor's decision and requests for revision, takes place by e-mail and via the Author's homepage, removing the need for a hard-copy paper trail.

Submission address and contact:
Dr. Ali M. Jawarneh
Editor-in-Chief
Jordan Journal of Mechanical & Industrial Engineering,
Hashemite University,
PO Box 330127, Zarqa, 13115, Jordan
E-mail: jjmie@hu.edu.jo

Types of contributions*:* Original research papers and Technical reports

Corresponding author: Clearly indicate who is responsible for correspondence at all stages of refereeing and publication, including post-publication. Ensure that telephone and fax numbers (with country and area code) are provided in addition to the e-mail address and the complete postal address. Full postal addresses must be given for all co-authors.

Original material: Submission of an article implies that the work described has not been published previously (except in the form of an abstract or as part of a published lecture or academic thesis), that it is not under consideration for publication elsewhere, that its publication is approved by all authors and that, if accepted, it will not be published elsewhere in the same form, in English or in any other language, without the written consent of the Publisher. Authors found to be deliberately contravening the submission guidelines on originality and exclusivity shall not be considered for future publication in this journal.

Withdrawing: If the author chooses to withdraw his article after it has been assessed, he shall reimburse JJMIE with the cost of reviewing the paper.

Manuscript Preparation:

General: Editors reserve the right to adjust style to certain standards of uniformity. Original manuscripts are discarded after publication unless the Publisher is asked to return original material after use. Please use MS Word 2010 for the text of your manuscript.

Structure: Follow this order when typing manuscripts: Title, Authors, Authors title, Affiliations, Abstract, Keywords, Introduction, Main text, Conclusions, Acknowledgements, Appendix, References, Figure Captions, Figures and then Tables. Please supply figures imported into the text AND also separately as original graphics files. Collate acknowledgements in a separate section at the end of the article and do not include them on the title page, as a footnote to the title or otherwise.

Text Layout: Use 1.5 line spacing and wide (3 cm) margins. Ensure that each new paragraph is clearly indicated. Present tables and figure legends on separate pages at the end of the manuscript. If possible, consult a recent issue of the journal to become familiar with layout and conventions. All footnotes (except for table and corresponding author footnotes) should be identified with superscript Arabic numbers. To conserve space, authors are requested to mark the less important parts of the paper (such as records of experimental results) for printing in smaller type. For long papers (more than 4000 words) sections which could be deleted without destroying either the sense or the continuity of the paper should be indicated as a guide for the editor. Nomenclature should conform to that most frequently used in the scientific field concerned. Number all pages consecutively; use 12 or 10 pt font size and standard fonts.

Corresponding author: Clearly indicate who is responsible for correspondence at all stages of refereeing and publication, including post-publication. The corresponding author should be identified with an asterisk and footnote. Ensure that telephone and fax numbers (with country and area code) are provided in addition to the e-mail address and the complete postal address. Full postal addresses must be given for all co-authors. Please consult a recent journal paper for style if possible.

Abstract: A self-contained abstract outlining in a single paragraph the aims, scope and conclusions of the paper must be supplied.

Keywords: Immediately after the abstract, provide a maximum of six keywords (avoid, for example, 'and', 'of'). Be sparing with abbreviations: only abbreviations firmly established in the field may be eligible.

Symbols: All Greek letters and unusual symbols should be identified by name in the margin, the first time they are used.

Units: Follow internationally accepted rules and conventions: use the international system of units (SI). If other quantities are mentioned, give their equivalent in SI.

Maths: Number consecutively any equations that have to be displayed separately from the text (if referred to explicitly in the text).

References: All publications cited in the text should be presented in a list of references following the text of the manuscript.

Text: Indicate references by number(s) in square brackets in line with the text. The actual authors can be referred to, but the reference number(s) must always be given.

List: Number the references (numbers in square brackets) in the list in the order in which they appear in the text.

Examples:
Reference to a journal publication:
[1] M.S. Mohsen, B.A. Akash, "Evaluation of domestic solar water heating system in Jordan using analytic hierarchy process". Energy Conversion & Management, Vol. 38 (1997) No. 9, 1815-1822.

Reference to a book:
[2] Strunk Jr W, White EB. The elements of style. 3rd ed. New York: Macmillan; 1979.

Reference to a conference proceeding:
[3] B. Akash, S. Odeh, S. Nijmeh, "Modeling of solar-assisted double-tube evaporator heat pump system under local climate conditions". 5th Jordanian International Mechanical Engineering Conference, Amman, Jordan, 2004.

Reference to a chapter in an edited book:
[4] Mettam GR, Adams LB. How to prepare an electronic version of your article. In: Jones BS, Smith RZ, editors. Introduction to the electronic age, New York: E-Publishing Inc; 1999, p. 281-304

Free Online Color : If, together with your accepted article, you submit usable color and black/white figures then the journal will ensure that these figures will appear in color on the journal website electronic version.

Tables: Tables should be numbered consecutively and given suitable captions and each table should begin on a new page. No vertical rules should be used. Tables should not unnecessarily duplicate results presented elsewhere in the manuscript (for example, in graphs). Footnotes to tables should be typed below the table and should be referred to by superscript lowercase letters.

Notification: Authors will be notified of the acceptance of their paper by the editor. The Publisher will also send a notification of receipt of the paper in production.

Copyright: All authors must sign the Transfer of Copyright agreement before the article can be published. This transfer agreement enables Jordan Journal of Mechanical and Industrial Engineering to protect the copyrighted material for the authors, but does not relinquish the authors' proprietary rights. The copyright transfer covers the exclusive rights to reproduce and distribute the article, including reprints, photographic reproductions, microfilm or any other reproductions of similar nature and translations.

Proof Reading: One set of page proofs in MS Word 2010 format will be sent by e-mail to the corresponding author, to be checked for typesetting/editing. The corrections should be returned within **48 hours**. No changes in, or additions to, the accepted (and subsequently edited) manuscript will be allowed at this stage. Proofreading is solely the author's responsibility. Any queries should be answered in full. Please correct factual errors only, or errors introduced by typesetting. Please note that once your paper has been proofed we publish the identical paper online as in print.

Author Benefits:

No page charges: Publication in this journal is free of charge.

Free offprints: One journal issues of which the article appears will be supplied free of charge to the corresponding author and additional offprint for each co-author. Corresponding authors will be given the choice to buy extra offprints before printing of the article.

JJMIE

Volume 12 Number 1, June. 2018
ISSN 1995-6665

Jordan Journal of Mechanical and Industrial Engineering

JJMIE

Volume 12 Number 1, June. 2018
ISSN 1995-6665
Pages 1 - 6

Jordan Journal of Mechanical and Industrial Engineering

Techno-Economic Analysis of a Concentrated Solar Polygeneration Plant in Jordan

S. Kiwan[a,*], L. Venezia[b], F. M. Montagnino[b], F. Paredes[b], R. Damseh[c]

[a] *Mechanical Engineering Department, Jordan University of Science and Technology, Irbid 22110, Jordan.*
[b] *Consorzio ARCA, Palermo 90128, Italy*
[c] *Mechanical Engineering Department, Albalqa Applied University, Al Huson College, Irbid, Jordan*

Received 30 Dec 2016 *Accepted 21 June 2018*

Abstract

A polygeneration concentrated solar plant is designed and analyzed to investigate its techno-economic performance, and to investigate the different components that can be effectively combined in zero or positive energy districts, both in built and rural environments. The design was based on the results of an energy audit performed on the site which showed the prevalence of the summer cooling demand. The design is characterized by using Parabolic Trough Collectors as solar collecting technology installed on the roof of a building. The installation constraints, such as the size and the orientation of the available space, have driven the design of the plants and the selection of the possible storage and conversion technologies. The design includes a steam circuit that feeds a steam turbine manufactured at a very small scale, solar driven absorption chiller, direct heating system and water distillation unit. Conclusions are drawn and documented about the potential impact of solar polygeneration in the Mediterranean solar belt and the future development of the involved technologies. Results showed that the polygeneration plant has a Utilization Factor of 0.66, while, the economics of such technology needs improvement as indicated by the Benefit-Cost-Ratio (BCR) of 0.62 due to the high cost of the small-scale components of this technology.

Keywords: *CSP, Polygeneration, Energy Audit, Renewable Energy.*

1. Introduction

In the framework of the STS-Med Project, an EU-funded project by European Commission under the ENPI CBCMED program, four solar polygenerative plants have been designed to be connected with public buildings in four different Mediterranean countries, respectively Italy, Cyprus, Egypt, and Jordan. All the plants are characterized by an innovative application of concentrating solar collectors with the aim to generate a balanced answer to the energy demanded by the buildings: electricity, heat and cold, as well as other energy-driven services like the supply of purified water.

Energy demand for cooling and heating requirements has increased significantly over the last years. Global space cooling energy consumption increased by 60% in the period between 2000 and 2010 reaching 4% of global consumption in 2010 [1]. On the other hand, heat consumption accounts for more than 50% of the global consumption [2].Therefore, alternative heating and cooling systems derived from renewable or recovered energy have driven the interest of many researchers worldwide. The generation of electricity using renewable energy technology may cause problems to the electricity grid [3], thus, thinking of generating essential energy demand is a solution that avoids the pressuring use of national electricity grid.

Many researchers [4-8] have carried out experimental and theoretical studies of using CS technology for Solar Heating Cooling (SHC) systems and/or power generation. Sakhriehaet al. [9], for example, carried out modeling investigation for the hybridization of CS technology with geothermal energy to produce electricity using organic Rankine cycle. For this paper, the work of [9] and [11] is of interest. They used the concentrated energy for polygeneration. Absorption heating and cooling systems were studied more than any other systems. These systems have many advantages over other refrigeration systems [11]: such as quiet operation, high reliability, long service life, meeting the variable load efficiently, minimum mechanical moving parts, no lubricants needed, and no atmosphere-damaging refrigerants .There are not many tools available for accurate dimensioning and evaluating the solar thermal contribution to the total energy requirements. The dynamic simulation tool is used by

* Corresponding author e-mail: kiwan@just.edu.jo.

many researchers [12-14]. Fong et al. [15] made a theoretical, comparative study of five different solar cooling systems; Solar electrical compression, solar mechanical, solar absorption, solar adsorption and solid desiccant cooling system. The results show that solar electrical compression alongside solar absorption system has the best performance results. Moreover, the advantages of two-stage systems over other systems are investigated by [17]. They concluded that the cooling system could work steadily in spite of unsteady solar input, lower generator input, and outlet temperature. However, they demand higher temperature heat.

The primary goal of using poly-generation systems is to maximize the utilization of the collected solar energy to the maximum possible extent. However, there are several challenges facing this approach: those challenges are mainly economical; first of all, the cost of the components of the systems are still high. Second, no available commercial technology for some components of the system, and the third challenge is to match the building load with the system output especially in winter and night which needs special treatment. The concept of storage using the innovative solution presented by [17] is applied.

In this paper, the case of designing and simulating a small scale poly-generation system to match the load for a building in Italy is presented. The techno-economic performance indicators are presented.

2. Analysis

To assess the impact of CS power plant from technical and economic points of view, we need to define technical and economic indicators. The concept of utilization factor is used to assess the technical performance of this poly-generation plant. Since the main idea of the multi-generation is to maximize the utilization of the incident solar energy on the solar field, it will be convenient to use the utilization factor which basically measures the amount of converted useful energy relative to the available energy from the source. It is defined as the ratio of the useful annual energy (thermal and electrical) produced by the system to the total annual incident energy on the system. The useful energy includes the energy produced for heating, cooling, water desalination, and electricity generation. That is

$$\varepsilon = \frac{Useful\ Energy\ Collected\ per\ year}{Annual\ incident\ solar\ irradiation\ on\ the\ solar\ field} \quad (1)$$

$$\varepsilon = \frac{E_h + E_c + E_{ele} + E_w}{\overline{DNI}\ x\ A} \quad (2)$$

where, DNI is the annual average direct normal solar irradiation in kWh/m^2/year incident at the location. The energy used for water desalination is calculated as

$$E_w = M * \left(h_{fg} + cp\ \Delta T\right) / 3600 \quad (3)$$

where, M is the total mass of water desalinated per year (kg/year), h_{fg} (2200 kJ/kg) is the specific enthalpy for vaporization of water at ambient conditions, and ΔT=(100-20)=80 °C.

The energy output of the heating system, E_h, is calculated as

$$E_h = \sum_{i=1}^{N} \dot{m}\, c_p (T_i - T_o) \quad (4)$$

where, N is the number of hours in the year when the heating system is operating. m is the average hourly flow rate of the fluid conveying heat to space in (kg/s) and T_i is the hourly average of the temperature of the fluid entering the heating coil and T_o is the hourly average temperature of the fluid leaving the heating coil.

The energy output of the cooling system, E_c, is calculated as

$$E_c = \sum_{i=1}^{NN} \dot{m}\, c_p (T_{co} - T_{ci}) \quad (5)$$

where, NN is the number of hours in the year when the cooling system is operating. $\dot{m}$, is the average hourly flow rate of the fluid conveying heat to space (kg/s), and T_{ci} is the hourly average of the temperature of the fluid entering the cooling coil and T_{co} is the hourly average temperature of the fluid leaving the cooling coil. The total annual energy from the electricity generation system is E_{ele} in kWh.

The variation of the types of energy harvested from the CS poly-generation systems makes the benefit-cost ratio (BCR) as a comprehensive and straightforward indicator. Benefit-cost ratio is the ratio of the accumulated present value of all the benefits to the accumulated present value of all costs, including the initial investment. The BCR is expressed as:

$$BCR = \frac{B_A \left[\frac{(1+I)^n - 1}{I(1+I)^n} \right]}{C_I \left[1 + m \left(\frac{(1+I)^n - 1}{I(1+I)^n} \right) \right]} \quad (6)$$

where, B_A is the sum of the annual benefits of the system (in Euro), I the real rate of discount, n is the lifetime of the system, C_I is the initial investment of the system, and m is the cost of annual O&M as a percentage of the initial system cost. Now, if BCR is higher than one, then the project is asuccess.

3. CS Plant Description

The plant under consideration is as shown in Fig.1. It is merelya parabolic trough for space heating, cooling, water distillation, and power generation. The solar thermal system loop consists mainly of the: concentrated solar collector of type linear parabolic trough Soltigua concentrating Solutions. The collector model is aPTMx-36 model (net collecting Area = 164 m2) of a nominal capacity of 100 kWth. The Heat Transfer Fluid is the thermal oil"Seriola Eta"by TOTAL. The nominal temperature of the oil at receiver inlet is 200 C, and at receiver outlet is 240 C. The collected heat from the solar field is extracted from the thermal oil in a counter flow heat exchanger and delivered to fan coil units to provide heating to the designated space in winter. While in summer, the extracted heat from the solar field through the thermal oil is used to drive an absorption chiller of 17.2 kW.

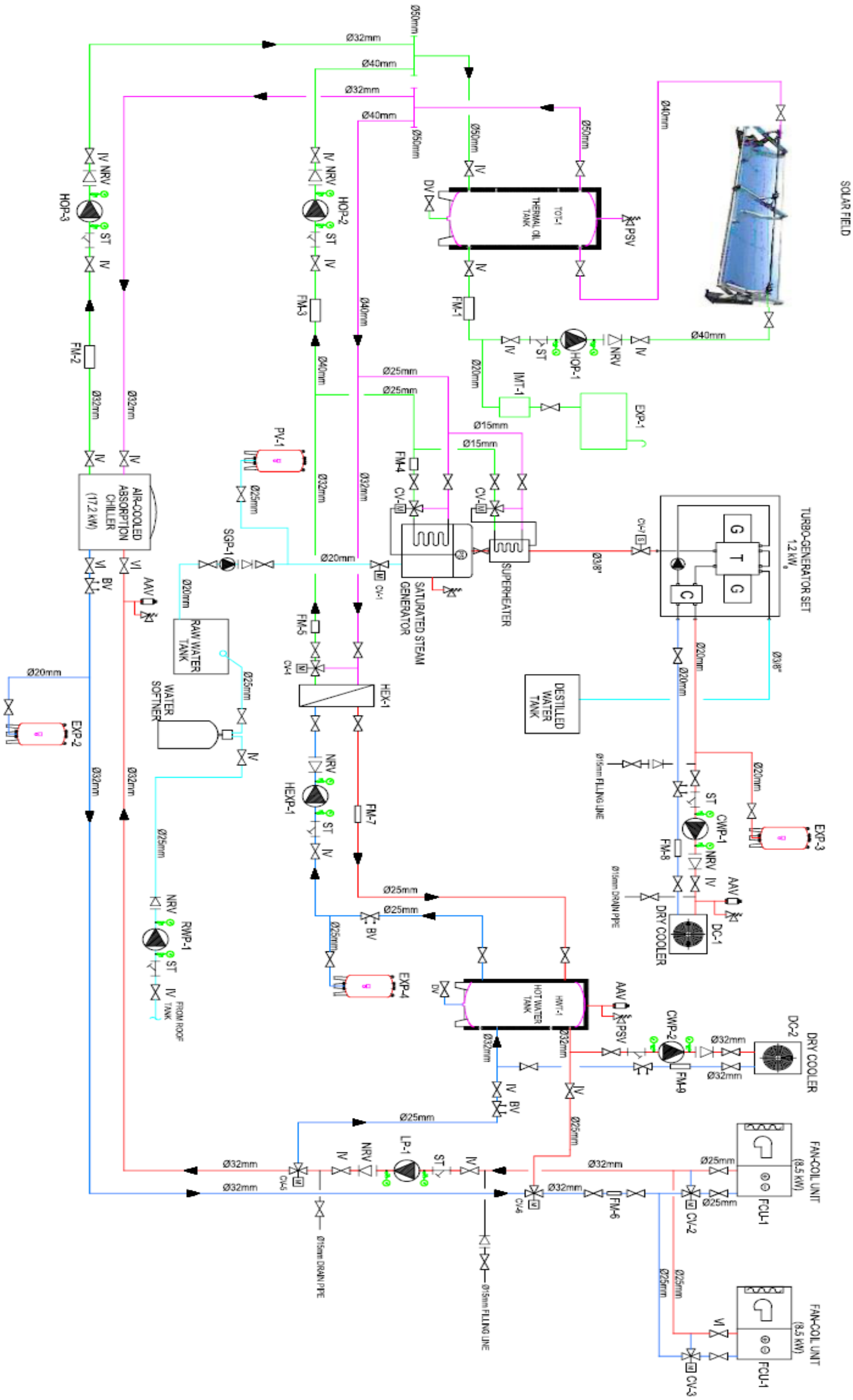

Figure 1: System Layout of the CS Polygeneration Plant in Jordan

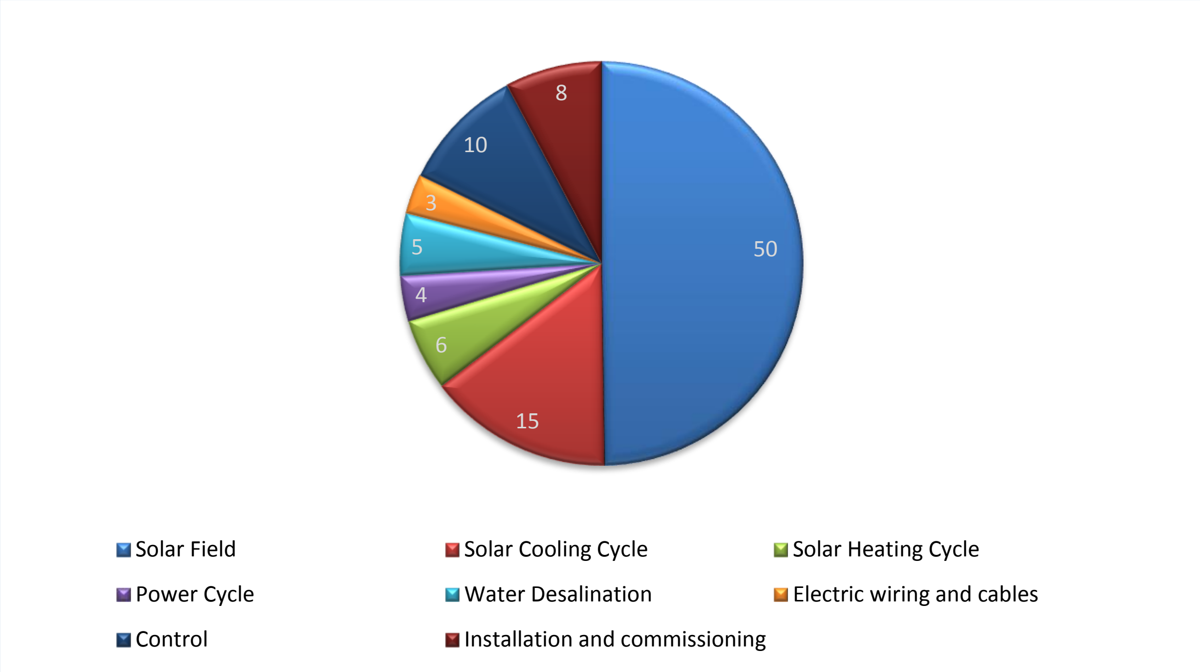

Figure 2: Percentage of cost for the CS-Polygeneration system in Jordan's pilot project

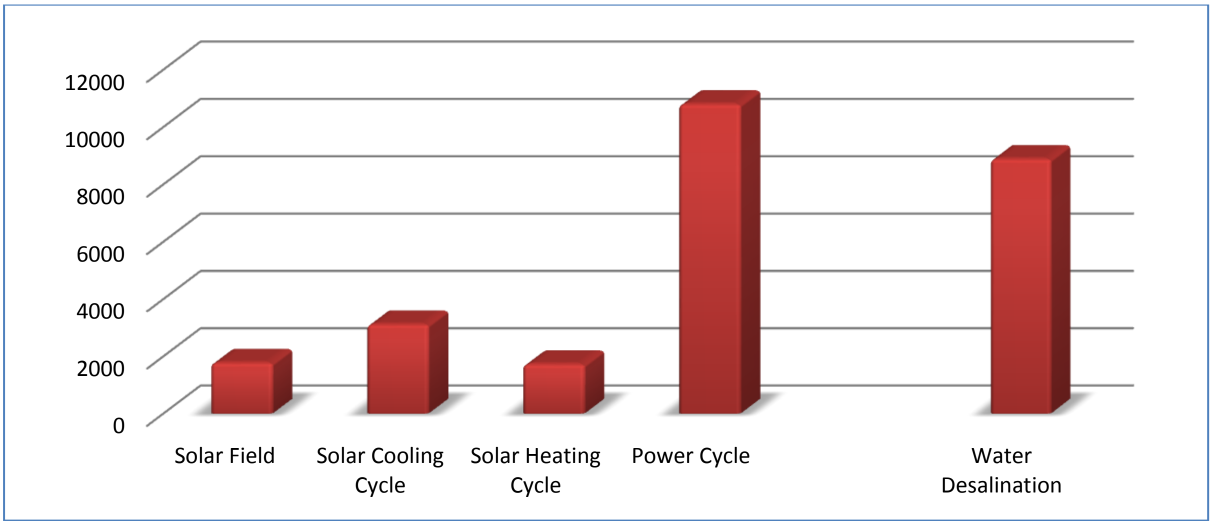

Figure 3. Normalized Cost (€ per Unit Output) for system components in Jordan's project

The chiller is Robur with inlet oil temperature at 240°C, and outlet temperature at 190 °C. It is a single effect Ammonia absorption chiller with COP of 0.5. Part of the hot thermal oil is extracted to generate steam at 200 °C, 5.2 bar through a locally made steam generator. The generated steam is fed to a small steam Turbine of 1.2 kW nominal power output. The condensate of the steam leaving the turbine is used as adistillate at a rate of 18 kg/hr.

The cost of subsystems is evaluated and analyzed. Table 1 shows the summary of the cost based on subsystems/components classified according to the nature of the energy outputs from the system.

Table 1: Breakdown of the cost of the pilot project in Jordan

Sub System/ Component	Size	Unit	Cost in€ per unit size	% Share
Solar Field	100	kWth	1778	50
Solar Cooling Cycle	17	kW	3120	15
Solar Heating Cycle	12	kW	1726	6
Power Cycle	5	kWe	6148	9
Electric wiring and cables	100	kWth	114	3
Control	100	kWth	358	10
Installation and commissioning*	100	kWth	278	8

*Estimated values

Figure 2 shows the pie chart of the distribution of the percentage of system cost. It is clear from this figure and the above table that the solar field cost 50% of the project, while, the heating system cost is about 6%. It is worth mentioning that most of heating system cost goes to the fan coil units. These unit were not available in the space. Moreover, the unit cost of the solar cooling system per kW is high compared to other components. Its cost is almost 6 times higher than conventional cooling systems such as vapor compression AC units. In spite of this, the cost of the solar chiller and the dry cooler compromise the main components of the solar cooling system, as shown in Fig. (3),in which their cost share is 15 %, as shown in Table 2, and they cost 3120 Euro/kW.Of particular interest in Fig. 3 is the cost of the energy block to produce electricity. The use of steam engine or steam turbine at small scale is unconventional in the market. This made the unit cost is very high. Figure 3 shows the normalized cost of power machine is 6148 Euro per kW. This causes a constraint to the required size of the power production unit in the polygenerative system.

4. System Output

The performance of the system and its components are simulated using TRNSYS where the weather data for the site is (Irbid, Jordan).The model equations for each component or subsystem were taken from manufacturers. The results are listed in Table 3. The output data in this table is calculated using the Eqns. (3-5) and assuming the COP of conventional A/C is 3. The real discount rate of 5%, and the annual operation and maintenance cost 2% of the initial cost. The lifetime of the system is assumed to be 20 years. The cost of electricity is sold to the facility at 0.25 euro/kWh (large consumer Tariff). The results of the simulation indicated the outputs as listed in Table 3 below.

Table 3: Energy and benefits extracted from the system in one year

Sub System	Quantity output/year	Unit	Annual Output kWh_{th}	Annual Benefit (€/year)
Cooling	2618	kWh_{th}	2618	655
Heating	12240	kWh_{th}	12240	3060
Distilled water	360	m^3	220500	18000
Electricity	1825	kWh_{elec}	1825	456
		Total	**237183**	**22171**

Based on the data given in the above table and applying Eqns. (1) and (6) respectively, it is found that the utilization factor is ε= 0.66 and the Benefit Cost Ratio (BCR)= 0.62.

Figure 4 shows that the income drawn from selling distilled water contributes about 80% to the total Benefits of the system.

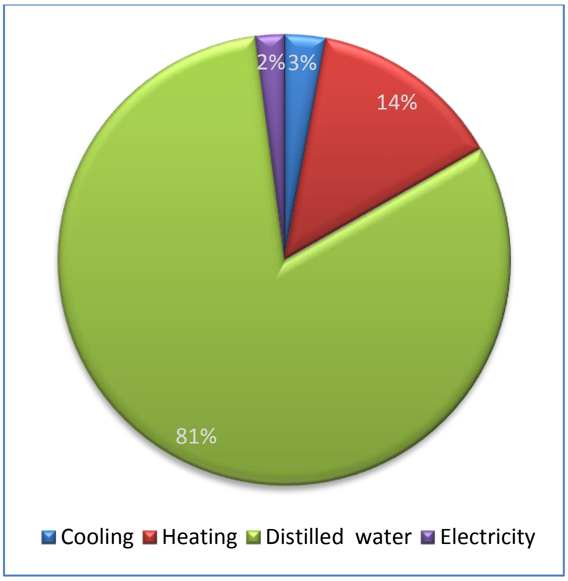

Figure 4: Percentage share of system benefits for Jordan's Pilot Project

5. Conclusion

The STS-Med Jordan pilot project was designed to demonstrate the ability to utilize solar poly-generation systems using CS technology. The project will also serve as a living laboratory to students at the college. On the other hand, the results indicated that the proposed plant would provide the heating and cooling load for the auditorium at the building. The system will cover part of the electric load. It will also provide a considerable amount of distilled water.

The results show that 66% of the incident solar energy at the solar field will be converted into different forms of useful energy. However, the cost-benefit ratio is lower than one. The percentage of the cost of the solar field reaches 50% of the total cost of the plant. Thus, to make such system economically feasible in the future, the cost of the solar field must be reduced at least by 25%. This should be an interesting perspective for the development of polygenerative solar fields in the Mediterranean area. Furthermore, it is found that 81% of the benefits of the studied plant come from water distillation. This is also an interesting future perspective of such plants.

Acknowledgment

The authors would like to acknowledge the European Commission: ENPI CBCMED program for supporting the project STS-Med under which this work has been conducted.

References

[1] The report, "Transition to Sustainable Buildings: Strategies and Opportunities to 2050," OECD/IEA, Paris, 2013.

[2] The report "Heating without Global Warming: Market Developments and Policy Considerations for Renewable Heat," OECD/IEA, Paris, 2014.

[3] T. Abu Dyak, E. O. Abu-Lehyeh, S. Kiwan, "Assessment of Implementing Jordan's Renewable Energy Plan on the Electricity Grid," JJMIE, Volume 11, No. 2, 2017, 113 -119.

[4] D.S. Kim,C.A. Infante Ferreira, "Solar refrigeration options – a state-of-the-art review," international journal of refrigeration, Vol. 3 , 2008, 3-15.

[5] H.M. Henning, "Solar assisted air conditioning of buildings – an overview," Applied Thermal Engineering, Vol. 27, 2007, 1734–1749.

[6] W. Saman, M. Krause, K. Vajen, "Solar Cooling Technologies: Current Status and Recent Developments," in Proceedings of 42nd ANZSES Conference Solar, Perth,Australia , 2004.

[7] Neuhäeuser, "Polygeneration using concentrating solar thermal power", Acts of SolarPACES, 2009

[8] Ababneh, "Energy Conservation Using a Double-effect Absorption Cycle Driven by Solar Energy and Fossil Fuels", JJMIE, Volume 5, No. 3, 2011, 213 - 219

[9] Sakhrieha, W. Shreimb , H. Fakhruldeenb , H. Hasanb , A. Al-Salaymeh, Combined Solar-Geothermal Power Generation using Organic Rankine Cycle", Jordan Journal of Mechanical and Industrial Engineering, Vol. 10, No. 1, 2016, 1- 9.

[10] S. Vasta, A. Frazzica, A. Freni, L. Venezia, A. Buscemi, F. Paredes, F. M. Montagnino, "A concentrating – based solar cooling system for agri-food industry", Acts of 5th International Conference Solar Air-Conditioning, Germany, 2013

[11] T. L. Freeman., J. W. Mitchell,T. E. Audit, "Performance of Combined Solar Heat Pump Systems," Solar Energy, Vol. 22, No. 2, 1979, 125-135.

[12] M. Quirante, L. Valenzuela, "Dimensioning a small-sized PTC solar field for heating and cooling of a hotel in Almería (Spain)," Energy Procedia, Vol. 30, 2012, 967 – 973.

[13] Calise.F, Palombo.A, Vanoli.L, "Maximization of primary energy savings of solar heating and cooling systems by transient simulations and computer design of experiments," Applied Energy, Vol. 87, 2010, 524–540.

[14] M. Mazloumi, M. Naghashzadegan, K. Javaherdeh, "Simulation of solar lithium bromide–water absorption cooling system with parabolic trough collector," Energy Conversion and Management, Vol. 49, 2008, 2820–2832.

[15] K.F. Fong, T.T. Chow, C.K. Lee,Z. Lin, L.S. Chan, "Comparative study of different solar Cooling systems for buildings in subtropical city," Solar Energy, vol. 84, 2010, 227–244.

[16] V. Mittal, K.S. Kasana, N.S. Thakur, "The study of solar absorption air-conditioning systems," Journal of Energy in Southern Africa, Vol. 16, No.4, 2005.

[17] W. Gaggioli, F. Fabrizi, F. Fontana, P. Tarquini, L. Rinaldi, "An innovative concept of a thermal energy storage system based on the single tank configuration using stratifying Molten Salts as both HSM and HTF and with an integrated Steam Generator," Acts of SolarPACES2013 conference.

JJMIE

Jordan Journal of Mechanical and Industrial Engineering

Volume 12 Number 1, June. 2018
ISSN 1995-6665
Pages 7 - 15

Numerical Modeling of Hydrogen Embrittlement of a Hollow Cylinder

Assia A. Lakhdari[a,*], Ilya I.Ovchinnikov[b], Aissa Seddak[a], Igor G. Ovchinnikov[b]

[a] Department of Mechanical Engineering, Université des Sciences et de la Technologie d'Oran Mohamed Boudiaf , USTO-MB, BP 1505 El M'naouer, 31000 Oran, Algeria

[b] Department of Transportation Constructions, Saratov State Technical University Gagarin Y.A., Russia

Received 27 Nov2017 Accepted 21 June 2018

Abstract

In this work, the behavior of a thick-walled tube in a hydrogenated medium was simulated. The study focused on the deformation and the rupture of the hydrogenated material at ambient temperature, taking into account the appearance of heterogeneity of the mechanical properties. For this, the influence of stress states on mechanical properties and diffusion in materials has been taken into account. During the development of the methodology of calculation of the thick wall tube, the work of the structure was presented in the form of three successive stages. Numerical simulation shows that the most dangerous case is the simultaneous action of hydrogen and the charge on the inner surface of the wall of the hollow cylinder due to the fact that the combination of the action of constraints of traction and hydrogen leads to an intense degradation of the material. It should be noted that such a case of the influence of charge and hydrogen is most typical for real conditions.

Keywords: *hydrogen; embrittlement; degradation; diffusion; stress state; mechanical properties; durability*.

1. Introduction

The hydrogenated environment has a destructive impact on the materials and structures. Furthermore, hydrogen can act on the structures at high temperatures and pressures, as well as at normal temperatures which are generally called low [1-7].

During its interaction with the structure materials, the hydrogen at high temperatures and pressures, can cause what is known as corrosion by hydrogen, during which decarburization takes place of section part, leading thus to decreasing the tensile strength, modulus of elasticity, the deformation pattern of transverse deformation coefficient, creep curves, the plastic limit and the limit of deformation. Following these changes, the stress-strain state in the structures changes and reduces longevity. The different experimental data on the effect of hydrogen at high temperature are given by [8-11].

To date, a number of deformation and fracture models of structures in the conditions of corrosion with hydrogen at high temperature has been developed; the review and analysis can be found in publications [12-15].

Unlike hydrogen at high temperature, hydrogen at low temperatures has a selective effect on the material structures so that the mechanical properties are not changed in the compressed regions, but they change in the stretched areas. However, the magnitude of the variation depends on the hydrogen concentration and the stress state diagram in such point. For only one and the same figure of the stress state, a high hydrogen concentration causes a large variation in mechanical properties, and for only one and the same concentration of hydrogen, a more rigid stress state diagram causes a significant mechanical properties change.

The review and analysis of experimental data on the hydrogenation effect at low temperature on the mechanical properties of materials that cause stress corrosion cracking, are presented in the work [16, 17].

The analysis shows the following possible cases of the hydrogen interaction with metals:

- During electrochemical processes at low-temperature, when hydrogen atoms are adsorbed- the surface of the structures become absorbed by the metal (this mechanism occurs in particular cases, such as hydrogenation etching, degreasing and galvanizing)
- During corrosion, when there is a chemical release of hydrogen, then it happens to penetrate into the metal;
- By direct contact of metal with hydrogen or hydrogen media where hydrogen enters the metal under its own pressure (many accidents known in the petroleum industry, due to the extraction of oil with high content hydrogen, which led to material losses and sometimes can cause losses of human lives).

* Corresponding author e-mailamina.lakhdari@univ-usto.dz.

Such a negative effect of hydrogen on the mechanical properties of metals leads for the need to take this effect into account in the design and calculation of structures; this will ensure better security for structures work. To date, there have been a number of developed models for the structure calculation subjected to hydrogenation. In the research done by [16] a method of calculating a cylindrical vessel has been proposed, taking into account the effect of hydrogen, the state of stress and temperature on the metal plasticity.

The authors [17] have developed a model of the hydrogen influence, taking into account the effect of hydrogen on the structure stretched zone as a function of the dependence of the mechanical properties of the hydrogen concentration. In the investigation [16] a model was proposed for the interaction of structures with a hydrogen environment, taking into account not only the influence of the sign, but also of the state of stress diagram on kinetics of change the properties of the structure during its interaction with the hydrogen. The authors of the work [17] proposed a theory of plasticity of materials exposed to hydrogen embrittlement, leading to the appearance of a different capacity for resistance of materials

In the above investigations, we tried to take into account the influence of the hydrogen concentration and the stress state diagram of material properties change, but without considering the influence of the stress state on the penetration of hydrogen in the volume of the structure.

2. Model of deformation and fracture of materials subjected to hydrogenation

When developing the models, it is important to take into consideration the following effects of the interaction of structures with hydrogen:

- The hydrogen penetrates into the structure of the activated diffusion mechanism, in which there is a diffusion of hydrogen in areas with a predominance of traction components, and optionally the extraction of hydrogen from the areas with predominantly compressive components, that is to say that the diagram of the state of stress influences the hydrogenation kinetics;
- The hydrogen penetrating into the metal leads to a deterioration in strength and plasticity according to the concentration of hydrogen, and in addition the change in mechanical properties depends on the hydrogen concentration and not of the nature of the hydrogenation process;
- The type and the state of the stress impact level on the interaction of the metal with hydrogen, in that during the predominance of compression components, the metal, and after an intensive hydrogenation retains its properties, but with a predominance of traction components, the strength and plasticity properties decrease, and in addition to the tightening of the stress state diagram, the change in properties is most important.

To develop deformation models and fracture of structures subjected to hydrogenation; an approach [17] is used, based on the systems of the examined: penetration model hydrogen, model of deformation of the material, progression model of limit state model of the constructive element.

2.1. Hydrogen permeation model in the material of the structure

The hydrogen permeation kinetics in the structure is described by the diffusion form as given in the following equation:

$$\frac{\partial C}{\partial t} = div(DgradC) \tag{1}$$

With the initial conditions and the appropriate limits see work [17].

Where: *D* is a diffusion coefficient, which is a function of local parameters; *C* is concentration; *T* is temperature; *t* is time.

To reflect the influence of the stress-strain state of the hydrogen permeability, different approaches are used.

A process of diffusion of the hydrogen has been suggested by [17], in the field of elastic stresses, which is described by the equation:

$$\frac{\partial C}{\partial t} = D\nabla^2 C - \left(\frac{DV_H}{RT}\right)\nabla C\nabla\sigma_0 - \left(\frac{DV_H}{RT}\right)C\nabla^2\sigma_0 \tag{2}$$

Where V_H – Hydrogen partial molar volume, $\sigma = (\sigma_x + \sigma_y + \sigma_z)/3$- mean stress, *R* - Gas constant.

The hydrogen equilibrium concentration C_δ in the field of elastic stresses σ_0 is determined by the expression:

$$C_\delta = C_0 \exp\left(\frac{\sigma_0 V_H}{RT}\right) \tag{3}$$

Where C_0 – equilibrium concentration of hydrogen in the absence of stress field.

In equation (2), the last two members reflect the directed broadcast hydrogen in areas with predominance of the traction component ($\sigma_0 > 0$) and the extraction of hydrogen from areas with predominance of the compression component ($\sigma_0 < 0$). For the equation (3), the initial conditions and the appropriate limits must be taken into account.

Another approach for taking into account the influence of the stress state on the hydrogen permeation is to assume that the hydrogen diffusion coefficient *D* and the hydrogen absorption limit of C_* are functions a special dimensionless parameter:

$$S = \frac{3\sigma_0}{\sigma_U} \tag{4}$$

Characterizing the pattern of the stress state, σ_u- stress intensity.

Parameter values *S* for certain patterns of the stress state are given in table 1.

Table 1: Parameter values S for certain patterns of the stress state

schema of the state of stress	biaxial compression	uniaxial compression	cisaillement	uniaxial traction	biaxial traction
S	-2	-1	0	+1	+2

The expressions for *D* and C_* are taken in the form:

$$D = D_0(1 + \alpha S^\beta) \tag{5}$$

$$C_* = C_*^0(1 + \gamma S^\delta) \tag{6}$$

D_0 and C_*^0- values of *D* and C_* in the idle state (non-constraint state), α, β, γ, δ - coefficients.

In this case, equation (1) takes the form:

$$\frac{\partial[\frac{C}{C_*(S)}]}{\partial t} = div\left(D(S)grad\left[\frac{C}{C_*(S)}\right]\right) \quad (7)$$

2.2. Material model deformation under the influence of the hydrogenation

For model elaboration, we apply the deformation theory of A. A. Iliouchine, whose basic assumptions are adjusted to reflect the influence of hydrogen:

- First hypothesis: the spherical deformation tensor is proportional to spherical stress tensor, and the coefficient of proportionality is a function of the parameter S and the hydrogen concentration C:

$$\sigma_0 = K(S,C)3\varepsilon_0 \quad (8)$$

Where ε_0- average strain, *K* (*S*, *C*) - three-dimensional elastic modulus.

$$K(S,C) = \begin{cases} K_0, S \le S_0 \\ K_1(S,C), S > S_0 \end{cases} \quad (9)$$

S ≤ S0 - value of the parameter S, corresponds to the diagram of the state of stress with predominance of compression components, which starts the degradation of properties of the metal under the influence of hydrogen.

- Second hypothesis: In any point of the body, the stress deviator is directly proportional to the deflection deformation. Below the scalar form is written as follows:

$$\sigma_x - \sigma_0 = \frac{2\sigma_u}{3\varepsilon_u}(\varepsilon_x - \varepsilon_0) \quad ; \quad \tau_{xy} = \frac{\sigma_u}{3\varepsilon_u}\gamma_{xy} \quad (10)$$

$$\sigma_x - \sigma_0 = \frac{2\sigma_u}{3\varepsilon_u}(\varepsilon_y - \varepsilon_0) \quad ; \quad \tau_{yz} = \frac{\sigma_u}{3\varepsilon_u}\gamma_{yz} \quad (11)$$

$$\sigma_z - \sigma_0 = \frac{2\sigma_u}{3\varepsilon_u}(\varepsilon_z - \varepsilon_0) \quad ; \quad \tau_{zx} = \frac{\sigma_u}{3\varepsilon_u}\gamma_{zx} \quad (12)$$

Where: σ_x, σ_y, σ_z, τ_{xy}, τ_{yz}, τ_{zx} - components of the stress tensor, ε_x, ε_y, ε_z, γ_{xy} γ_{yz}, γ_{zx} - components of the tensor deformations.

- Third hypothesis: Assume that the intensity of σu stresses is a function of the deformation intensity of εu of pattern setting for stress state S and the hydrogen concentration C:

$$\sigma_u = \varphi(\varepsilon_u, S, C) \quad (13)$$

This function has the following form:

$$\varphi(\varepsilon_u, S, C) = \begin{cases} \varphi_0(\varepsilon_u); \quad S \le S_0 \\ \varphi_1(\varepsilon_u, S, C), \ S > S_0 \end{cases} \quad (14)$$

It is obvious that in order to determine the functions $\varphi_0(\varepsilon_u)$ and the $\varphi_1(\varepsilon_u, S, C)$, we need the experimental curves of metal deformation for different *S* state of stress patterns and concentration of hydrogen *C* in the test samples.

In the particular case, we can take:

$$\varphi_1(\varepsilon_u, S, C) = \varphi_0(\varepsilon_u).\, y(S,C) \quad (15)$$

where : φ0(εu) - approximating the function of the material deformation curve for S ≤ S0 and the function of the influence of the pattern of the stress state and the hydrogen concentration y(S, C) is defined as:

$$y(S,C)\begin{cases} 1, \quad then \ S \le S_0 \\ \exp[-KC^\alpha(S-S_0)^b, \quad then \quad S > S_0 \end{cases} \quad (16)$$

Where k, a, b – constants.

The type of the function y (S, C) in the equation (16) has been suggested by [17], on the basis of the experimental data analysis on the influence of the pattern of the stress state and hydrogen concentration on the mechanical properties of materials.

2.3. Progression model limit state

Much attention has been paid by the authors of the work [17], to the problem of developing models limit state of structures under the hydrogenation conditions. To develop the limit state model, we will consider the fact observed experimentally that the material located in a plastic state before hydrogenation, under the influence of hydrogen, is weakened. To reflect this, we introduce the fragility parameter:

$$\xi(S,C) = \sigma_B(S,C) / \sigma_B^0 \quad (17)$$

Representing the resistance ratio of the rupture strength of the material after hydrogenation σ_B (*S*, *C*) to the initial rupture resistance σ_B^0 of the material before hydrogenation.

In the absence of hydrogenation effects σ_B (*S*, *C*) = σ_B^0, and the embrittlement parameter ξ =1. Under the action of hydrogen on the material under stress, there is a reduction σ_B (*S*, *C*) and a decrease in the parameter ξ.

By analogy with equation (13) can be taken:

$$\sigma_B(S,C) = \sigma_B^0\psi(S,C) \quad (18)$$

Where: ψ (*S*, *C*) - influence function of the form equation (16).

Resistance condition of the material subjected to hydrogenation, we take the form:

$$\sigma_U\,\xi + (1-\xi)\,\sigma_1 \le \sigma_B^0(S,C) \quad (19)$$

One can see that for ξ =1, the condition (19) becomes a plastic material condition resistance $\sigma_U \le \sigma_B^0$, and during hydrogen embrittlement as a measure that ξ decreases, a second term is included in the condition (19), reflecting the process of hydrogen embrittlement. Taking into account equation (15), the equation (17) can be transformed into the form:

$$\sigma_U + (\frac{1}{\xi} - 1)\sigma_1 \le \sigma_B^0 \quad (20)$$

If, at the end, and taking into account the equation (14), equation (15), equation (16), then resistance condition can be written permanently as follows:

$$\sigma_U \le \sigma_B^0 \quad then \ S \le S_0 \quad (21)$$

$$\sigma_U + \{exp[kC^\alpha(S-S_0)^b] - 1\}\,\sigma_1 \le \sigma_B^0 \quad then \ S > S_0$$

2.4. Delayed fracture model of metals in a hydrogenated medium

Delayed rupture of structures under the influence of hydrogen accounts for the process of accumulation of scattered damage, whose kinetics is determined by the pattern of the stress state and the hydrogen concentration.

During the simulation of delayed fracture in hydrogen, we assume that the assumptions are correct:

1. The influence of hydrogen on the mechanical properties of metals is the same for the short-term loading as for long-term loading;

2. In the case of the predominance of compressive components ($S \leq S_0$), the metal retains, its long term properties regardless of the concentration of hydrogen.
3. In the case of the predominance of traction components ($S > S_0$), under the influence of hydrogen, long-term mechanical properties are reduced, and the degree of reduction increases with the rigidity of the pattern of the S constrained state and the hydrogen concentration C.

To describe the kinetics of delayed fracture, one can use either the L.M. Kachanov approach, based on the use of the continuity of ψ parameter or the Y.N. Rabotnov approach based on the use of damage parameter Π or the A.R. Rzhanitsyn approach, based on the use of the concept of instantaneous resistance R of the material see reference [16].

Since the interaction process metal structures with hydrogen causes a change in mechanical properties, resulting in a change in the stress-strain state of the structure, and to describe the delayed fracture, it becomes important to use the model of the accumulation of damage of Moskvitin see reference [16], which is suitable for both stationary stress states and non-stationary.

The V. V. Moskvitin model applied to the case of delayed fracture of the metal in the hydrogen has the form:

$$\Pi = \int_0^t (t-T)^m \, \eta[\sigma_э(\tau), S(\tau), C(\tau)] d\tau \tag{22}$$

The function η [$\sigma_Э$, S, C] in this equation can be taken as:

$$\eta[\sigma_э, S, C] = \frac{m(S,C)+1}{t_r^{m(S,C)+1}(\sigma_э)} \tag{23}$$

and dependence breakup time t_r depending on the equivalent stress (long-term resistance curve) is approximated by the following function:

$$t_r(\sigma_э) = \frac{A(S,C)}{\sigma_э^{b(S,C)}} \tag{24}$$

Substituting equation (23) in equation (22) taking into account equation (24), we can write:

$$\Pi = \int_0^t \frac{[m(S,C)+1]\sigma_э^{b(S,C)[m(S,C)+1]}}{[A(S,C)+1]^{[m(S,C)+1]}} (t-T)^{m(S,C)} d\tau \tag{25}$$

As can be seen, the effect of the hydrogenation is taken into account through the dependence of the coefficients A, b, m of the parameter diagram of the S state of stress and hydrogen concentration C.

In the case of the predominance of compressive components ($S \leq S_0$), equation (25) is simplified and reduced in the form:

$$\Pi = \frac{m_0+1}{A_0^{m_0+1}} \int_0^t \sigma_э^{b_0(m_0+1)} (t-T)^{m_0} d\tau \tag{26}$$

Where the coefficients A_0, b_0 and m_0 correspond to the metal in the non-hydrogenated state.

3. Application of the developed model to the hydrogenation problem of a thick-walled tube

3.1. Basic equations for deformation of a thick-walled tube during hydrogenation

We examine the application of the model developed to the hydrogenation problem of a thick-walled tube subjected to an axisymmetric load in a hydrogenated medium. In this case, stress and strain tensors will have non-zero components σ_r, σ_φ, σ_z, ε_r, ε_φ. All three components of deformation, shear and tangential stresses will be equal to zero, due to symmetry with the tube axis and the constancy of the conditions along its axis. The relationship between the stresses and the deformations has the following form:

$$\varepsilon_r = \frac{1}{\psi}\left(\sigma_r - \nu\left(\sigma_\varphi + \sigma_z\right)\right)$$

$$\varepsilon_\varphi = \frac{1}{\psi}\left(\sigma_\varphi - \nu\left(\sigma_r + \sigma_z\right)\right) \tag{27}$$

$$\varepsilon_z = \frac{1}{\psi}\left(\sigma_z - \nu\left(\sigma_r + \sigma_\varphi\right)\right)$$

Where: r, z - radial, circumferential and longitudinal coordinates, and $\psi(\varepsilon_u, C, S)$ - function of strain intensity ε_u, C - hydrogen concentration (in the traction zones of the hollow cylinder) = $S = \sigma_0/\sigma_u$ - parameter characterizing the stiffness state of stress state, σ0 - average stress, σu - stress intensity.

The function $\psi(\varepsilon_u, C, S)$ is taken as:

$$\psi(\varepsilon_u, \mathrm{C}, \mathrm{S}) = \begin{cases} A_0 - B_0\varepsilon_u^{m-1} & then\ S < S_0 \\ A_0 - B_0\theta^{1-m}(C,S)\varepsilon_u^{m-1} & then\ S \geq S_0 \end{cases} \tag{28}$$

The transverse strain coefficient ν and is also taken as a function of ε_u, C and S:

$$\nu(\varepsilon_u, \mathrm{C}, \mathrm{S}) = \begin{cases} \nu_0 & then\ S < S_0 \\ \dfrac{1}{2} - \dfrac{1-2\nu_0}{\psi_0}\psi(\varepsilon_u, \mathrm{C}, \mathrm{S}) & then\ S \geq S_0 \end{cases} \tag{29}$$

The function (C, S) in equation (28) is written in the form:

$$\theta(\mathrm{C}, \mathrm{S}) = \begin{cases} 1 & then\ S < S_0 \\ \exp(-kC^a(S-S_0)^b) & then\ S \geq S_0 \end{cases} \tag{30}$$

Where: k, a, b - coefficients.

By expressing σ_z through σ_r and σ_φ in the third equation (27) and substituting it in the first two equations (27), it is found:

$$\begin{aligned} \varepsilon_r &= \frac{1-\nu^2}{\psi}\left(\sigma_r - \frac{\nu}{1-\nu}\sigma_\varphi\right) - \nu\varepsilon_z, \\ \varepsilon_\varphi &= \frac{1-\nu^2}{\psi}\left(\sigma_\varphi - \frac{\nu}{1-\nu}\sigma_r\right) - \nu\varepsilon_z. \end{aligned} \tag{31}$$

By substituting the expressions of ε_r and ε_φ in the continuity equation of the deformation:

$$\frac{d\varepsilon_\varphi}{dr} = \frac{(\varepsilon_r - \varepsilon_\varphi)}{r} \tag{32}$$

And taking into consideration, that according to the equation of equilibrium:

$$\frac{d\sigma_r}{dr}+\frac{\sigma_r-\sigma_\varphi}{r}=0 \tag{33}$$

$$\sigma_\varphi=\sigma_r+r\frac{d\sigma_r}{dr},\ \frac{d\sigma_\varphi}{dr}=2\frac{d\sigma_r}{dr}+r\frac{d^2\sigma_r}{dr^2} \tag{34}$$

After some transformations, we obtain the following nonlinear equation of constraints.

$$\frac{d^2\sigma_r}{dr^2}+\lambda\frac{d\sigma_r}{dr}+\eta\sigma_r=F \tag{35}$$

The coefficients λ and η in this equation are nonlinear functions of ψ and v and their derivatives:

$$\lambda=\frac{3}{r}-\frac{2vv'}{(1-v^2)}-\frac{\psi'}{\psi},$$
$$\eta=-\left((1-4v)v'+(1-v-2v^2)\psi'/\psi\right)/r(1-v^2). \tag{36}$$

Where: v and ψ - derived from r.

The right part of F has the form:

$$F=\psi\varepsilon_z v'/r^2(1-v^2) \tag{37}$$

The longitudinal deformation ε_z is determined from the equilibrium conditions of the thick-walled tube in the longitudinal direction:

$$N=2\pi\int_{r_1}^{r_2}\sigma_Z r dr \tag{38}$$

Hence, replacing by the expression of σ_z, we obtain:

$$\varepsilon_Z=\left(\frac{N}{2\pi}-\int_{r_1}^{r_2}v(\sigma_r+\sigma_\varphi)\right)\Big/\left(\int_{r_1}^{r_2}\psi r dr\right) \tag{39}$$

Where: r_1 and r_2 - internal and external radius of the thick-walled tube, respectively.

If the tube is loaded by external and internal pressures (fig.1.a) then the boundary conditions for the differential equation (35) are written as follows:

$$\sigma_r(r=r_1)=-P_1,\quad \sigma_r(r=r_2)=-P_2 \tag{40}$$

The concentration distribution of hydrogen according to the tube thickness is determined from the diffusion equation (2), written in a cylindrical coordinate system and taking into account the influence of the stresses:

$$\frac{1}{D}\frac{\partial C}{\partial t}=\frac{\partial^2 C}{\partial r^2}+\frac{1}{r}\frac{\partial C}{\partial r}-\frac{V_H}{RT}\left(\frac{\partial C}{\partial r}\cdot\frac{\partial\sigma_0}{\partial r}\right)$$
$$-\frac{CV_H}{RT}\left(\frac{\partial^2\sigma_0}{\partial r^2}+\frac{1}{r}\frac{\partial\sigma_0}{\partial r}\right) \tag{41}$$

Where: σ_0 - mean stress determined from the expression: $\sigma_0=(\sigma_r+\sigma_\varphi+\sigma_z)/3$

t - time, D - diffusion coefficient, R - gas constant.

The initial and boundary conditions must be added to equation (41), taking into account the action of the hydrogenous medium on the thick-walled tube.

If hydrogen acts on the inner and outer surfaces of the tube (fig.1.b), then the boundary and initial conditions will be:

$$C(r=r_1)=C(r=r_2)=C_\infty,\ C(t=0)=C_{in} \tag{42}$$

If the hydrogen penetrates into the wall of the tube from the inside, and the reflux of the outer surface is not taken into account (fig. 1.c), then we have:

$$C(r=r_1)=C_\infty,\ \frac{\partial C}{\partial r}(r=r_2)=0,\ C(t=0)=C_{in} \tag{43}$$

Under the action of hydrogen on the outer surface tube and the absence of the reflux of the inner surface (fig. 1.d)

$$\frac{\partial C}{\partial r}(r=r_1)=0,\ C(r=r_2)=C_\infty,\ C(t=0)=C_{in} \tag{44}$$

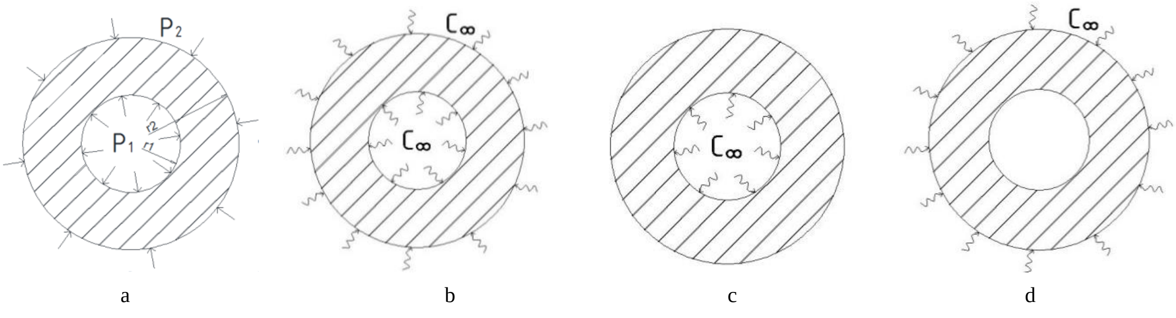

Figure1: Variants of the influence of the hydrogen medium and of the pressure on a thick-walled tube

3.2. Method of the thick-walled tube calculation, subjected to hydrogenation

When designing the method of calculating the thick-walled tube, subjected to a combined action of the filler and the hydrogen-containing medium, the work program of the structure is presented in the form of a succession of three stages [17]:

1. the stage of loading;
2. the stage of establishing the boundary conditions on the surfaces in contact with the hydrogenated medium;
3. stage of deformation of the thick-walled tube as a result of the change in the properties of the material under the influence of the hydrogenated medium in accordance with (28) and (29).

At the stage of application of the load, the calculation of the thick-walled tube is reduced to the solution of the homogeneous differential equation of the type:

$$\frac{\partial^2\sigma_r}{\partial r^2}+\lambda\frac{\partial\sigma_r}{\partial r}+\eta\sigma_r=0 \quad (45)$$

With boundary conditions (40).

The coefficients λ and η are determined for the initial characteristics of the material.

The solution of the linear - elastic problem for the thick - walled tube is solved for the resolution of the non - linear part of the problems (45), (40), and as a zero approximation Of Blade), which has the form:

$$\sigma_r^o=I+J/r^2 \quad , \quad \sigma_\varphi^o=I-J/r^2 \quad (46)$$

where :

$$I=(P_1r_1^2+P_2r_2^2)/(r_2^2-r_1^2) \quad ,$$
$$J=(P_2-P_1)r_1^2r_2^2/(r_2^2-r_1^2) \quad (47)$$

For the resolution of the other part (problem at the limits) of the problems (45), (40), we use the method of scanning (algorithm of tridiagonal matrix), and in addition to find the derivatives one uses the formula of Lagrange, and the integrals in the expressions for λ and η by the Simpson formula of order 4.

At the next stage of the boundary conditions it is assumed that the concentration of hydrogen required on the surfaces of the tube is not established immediately, but during a certain t_d, given by the expression:

$$t_d=\Delta r/4D \quad (48)$$

A suitable distribution of the mechanical parameters (and consequently the coefficients λ, η and the right part of the equation (35)) is found according to the concentration field of the hydrogenated medium at the corresponding time *tr*.

The third stage is devoted to the study of the deformation process of the thick-walled tube, caused by the action of the hydrogenated medium. The problem is solved by time increments. First, by the finite difference method, the diffusion equation (41) is solved with the initial conditions and with the corresponding limits, taking into account the distribution law of the mean stress σ0 according to the thickness of the wall of the tube. Depending on the found distribution of the hydrogen concentration C, taking into account the rigidity of the stress state diagram S according to formulas (36), (37), in the nodes of the network are found the values of the coefficients Λ and η and the right-hand part of F of equation (35), which is then solved by the scanning method. Then, the following time increment Δt is given and the calculation process is repeated.

The problem is solved by time increments until the In order to evaluate the reliability of the solution obtained, an example of calculation of a thick-walled tube of non-linear material was tested with the strain diagram $\sigma = A\varepsilon\text{-}B\varepsilon^m$, where A = 3 · 104 MPa, B = 2 · 105 MPa, m = 1.5. In the calculations we have taken $P_1 = 0$,

$P_2 = 20$ MPa, $r_1 = 30$ cm, $r_2 = 60$ cm, $\nu = 0.3$.

In Figure 2, we present the results of our calculation in dotted lines, and in solid lines those of the work [17]. We observe a certain difference in the distribution of constraints, which is explained by the use by the authors of the work [17] of assumptions about the incompressibility of the material ($\nu = 0.5$), and in our calculations $\nu = 0.2$. The calculation for $\nu = 0.5$ leads to a total similarity of the results.

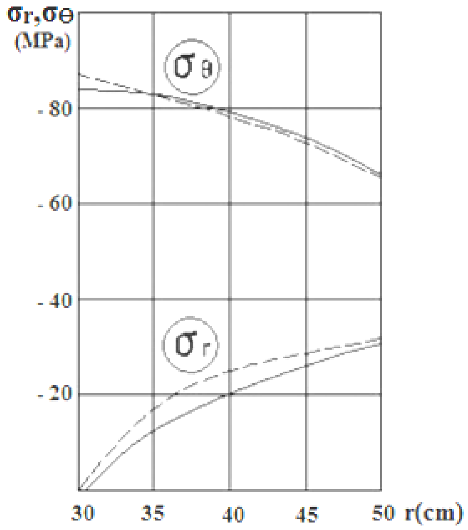

Figure 2: Calculation results for thick-walled tube

In order to evaluate the influence of the size of the finite difference network (depending on the wall thickness of the thick-walled tube) on the results of the calculation, a test calculation was made on a tube made of material with the In the calculations, we took $P_1 = 20$ MPa, $P_2 = 0$, $r_1 / r_2 = 0.5$. The results of the calculation are shown in Table 2.

Table 2. The results of the calculation

Number of nodes in the mesh	Values	
	σ_n/P_1	ε_n, %
11	2,1458	0,2255
21	2,1437	0,2218
41	2,1570	0,2241
81	2,1466	0,2220
161	2,1380	0,2225

Subsequently, the calculations are carried out on a network with 81 nodes.

3.3. Analysis of the influence of the state of stress on the permeability to hydrogen of the thick-walled tube (long hollow cylinder).

In order to evaluate the influence of the stress state on the hydrogen diffusion kinetics in the wall of the thick-walled tube, the calculation was carried out initially without taking into account the influence of the stress state on the Kinetics of diffusion, and then taking it again into consideration. The studies were carried out for three cases of loading and effects of the hydrogenated medium:

1. the charge P_1 and the hydrogen medium act on the inner surface of the thick-walled tube;
2. the charge acts on the outer surface of the thick-walled tube, and the hydrogen on the inner surface;
3. the charge acts on the inner surface of the thick-walled tube, and the hydrogen on the outer surface.

The pressure in all calculations is $P_1 = P_2 = 20$ MPa, the dimensions of the tube: $r_1 = 5$ cm, $r_2 = 10$ cm.

In Fig. 3, the graphs of the hydrogen concentration according to the tube radius for case 1 are presented, in the absence of the influence of the constraints on the diffusion kinetics (dotted line) and taking account of this influence (full line).

The analysis shows that the stress state has an intensifying effect on the hydrogen saturability of the tube wall, and with the increase of the time of the effect of the stresses, it increases and the increase reaches 34%.

The influence of the stress on the hydrogen saturation kinetics for case 2 is shown in fig.4.

In this case, there is a stress-inhibiting effect on the hydrogen saturability of the tube walls, because the load causes compression stresses to occur. The largest difference in the hydrogen concentration graphs is 29% for $t_3 / t_r = 0.31$.

Fig. 5 illustrates the influence of the stress state on the hydrogen diffusion kinetics for case 3, when the charge acts from the inside, and the hydrogen from the outside

As can be seen, at certain points on the wall of the tube, the difference in the magnitude of the hydrogen concentration can reach 50% (at $t_2 = 0.15$), and destruction $t_2 = t_r$ it reaches 26%.

The analysis carried out makes it possible to conclude that taking into account the influence of stress state on the hydrogen permeability of the structures is necessary both under the action of compressive stresses (fig.4). With the predominance of tensile stresses (figures 3 and 5).

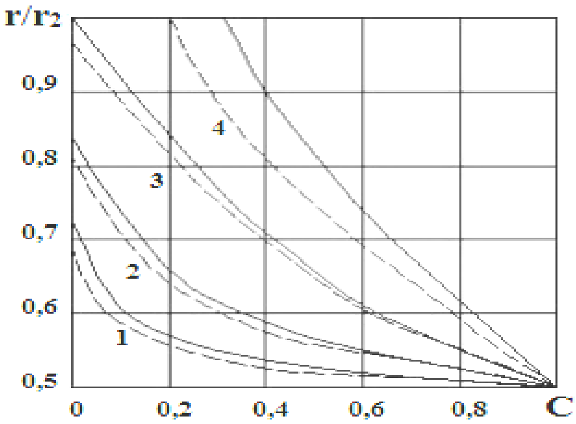

Figure 3: Concentration of hydrogen according to the thickness of the wall of the tube (case 1)
(dotted line - absence of the influence of constraints on the kinetics of diffusion, full line - with considering
(1 – t=0,076; 2 – t=0,15; 3 – t=0,31; 4 – t=tr=1)

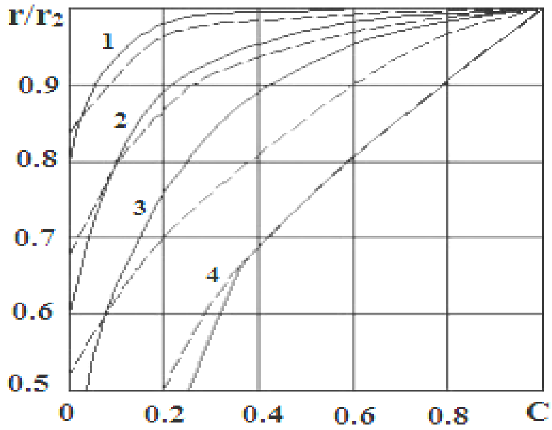

Figure 4: Concentration of hydrogen according to the wall thickness of the tube (case 2)
(dotted line - excluding the impact of stress, full line - with considering) , (1 – t=0,076; 2 – t=0,15; 3 – t=0,31; 4 – t=tr=1)

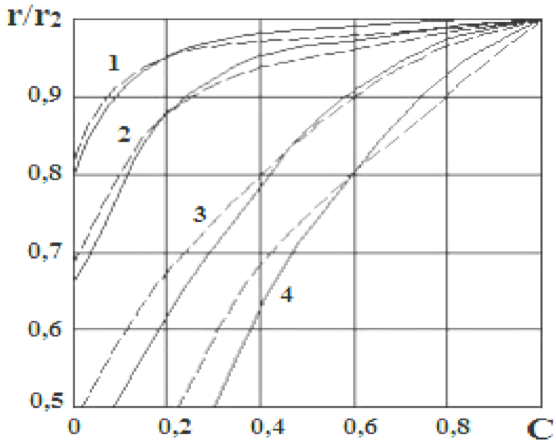

Fig.5: Concentration of hydrogen according to the wall thickness of the tube (case 3)
(dotted line - excluding the impact of stress, full line - with considering), (1 – t=0,076; 2 – t=0,15; 3 – t=0,31; 4 – t=tr=1)

3.4. Analysis of the influence of the loading scheme on the character of the stress state of a thick-walled tube under the action of the charge and the hydrogenation

In order to evaluate the effect of the stiffness of the stress state diagram that is characterized by the parameter *S*, the equations mentioned above, the mutual influence and the hydrogenated medium should be taken into consideration, which have been used on the mechanical characteristics of the material, and on the stress-strain condition, and the stress state on the hydrogen diffusion kinetics in the tube wall. That is to explain that the problem is part of non-linear deformation.

The same cases of loading and effects of the hydrogenated medium are examined as in paragraph 3.

For case 1 (the charge and the hydrogen acting from the inside), the results of the calculation in the form of diagrams of the concentration of hydrogen *C* and the circumferential stress σ are shown in Fig.6. It can be seen that in the zone close to the inner surface of the tube, on which the charge and the hydrogen are acting, the stress field is restructured, resulting in the most hydrogenated zones being discharged and the less hydrogenated - are charged.

In fig. 7, the hydrogen concentration diagrams *C*, the circumferential stresses σf and the longitudinal stresses σ_z for case 2 (external charge, hydrogen from the inside) are presented. As can be seen, in this case the change in the state of stress is less important, which is explained by the fact that the walls of the tube are in a compressed state and that is why the change in the mechanical characteristics is insignificant.

Finally, the illustrated fig.8 the character of the distribution of concentration hydrogen C, of the circumferential stresses σ_f according to the thickness of the wall of the tube for case 3 (charge from the inside, hydrogen from the outside). As can be seen, under the influence of the constraints of traction and hydrogenated medium a place a change of the mechanical properties of the material, resulting in a change in the character of distribution of the constraints. In addition, the greatest changes in the stress state occur in the internal zones of the tube wall and the values of these changes reach 18%.

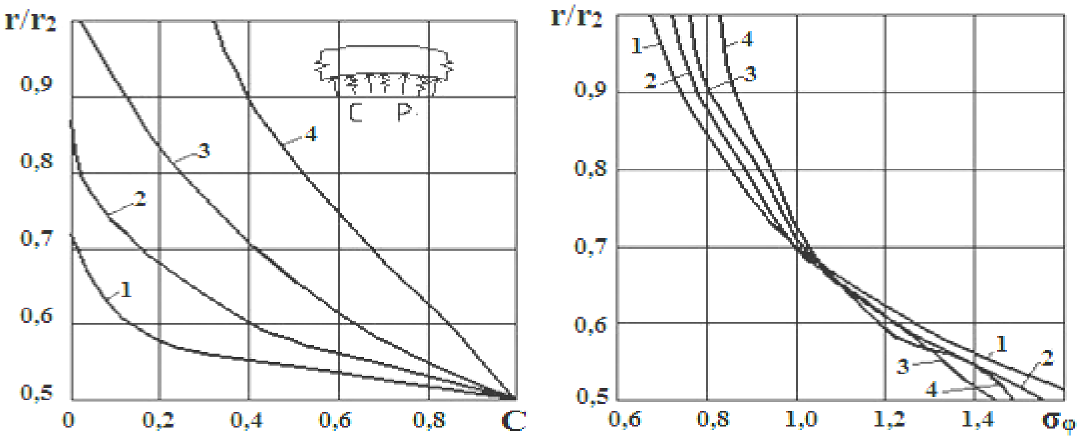

Figure 6: Hydrogen concentration and stresses σf at different times
(1 – *t*=0,076; 2 – *t*=0,15; 3 – *t*=0,31; 4 – *t*=t_r=1)

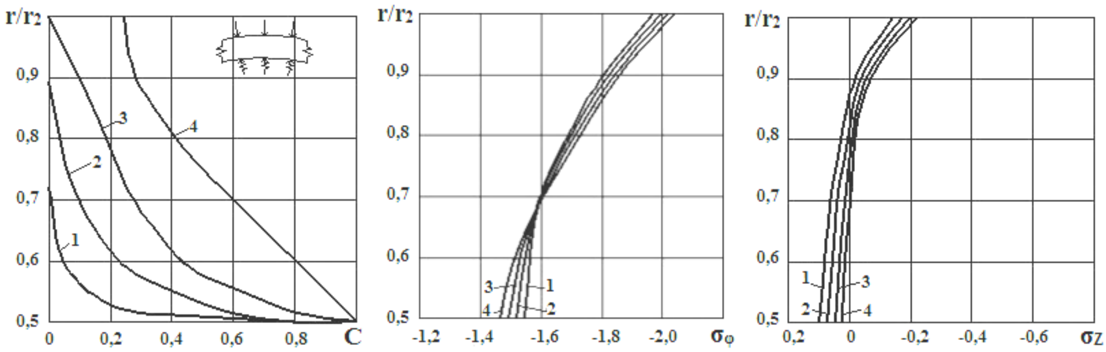

Figure 7: Concentration of hydrogen C, circumferential σf and longitudinal σz stresses in the tube
(case 2) at different times (1 – *t*=0,076; 2 – *t*=0,15; 3 – *t*=0,31; 4 – *t*=t_r=1)

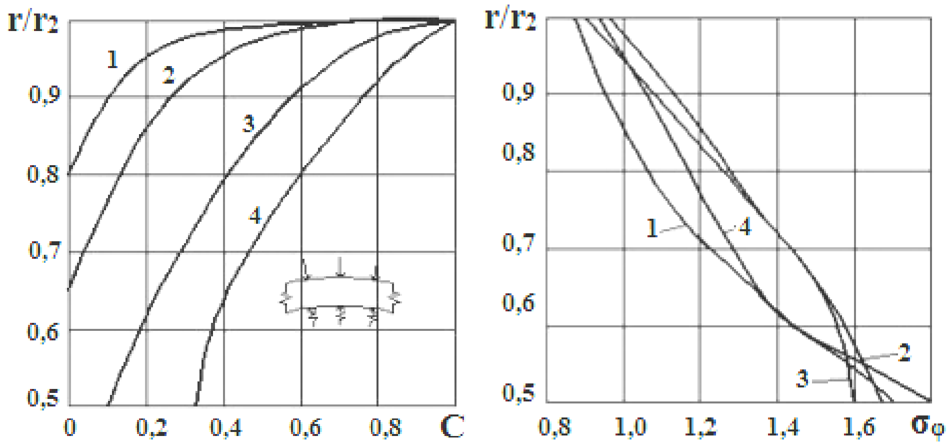

Figure 8: Hydrogen concentration and stresses σ_f at different times (case 3)
(1 – t=0,076; 2 – t=0,15; 3 – t=0,31; 4 – t=tr=1)

4. Conclusions

1. The elaborated model of material deformation in a hydrogenated medium takes into account the selective effect of hydrogen at low temperature on the mechanical characteristics of materials, leading to the appearance of an induced anisotropy and changing with saturation of the hydrogen material. The selectivity is expressed as a function of the value of the anisotropy induced not only by the concentration of hydrogen, but also by the state rigidity of the stress state.
2. In the proposed model, consideration is given to the influence of the type and level of stress state of the material on the penetration kinetics (permeation) of hydrogen in the material through the dependence of the coefficient of diffusion and the hydrogen absorption limit of the special parameter, characterizing the stress state diagram.
3. The analysis carried out shows that the established relations describe quite correctly the behavior of the thick-walled tube under the conditions of the combined action of the charge and of the hydrogenation taking into account the destructive action of hydrogen and allow to take into account the main effects, accompanying the interaction of the thick-walled tube with hydrogen.
4. The proposed method and the computational algorithm allow to perform a correct analysis of the kinetics of the hydrogenation changes and the stress state of a thick-walled tube taking into account the connectivity of the solved problem, I.e. the combined effect of hydrogen on the mechanical properties of the material and then on the state of stress of the tube and the influence of the state of stress on the diffusion kinetics of the material. Hydrogen in the walls of the thick-walled tube.
5. The numerical simulation carried out has shown that the most dangerous case is the case of the simultaneous action of the charge and of hydrogen on the surface Inside the wall of the thick-walled tube, because in this case the combination of the action of tensile stresses and hydrogen leads to the most intensive degradation of the tube material. It should be noted that such a case of the influence of the charge and of the hydrogenated medium is the most characteristic for the actual operating conditions of the thick-walled tubes.

References

[1] I. Dincer, "Hydrogen and fuel cell technologies for sustainable future". Jordan Journal of Mechanical and Industrial Engineering, Vol.2 (2008) No.1, 1-14.

[2] M. Cabrini, S. Lorenzi, S. Pellegrini, "Environmentally assisted cracking and hydrogen diffusion in traditional and high-strength pipeline steels". Corrosion Reviews, Vol.33 (2015) No.6, 529-545.

[3] A. Bueno, E. Moreira, J. Gomes, "Evaluation of stress corrosion cracking and hydrogen embrittlement in an API grade steel", Engineering Failure Analysis, Vol. 36 (2014), 423–431.

[4] S. Serebrinsky, E.A. Carter, M. Ortiza," A quantum-mechanically informed continuum model of hydrogen embrittlement". Journal of the Mechanics and Physics of Solids, Vol.52 (2004) No.10, 2403 – 2430.

[5] B.A. Kolachev, "Hydrogen in metals and alloys". Metal Science and Heat Treatment, Vol.41 (1999) No.3, 93-100.

[6] J. Woodtli, R. Kieselbach, "Damage due to hydrogen embrittlement and stress corrosion cracking". Engineering Failure Analysis, No.7 (2000), 427- 450.

[7] T.J. Carter, L.A. Cornishn, "Hydrogen in metals". Engineering Failure Analysis, Vol.8 (2001) No.2, 113-121.

[8] D. Hardie, E.A. Charles, A.H. Lopez," Hydrogen embrittlement of high strength pipeline steels". Corrosion Science, Vol. 48 (2006) No.12, 4378–4385.

[9] S. Lynch,"Hydrogen embrittlement and mechanisms".Corrosion Reviews, Vol.30 (2012) No.3-4, 105-123.

[10] A. Balueva,"Modeling of Hydrogen Embrittlement Cracking in Pipe-lines under High Pressures". Procedia Materials Science, (2014) No.3, 1310-1315.

[11] M.B. Djukic, V. Sijacki Zeravcic, G.M. Bakic, A. Sedmak, B. Rajicic, "Hydrogen damage of steels: A case study and hydrogen embrittlement model".Engineering Failure Analysis, Vol.58 (2015) No.2, 485-498.

[12] C.J. McMahon," Hydrogen-induced intergranular fracture of steels". Engineering Fracture Mechanics, Vol.68 (2001) No.6, 773–788.

[13] H.K. Birnbaum, "Hydrogen effects on deformation and fracture: science and sociology". MRS Bulletin, Vol.28 (2003) No.7, 479-485.

[14] P. Novak, R. Yuan, B.P. Somerday, P. Sofronis, R.O. Ritchie,"A statistical, physical-based, micro-mechanical model of hydrogen-induced intergranular fracture in steel". Journal of Mechanics and Physics of Solids, Vol.58 (2010) N°2, 206–226.

[15] N.H. Kim, C.S. Oh, Y.J. Kim, B. Yoon Ke, Y.W. Ma," Hydrogen-assisted stress corrosion cracking simulation using the stress-modified fracture strain model". Journal of Mechanical Science and Technology, Vol.26 (2012) No.8, 2631-2638.

[16] Bubnov AA., Bubnov SA., Ovchinnikov I I., Modelling of stress state and fracture of thick-walled piping in hydrogen corrosion and heterogeneous thermal field. Moscow: Goryachaya Liniya –Telekom ; 2011. (in Russian)

[17] Ovchinnikov IG., Khvalko TA., Serviceability of structures under high-temperature hydrogen corrosion. Saratov: Sarat. Gos. Tekhn. Un-t ; 2003. (in Russian)

JJMIE

Jordan Journal of Mechanical and Industrial Engineering

Volume 12 Number 1, June. 2018
ISSN 1995-6665
Pages 17 - 22

Optimization of Welding Parameters by Using Taguchi Method and Study of Fracture Mode Characterization of SS304H Welded by GMA Welding

Saadat Ali Rizvi[a,*] , S.P Tewari[b]

[a]*Mechanical Engineering Department ,Indian Institute of Technology (BHU), Varanasi and faculty member in UP J.M.I, New Delhi, India*
[b]*Mechanical Engineering Department, Indian Institute of Technology (BHU), Varanasi, India*

Received 24 July 2017 *Accepted 21 June 2018*

Abstract

This study focuses on optimizing different welding parameters which affect the mechanical properties such as YS, UTS, Toughness, and Vicker hardness (VHN) of SS304H, Taguchi technique was employed to optimize the welding parameters, and fracture mode characterization was studied. A series of experiments have been carried out. L9 orthogonal array (3xx3) applied for it. Statistical methods of signal to a noise ratio (SNR) and the analysis of variance (ANOVA) was applied to determine the effects of different welding parameters such as wire feed speed, welding current and gas flow rate on Mechanical properties. Tensile strength, toughness, Vicker hardness (VHN), and mode of fracture were examined to investigate the weld quality of SS304H, and it was observed from the results that the welding voltage has significant effect whereas gas flow rate has insignificant effect on tensile strength of the weldment, and optimum process parameters were found to be 23 V, 350 IPM travel speed of wire and 20 l/min gas flow rate for tensile strength and mode of fracture was ductile fracture for tensile test specimen.

Keywords: *GMAW/MIG, Mechanical properties, ANOVA, stainless steel, mode of fracture, SEM, S/N ratio*.

1. Introduction

Gas metal arc welding (GMAW) is an advanced version of electric arc welding in which no pressure is applied during the welding process and arc is created between a continuous copper coated wire and work piece [1]. This GMAW commonly used method for joining of steels structural, components for the automotive industry [2-3]. Type 304/304L is the modern evolution of the original “18-8” austenitic stainless steel. It is very economical and versatile corrosion resistant stainless steel suitable for a wide range of general purpose applications.SS304H with a higher chromium and lower carbon content. Lower carbon contents minimize chromium carbide precipitation during welding and its susceptibility to intergranular corrosion.SS304H frequently was used in various industries such as Chemical and Petrochemical, Processing industries, pressure vessels, tanks, valves and pumps, heat exchangers, piping systems, flanges, fittings, Medical, Pharmaceutical Processing, Food, Beverage Processing and nuclear industries due to its excellent tensile strength, good weldability, and better corrosion resistance properties [4]. Dinesh Mohan arya et al [5] investigated process parameters for Metal Inert Gas welding and they reported that welding current is having maximum percentage contribution in experimental work. Nabendu Ghosh et al [6] optimized the metal inert gas welding parameters, by Grey-Based Taguchi method and they reported in their result that current having the more significant effect than gas flow rate in influencing the strength of the welded joints.

Vikas Chauhan and R. S. Jadoun [7] studied the joining of two dissimilar metals SS304 and Low Carbon Steel by metal inert gas Welding (MIG) and they optimized the process parameter by using Taguchi Design Method and finally they informed that the effect of welding parameters on the ultimate tensile strength can be ranked in decreasing order as follows: voltage >speed > current. Abhishek Prakash et al [8] determined the (welding) process parameters which influence the mechanical properties by using the Taguchi method and they produced a result that Welding Current has the greatest influence on Tensile and Hardness in the Weldability of welded joint followed by wire feed speed and arc voltage. S. M. Bayazid et al [9] predicted welding parameters such as travel speed, rotational speed and plates position on microstructure and mechanical properties of Friction Stir Welded joint of two dissimilar Aluminum 6063 and 7075 alloys via Taguchi method and they reported that rotational speed, travel speed and plates position have 59, 30 and 7 % influence on

* Corresponding author e-mail: sarizvi1@jmi.ac.in.

tensile strength of welded joint respectively. Saurav Datta et al [10] developed a multi-response problem to optimize parameters by combining to yield favorable bead geometry of submerged arc bead on-plate weldment and they coupled the Taguchi optimization method with Grey relation technique to evaluate the optimal parametric combination for deeper penetration, minimum bead height and depth HAZ of welded part. D Kalita and P. B Barua[11] investigated the effect of the process parameters of Metal Inert Gas Welding such as welding current, arc voltage and shielding gas flow rate on tensile strength of welded joints by the Taguchi Optimization method and they concluded that welding voltage has significant effect, both on mean and variation of the Tensile strength of the weld having 87.019% and 85.398% contribution respectively, whereas welding current has significant effect on mean only (10.807% contribution) whereas Shielding gas flow rate has insignificant effect on the tensile strength of the welded joint.

Therefore, in this research article, an attempt has to be made to optimize the process parameters of metal inert gas (MIG) welding. S R.Chikhale et al [13] predicted the mechanical properties of Al Alloy 6061-T6 by metal inert gas welding and they consider the welding current, arc voltage and wire feed speed as welding parameters and finally they optimized the parameters by reporting that welding current has the most significant effect on the Tensile strength, depth of penetration and toughness of weld joint. Saadat Ali Rizvi et al [14] optimized various welding process parameters by application of Taguchi method on MIG welding during welding of IS2062, and they mentioned in their research results that welding current and welding voltage have significant effect whereas gas flow rate has an insignificant effect on tensile strength of the weldment. Emmanuel O. Ogundimu et al [15] studied the mechanical properties and microstructure of AISI 304 weldment, welded by MIG and TIG welded and they concluded that welding current has the most significant effect on weldment hardness and they also added that UTS is depended on welding parameters. Woei-Shyan Lee et al [16] studied the fracture behaviour of SS 304 welded and they analysed the fractography of failed samples and observed that weldments, all fail in a ductile manner as a result of an extensive localized shearing in the fusion zone and they also added that failure of the weldments initiates at the site of second-phase particles within the fusion zone. Uğur ÇALIGÜLÜ et al [17] observed the tensile fracture of weldment and they concluded that after welding, it is seen that tensile strength values can be decreased depending on increasing the welding speed and this values can be increased depending on increasing the heat inputs, mainly in ductile fracture manner due to the fact that the ferritic stainless steel is a ductile steel. Anmol jeet Singh and Rutash Mittal[18] applied the Taguchi technique to optimize the process parameters and the observed that a dimple pattern in the whole width of impact fracture specimen which confirms the ductile mode failure of the joints. Ýhsan Kirik and Niyazi Özdemýr [19] examined the fracture mode of SS 304 weldment and mentioned that the tensile test mostly occurred on the AISI 1040 side, and especially ductile fractures in the form of quasi-cleavages were observed in the dimples. Ravindra V. Taiwade et al [20] examined the fractured surface of tensile test of AISI 304 weldment and they observed that the AISI 304 SS failed due to ductile fracture. The fractured surfaces of AISI 304 SS showed a wide range of dimple sizes of equiaxed type.

2. Design and Experimental work

2.1. Workpiece material

In this research article i,e Stainless steel 304H was used as a raw material.SS 304H plate of dimension 150mm × 60 mm× 5 mm were welded using Gas Metal Arc Welding (GMAW) machine, with Polarity Direct Current Electrode Negative [DCEN]. Actual GMA welding set up is shown in fig 1.

Figure 1: Actual welding setup of GMA

After completed weld, welded plates were machined on a horizontal milling machine for making V-groove. The chemical composition of the base metal plate and filler wire used in the process for welding purpose is given in Table .1 respectively.

Taguchi design of the experiment is a simple and foolproof approach which is used to reduce the analysis up to an optimal level. In this research article, three factors were selected with their levels as shown in Table 2. Selection of the orthogonal array was based on DOF. The degree of freedom for all three factors is 6 in this design and welded by GMAW process with different welding parameters, nine tensile test specimens were cut from welded piece longitudinally; vertical milling machine is used to produce an arc of R12.5mm and to produce “V” notch in Charpy impact test specimens. Tensile test specimens are fabricated as per ASTM standard and a tensile test specimen is shown in fig 2.

Table 1: Composition of base metal and filler wire

Material	% C	% Cr	% Ni	% Mn	% Si	% P	% S	Cu	Fe
Base plate	0.06	18.68	8.54	1.9	0.41	0.031	0.005	----	rest
Filler wire	0.08	19.5-22.0	9.0-11.0	1.0-2.5	0.3-0.65	0.030	0.03	0.75	rest

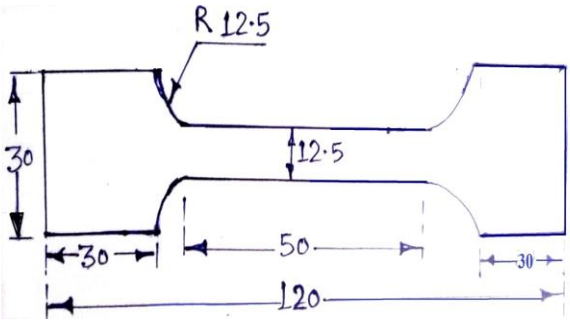

Figure 2: Tensile test specimen as per ASTM [12]

All tensile test specimens are tested on UTM-40T at room temperature. Tensile test specimens after fracture are shown in fig 3. Three different welding parameters are used to perform the welding. In entire, this research work pure Argon (Ar) was used as shielding gas to avoid any contamination of weld pool , as pure argon having special characteristics.

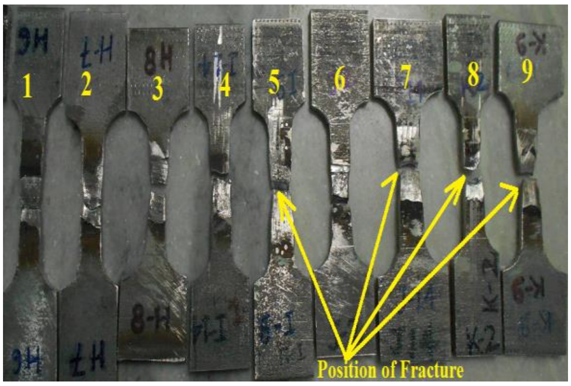

Figure 3: Tensile test specimens after fracture

2.2. Welding parameters

In this research article, parameters which are used for welding purpose are given in Table 2.

Table 2. Input (welding) parameters with their level

Variable	Level I	Level II	Level III
Voltage(V)	22	23	24
Gas flow rate (l/min)	10	15	20
Wire feed rate(IPM)	250	300	350

In the present experimental work, an L_9 OA with 3 columns and 3 rows was used. This array can handle three level process parameters. Nine experiments conducted to study the welding parameters using the L_9 OA.OA and the corresponding values of welding parameters are listed in Table 3.

3. Results

3.1. Evaluating the signal-to-noise (S/N) ratios

Noise factors are those uncontrollable factors which affect the process result (Output), whereas derived response is known as the signal. The variation of the index is known as S/N ratio. Variations are usually three types i, e "lower is better", "higher is better'' and "Normal is better". In the Present study Ultimate tensile strength (UTS), Vicker hardness (VHN), Toughness was output (weld quality). For good quality of weld hardness (VHN), Toughness and Ultimate tensile strength (UTS) consider as "higher is better''. In order to evaluate the influence of each selected factor on the response, S/N ratios for each control factor was calculated.

In the present research work tensile strength, Vicker hardness (VHN) and Toughness of welded pieces were identified as the responses, therefore, "higher the better" consider for tensile strength and "nominal the best" for Vicker hardness (VHN) characteristic chosen for analysis purpose

$$\frac{S}{N} = -10\log_{10}\left(\sum_{i=0}^{n}\frac{1}{y_i^2}\right), \text{ Higher is better} \quad (1)$$

$$\frac{S}{N} = -10\, log_{10}\left(\frac{1}{n}\sum_{i=0}^{n}(y_i^2)\right), \text{ Lower is better} \quad (2)$$

$$S/N = \ -10\, log_{10}\left(\frac{1}{n}\sum_{i=0}^{n}(y_i - m)^2\right), \quad (3)$$

Normal is better

For tensile strength. Response table or signal to noise is shown in table 4.

Table 4: Response Table for Signal to Noise Ratios

Level	Voltage (V)	Gas flow rate (l/m)	Wire feed speed (ipm)
1	53.83	54.31	54.44
2	55.79	54.74	56.64
3	54.24	54.81	54.78
Delta	1.96	0.50	0.24
Rank	1	2	3

Table 3: Result for Ultimate Tensile Strength, Vicker Hardness (VHN), and Toughness

Experiment No	Voltage (V)	Gas flow rate (l/m)	Wire feed speed (IPM)	UTS (MPa)	SNRA1	VHN	SNRA2	Toughness (Joule)	SNRA3
1	22	10	250	480	53.6248	190	45.5751	250	47.9588
2	22	15	300	453	53.1220	199	45.9771	262	48.3660
3	22	20	350	546	54.7439	177	44.9595	240	47.6042
4	23	10	300	636	56.0691	180	45.1055	180	45.1055
5	23	15	350	657	56.3513	187	45.4368	232	47.3098
6	23	20	250	559	54.9482	180	45.1055	176	44.9103
7	24	10	350	459	53.2363	179	45.0571	234	47.3843

8	24	15	250	546	54.7439	202	46.1070	230	47.2346
9	24	20	300	545	54.7279	187	45.4368	264	48.4321

3.1.1. Tensile strength

Ultimate tensile strength (UTS) was calculated experimentally, Taguchi technique was applied for analysis with support of ANOVA and mode of fracture was studied. On the basis of data analyzed, plots for S/N ratio are shown in fig 4.it is much cleared from fig 4 that third level of voltage (23V), the second level of gas flow rate (20 l/min) and third level of wire feed speed (350IPM) gives higher tensile strength.

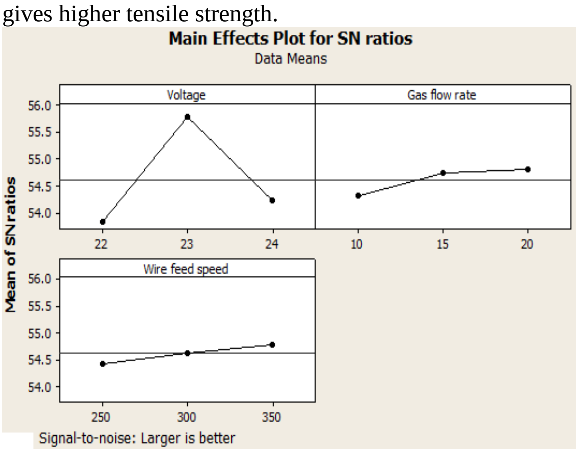

Figure 4: Main Effects Plot for SN ratios (UTS)

3.1.2. Hardness

Vicker hardness (VHN) of test samples also experimentally calculated, Taguchi technique was applied to determine the optimal process parameters with help of ANONA .on the basis of data analyzed, plots for S/N ratio are shown in fig 5. From fig 5 it is observed that and voltage (24V), second level of gas flow rate (15 l/min) and third level of wire feed speed (250IPM) gives normal values of hardness.

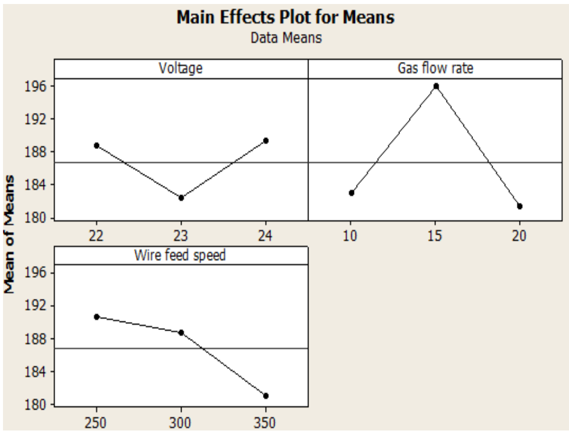

Figure 5: Main Effects Plot for SN ratios (VHN)

3.2. ANOVA-

Analysis of variance is a statistic technique, which is used to evaluate the differences between the mean and their associated procedure. ANOVA result for Ultimate tensile strength (UTS) is given in table 5, shows that Arc voltage has the most significant effect with 63.72%, while gas flow rate and wire feed speed having least effect.

Table 5: Analysis of Variance for SNRA1 (UTS), using Adjusted SS for Tests

Source	DF	Seq SS	Adj SS	Adj MS	F	P	% Contribution
Arc voltage	2	26153	26153	13076	2.09	0.324	63.72
Gas Flow rate	2	1358	1358	679	0.11	0.902	3.31
Wire feed speed	2	1013	1013	506	0.08	0.925	2.47
Error	2	12521	12521	6260			30.50
Total	8	41044					

ANOVA for S/N ration for hardness is summarized in Table 6 and it is observed that gas flow rate has the most significant effect with 60.49% contribution followed by arc voltage 25% contribution, while wire feed speed having least effect.

Table 6: Analysis of Variance for SNRA2 (Hardness), using Adjusted SS for Tests

Source	DF	Seq SS	Adj SS	Adj MS	F	P	% Contribution
Arc voltage	2	89.56	89.26	44.78	13.0	0.071	14
Gas Flow rate	2	386.89	386.89	193.44	56.16	0.017	60.49
Wire feed speed	2	156.22	156.22	78.11	22.68	0. 042	24.43
Error	2	6.89	6.89	3.44			1.1
Total	8	639.56					

4. Mode of fracture

4.1. Fracture mode of the tensile test specimen

Fracture mode of the tensile test specimens was studied by SEM apparatus at room temperature. The fracture surface of SS304H welded joint obtained with MIG welding is shown in Fig 6. Mode of fracture of tensile test specimens is tried to understand by given Figure. Fig 6(b) shows the fractography of tensile fractured surface. It is very clear from the figure that mode of fracture was ductile with numerous dimples. It is also observed from the result that fracture pattern is not uniform; cleavage fracture is a tear type fracture. Cleavage and secondary cleavage are clearly visible in SEM image of the fracture surface.

4.2. Fracture mode of toughness test specimen

To determine the toughness "V" notch Charpy samples were prepared as per ASTM. Specimens after fracture are shown in fig 7. Toughness fractured specimens examined to determine the surface morphology.

Figure 8 (a) and (b) shows the images of fractography of impact charpy "V" notch test piece. Sample 1 in Figure 8 shows the ductile fracture with coarse dimples. Enough finer dimples are observed in sample 3 in figure 8.combined ductile and brittle fracture mode formation is responsible for poorly absorbed energy. Sample 2 shows shallow dimples.

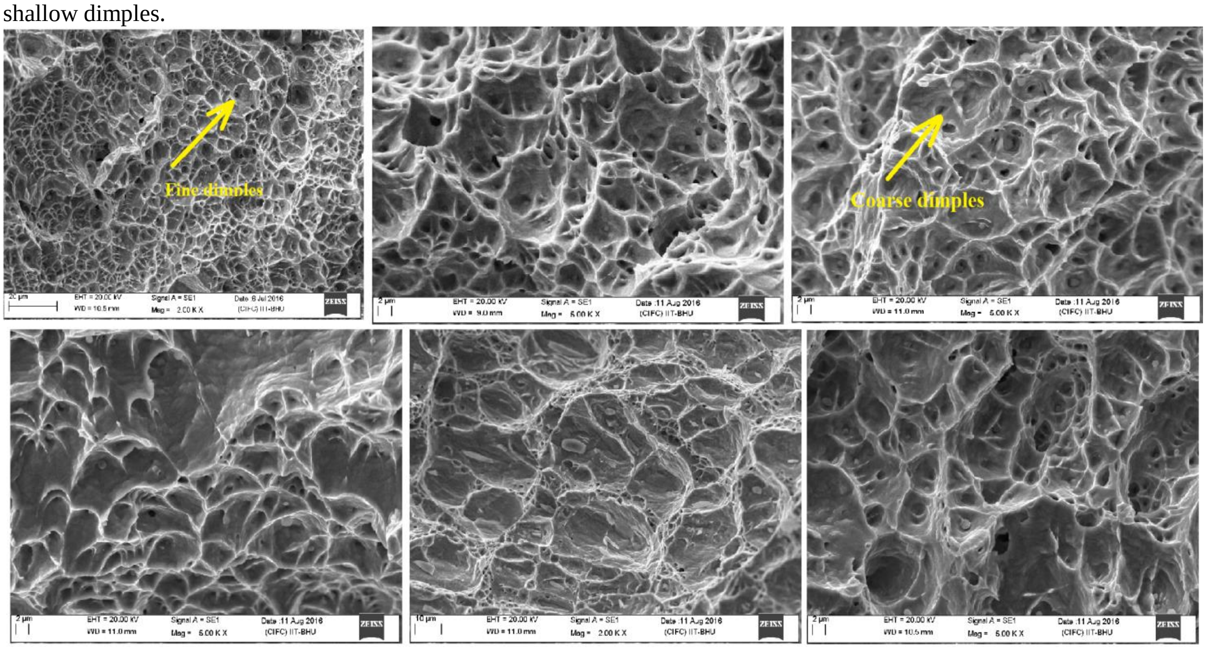

Figure 6: Fractograph morphology (SEM) of tensile test specimens

(a) Toughness test before fracture

(b) Toughness test after fracture(Centre)

Figure 7: Toughness test samples

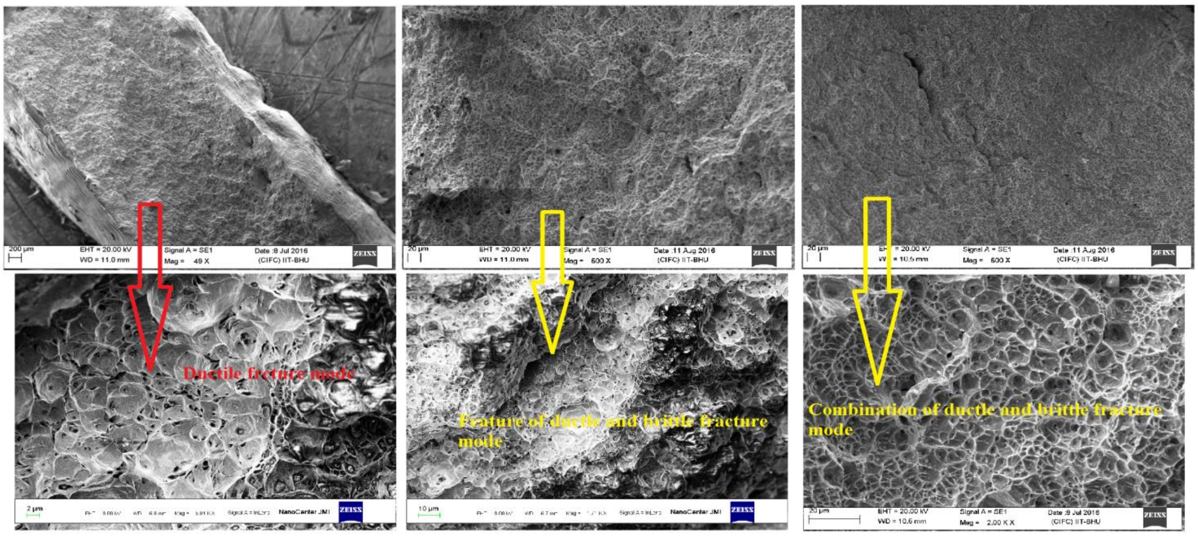

Figure 8: Macro images and SEM images of Impact fracture samples for morphology

5. Conclusions

In this study to investigate the effect of GMAW processes on different welding parameters and fracture mode characterization was studied. The variables parameters in this experiment were arc voltage, wire feed speed, and gas flow rate. In this conclusion it found that:

- In this experimental work, the selection of the process parameters for MIG welding of SS 304 weldment with the optimal mechanical quality has been presented.
- Weld bead surface finish is better by this process.
- It is also observed from experimental work that mechanical properties and microstructure of weldments depend on the heat input.
- It is also observed from fractograph morphology (SEM) of tensile test specimens that small dimple size or high dimple size are responsible for fracture.
- SEM analysis of fractured samples fracture morphology shows coarse dimples with the combination of ductile and brittle fracture in impact toughness weldment samples
- Deeper penetration is achieved in this process.
- Taguchi technique is method power pull tool to discover the effect of welding process parameters on mechanical quality.
- It is also observed that from the SEM result that if the dimple size is smaller, the strength and ductility of weldments is higher.
- ANOVA (Analysis of variance) depicts that Arc voltage having a significant parameter that affects the UTS and VHN followed by gas flow rate and wire feed speed
- Ductile fracture mode observed with fine dimples for tensile test samples.

References

[1] Saadat Ali Rizvi, S.P Tewari, Wajahat Ali, Advanced Welding Technology, Kataria & Sons (P) Ltd., New Delhi 2009, P45

[2] H.R. Ghazvinlo, A.Honarbakhsh and N. Shadfar, Effect of Arc Voltage, Welding Current and Welding Speed on Fatigue Life, Impact Energy and Bead Penetration of AA6061 joints Produced by robotic MIG Welding, *Indian Journal of Science and Technology*, Vol: 3, Issue 2, 2010

[3] Ramazani, A., Mukherjee, K., Abdurakhmanov,A., Prahl, U., Schleser, M., Reisgen, U. Bleck, W, Micromacro-characterization and modeling of mechanical properties of gas metal arc welded (GMAW) DP600 steel. *Material Science & Engineering A* (2014) 589: 1–14.

[4] http://www.aperam.com/uploads/stainlesseurope/TechnicalDataSheet/FT%20aust%C3%A9nitiques/Anglais/304%20UK.pdf.

[5] Dinesh Mohan arya,Vedansh chaturvedi , Jyoti Vimal, " Parametric Optimization of MIG process parameters using Taguchi and Grey Taguchi analysis", *International Journal of Research in Engineering and applied sciences.* Vol. 3, Issue 6. 2013, 1-17

[6] Nabendu Ghosh, Pradip Kumar Pal, Goutam Nandi, Parametric Optimization of MIG Welding on 316L Austenitic Stainless Steel by Grey-Based Taguchi Method, *Procedia Technology* Vol.25 (2016) 1038 – 1048

[7] Vikas Chauhan and R. S. Jadoun, Parametric Optimization of Mig Welding For Stainless Steel (SS-304) and Low Carbon Steel Using Taguchi Design Method, *International Journal of Recent Scientific Research* Vol. 6, Issue, 2 (2015), 2662-2666

[8] Abhishek Prakash, Raj Kumar Bag, Papin Ohdar, Siva Sankar Raju, Parametric Optimization of Metal Inert Gas Welding By Using Taguchi Approach, *IJRET*, Volume: 05 Issue 02,(2016),176-181

[9] S. M. Bayazida , H. Farhangia , A. Ghahramani, Investigation of friction stir welding parameters of 6063-7075 Aluminum alloys by Taguchi method, *Procedia Materials Science* 11 (2015) 6 – 11

[10] Saurav Datta & Asish Bandyopadhyay, Pradip Kumar Pal, Grey-based Taguchi method for optimization of bead geometry in submerged arc bead-on-plate welding, *Internatonal Journal of Advanced Manufacturing & Technology* (2008) 39:1136–1143

[11] Diganta Kalita, P.B Barua, Taguchi Optimization of MIG Welding Parameters Affecting Tensile Strength of C20 Welds, *IJETT* – Vol.26, (2015) 43-49

[12] ASTM E8/E8M − 11. Standard Test Methods for Tension Testing of Metallic Materials. ASM International; 2013

[13] Sagar R.Chikhale, Kishor P.Kolhe, Pawan Kumar," Prediction of Mechanical properties of Al Alloy 6061-T6 by using GMAW" *International Journal of Current Engineering and Technology*, Issue-5,(2016) 300-306

[14] Saadat Ali Rizvi,S.P Tewari,Wajahat Ali," Application of Taguchi technique to optimize the Process Parameters of MIG Wedging on IS2062 Steel" *International Journal on Emerging Trends in Mechanical & Production Engineering*" Vol. 2, Issue 2 (2016)1-11

[15] Emmanuel O. Ogundimu, Esther T. Akinlabi, Mutiu F. Erinosho, Study on Microstructure and Mechanical Properties of 304 Stainless Steel Joints by TIG–MIG Hybrid Welding, *Surface Review and Letters*, Vol. 25, No. 4 (2018) ,1-4

[16] Woei-Shyan Lee, Jen-I Cheng, Chi-Feng Lin,Chen-Yang Liu, Dynamic Mechanical Properties and Fracture Behavior of a 304L Stainless Steel GTAW Joint under Shear Conditions, *Materials Transactions*, Vol. 44, No. 12 (2003),2637-2645

[17] Uğur ÇALIGÜLÜ, Halil DİKBAŞ, Mustafa TAŞKIN, Microstructural Characteristic of Dissimilar Welded Components (AISI 430 Ferritic-AISI 304 Austenitic Stainless Steels) by CO_2 Laser Beam Welding (LBW), *Gazi University Journal of Science*, Vol. 25,Issue 1, (2012),35-51

[18] Anmol jeet Singh,Rutash Mittal, Experimental Analysis on TIG welding process parameters of dissimilar metals SS304-SS202 using Taguchi Method, *International Journal of Engineering and Manufacturing Science*, Vol. 7, Number 2 (2017), 249-258

[19] Ýhsan Kirik, Niyazi Özdemýr, Effect of process parameters on the microstructure and mechanical properties of Friction-Welded joints of AISI 1040/AISI 304l Steels, *Materials and technology* 49:5, (2015), 825–832

[20] Ravindra V. Taiwade, Awanikumar P. Patil, Ravindra D. Ghugal, Suhas J. Patre, Ravin K. Dayal, Effect of Welding Passes on Heat Affected Zone and Tensile Properties of AISI 304 Stainless Steel and Chrome-Manganese Austenitic Stainless Steel, *ISIJ International*, Vol. 53, No. 1 (2013), 102–109

JJMIE

Volume 12 Number 1, June. 2018
ISSN 1995-6665
Pages 23 -31

Jordan Journal of Mechanical and Industrial Engineering

Finite Element Simulation and Prediction of Mechanical and Electrochemical Behavior on Crevice Corrosion in Sheet Pile Steel

Benamar Balegh [a,*], Habib Trouzine [b] , Youcef Houmadi [c]

[a] *Civil Eng Dep, Faculty of Technology, Sidi Bel Abbes University, Sidi Bel Abbes, Algeria*
[b] *LGCE Civil Engineering and Environmental Laboratory, Sidi Bel Abbes University, Algeria.*
[c] *SSL Smart Structures Laboratory, Ain Témouchent university center, Algeria*

Received 24 June 2017 *Accepted 21 June 2018*

Abstract

A finite element method is proposed for modeling the crevice corrosion effect on sheet pile steel, through a multiphysics field coupling techniques. In this paper, the results show that while a tensile strain enhances stress uniformly through sheet pile steel, an increasing depth of crevice corrosion results in a concentrated stress at localized corrosion. When the crevice corrosion is under an elastic deformation, there is no apparent effect of mechanical–electrochemical interaction on corrosion. However, when the applied tensile strain on the side of crevice corrosion is enough to produce a plastic deformation, corrosion activity is also increasing.

Keywords: *Sheet pile steel; Mechano-electrochemical behaviour; modelling studies; Crevice corrosion.*

1. Introduction

Corrosion of sheet pile steel is the term which is usually given to the level that is higher than expected corrosion loss. In an advanced state, typically after many years of exposure, this vertically oriented differential corrosion along the sheet pile length causes localized crevice of the wall thickness. Such crevice and loss of sheet pile wall thickness can have a significant effect on the structural capacity wherever the place of the crevice occurs. The general pattern of crevice corrosion is remarkable [1]. For U-profile sheet piling the perforations occur predominantly on the out-pans, while for Z-profile piles perforation appears to occur predominantly as elongated slots on the web of the Z shape as shown in Figure 1[2, 3]. In practice the corrosion rate is also assumed to be a linear function of time by most researchers [4] and the values on corrosion rates are recommended [5].Corrosion behaviour of steel structural in soils, water, and air was studied with a specific conditions by means of several techniques also developed test method [6,7].

Many studies have mainly focused on the distribution of the electrical potential, current within the corrosion crevice, the mechanism and modeling of the phenomenon of cathodic protection [8,9]. Significant research has been performed in the past to understand the mechanisms of external corrosion of soil. Crevice with minimal overall metal loss of thickness can lead to the failure of structures because of several corrosion types that can stem from pitting corrosion such as stress corrosion [10].

It has been recommended that mechanisms are there to describe the initiation of crevice corrosion which is attributable to the development of a differential aeration cell with the subsequent acidification of the crevice solution and/or migration of aggressive anions [11–13],there have been a number of industrial codes/standards, such as Eurocode 3 [5], that can be used to evaluate remaining strength and failure under complex stress/strain conditions. However, this industry code was developed according to corrosion process and grades of steel and environment of corrosion (air, soil, water). Besides, this model usually provide prediction of behavior steel structures at a relatively high tolerance as reported in literature [14,15].

The simulating parameters include stress distribution, corrosion potential, and current densities as a function of the corrosion crevice size and tensile strain. It is anticipated that this research provides a sufficiently reliable method for simulation and prediction of crevice corrosion on sheet pile steel under complex stress and strain conditions, and develop recommendations to industry for risk assessment[16, 17]

In this paper, a finite element model is developed to study the mechanoelectrochemical effect of corrosion of a segment of sheet pile steel, under corrosion effects. The reliability of the model is validated by various mechanical, and corrosion measurements.

* Corresponding author e-mail: balegh.benamar@yahoo.com.

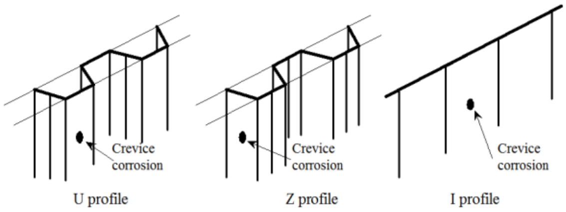

Figure 1: Sheet pile steel formed by U, Z and I profile piles and the types and locations of crevice corrosion.

2. Simulation

2.1. Boundary geometrical parameters

The simulation of mechanoelectrochemical effect of corrosion of sheet pile steel was performed. The geometrical model containing crevice corrosion is shown in Figure 1,where the segment of sheet pile thickness is 18 mm and, the length is 60mm for finite element simulation. The crevice corrosion on sheet pile wall is elliptically shaped, with a length of 2 mm, and its depths dt are:1mm, 1.75mm,2.5mm, 3.75mm respectively. This work assumes an unchanged length with growing depth for crevice corrosion in order to investigate propagation of the corrosion defect along the sheet pile direction.

The boundary condition of solution is that the solution boundary is electrically isolated, except for the steel interface that is set as a free boundary at right side. While the bottom segment is fixed, the left segments loaded with prescribed tensile strains as described below and is set as an electric grounding. Themesh type used is triangular. A full mesh consists of 977 nodes with 133 edge elements and 18 integration points. The maximum and minimum element sizes are 1.6 mm and 0.001 mm, respectively, with a maximum element growth rate of 1.3 also the predefined size is extremely fine. A stationary solver of and time dependent solver is selected for this case.

The geometry of sheet pile segment is simplified into a 2D model due to the symmetrical property, as shown in Figure 2. The finite element simulation contains two aspects, mechanical elasto-plastic solid stress analysis of the steel sheet pile and corrosion secondary potential and current density analyses [18]

2.2. Simulation of mechanical parameters

An elasto-plastic solid stress simulation was performed on sheet pile steel. The isotropic hardening model is used, E is Young's modulus of200GPa. Von Mises yielding criterions used for the elasto-plastic simulation then a stress is applied on the steel sheet pile along the longitudinal direction to simulate steel strainof5 MPa[20]. The total strain εis equal to the totaldeformation Δldivided by segment lengthl:

$$\varepsilon = \frac{\Delta l}{l} \tag{1}$$

2.3. Simulation of electrochemical corrosion parameters

The interface of secondary corrosion, found under the electrochemistry corrosion, deformed geometry branch when adding a physics interface, describes the current and potential distributions in corrosion under the assumption that the variations in composition in the electrolyte are negligible[20]. The physics interface can be combined with physics interfaces modeling mass transport to describe concentration dependent current distributions.

The electrochemical reactions of iron dissolution occur in the crevice according to:

Anodic reaction :

$$\mathrm{Fe(s)} \rightarrow \mathrm{Fe^{2+}(aq)} + 2\acute{e} \tag{2}$$

which Fe(s) is iron in solid state, Fe+2(aq) is iron in liquid state and é is electron

Experimental polarization data is used for this reaction, where the local current density of the reaction is evaluated as:

$$\mathrm{i_{Fe}} = \mathrm{f}(\,\varphi_{s-}\varphi_{l}) \tag{3}$$

The crevice corrosion is modeled as a porous electrode, with the specific surface area, and the electric potential is assumed to be constant over the crevice, solving for electrostatic potential φsis disabled in the solver[21].The problem is solved using a parametric sweep on a stationary solver, sweeping the potential in the electrode phase. The parametric sweep is needed to ensure that the intended active-to-passive polarization behavior is captured in the simulation, since due to the non-monotonic shape of the polarization curve the problem may have more than one solution. Several numerical models have been studied for describing crevice corrosion not only in the one-dimensional approximation, but also in the two and three-dimensional cases In concentrated solutions in the presence of chemical reactions and practically with arbitrary boundary conditions as it is reported to describe crevice corrosion models[22,23]. The FE simulation of mechanoelectrochemical effect of crevice corrosion of sheet pile steel was performed using a commercial COMSOL Multiphysics[24].

Table 1: Composition of steel sheet piling used in study measured by Optical Emission Spectroscopy (wt%) [19]

Profile	C	P	Mn	si	S	Ni	Cr	Mo	Cu	Al	V	Ti	Sn	Pb	Fe
U	0.1	0.069	0.87	0.173	0.021	0.47	0.09	0.05	0.55	0.003	0.021	0.004	0.019	-	Bal.
Z	0.1	0.073	0.86	0.165	0.023	0.47	0.08	0.04	0.58	≤0.005	0.021	0.002	0.017	0.01	Bal.

3. Experimental testing

Specimens used in this paper were cut from a sheet of sheet pile steel wall along circumferential direction, with achemical composition shown in Table 1. The specimen was machined into dumbbell shaped and itssurface was ground up[25].

The test solution was a near-neutral pH bicarbonate solution,i.e., NS4 solution, which has been used widely to simulate electrolyte. The solutioncontained 0.483 g/L NaHCO3, 0.122 g/L KCl, 0.181 g/L CaCl2_H2Oand 0.131 g/L MgSO4_7H2O, and was made from analytic grade reagentsand ultra-pure wateratambient temperature (22 C°).

The engineering stress–strain curve of sheet pile steel was obtainedby tensile testing through a Bose Electroforce dynamic materialstest system. Potentiodynamic polarization curve was measured on steelelectrode through a Solatron 1280C° electrochemical workstation after a steady-state corrosion potential was achieved upon immersing in NS4 solution for 1 h. The potential scanning ratewas 0.3 mV/s, and potential polarization started at 0.9 Vand ended at 0.6 V[26].

Mechanical properties of the steel and various electrochemicalcorrosion parameters derived from the polarization curve were used as initial conditions for FE. These included corrosion potential,corrosion current density.

4. Results and discussion

4.1. Von Mises stress under corrosion depth

Figure4 shows the distributions of Von Mises stress at the crevice corrosion under various corrosion depths.It is seen that, the local Von Mises stresslevelincreases apparently and is distributed symmetrically to the center of the crevice that the highest stress occurs at the crevice center.

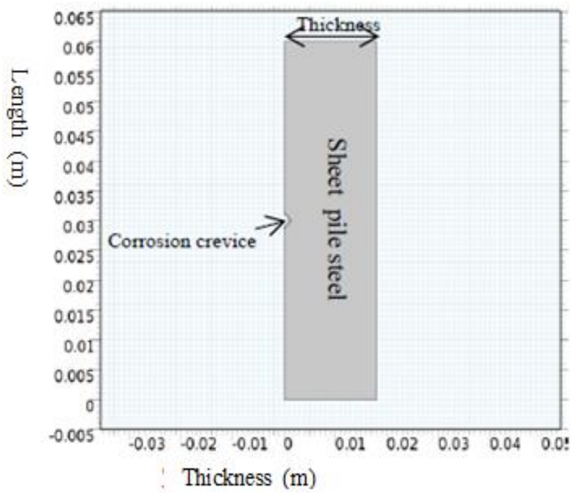

Figure 2: Geometry of model

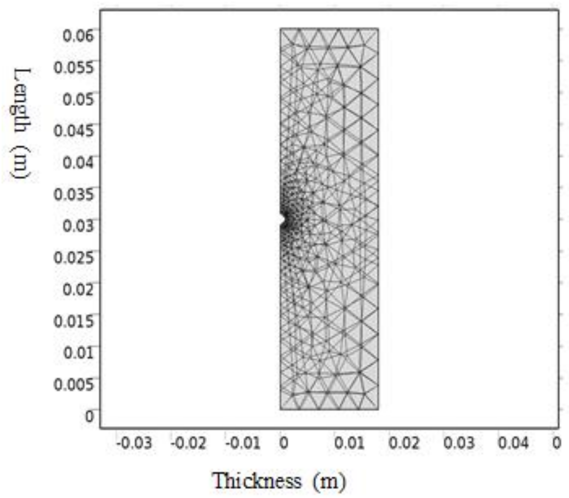

Figure 3: Meshing of model

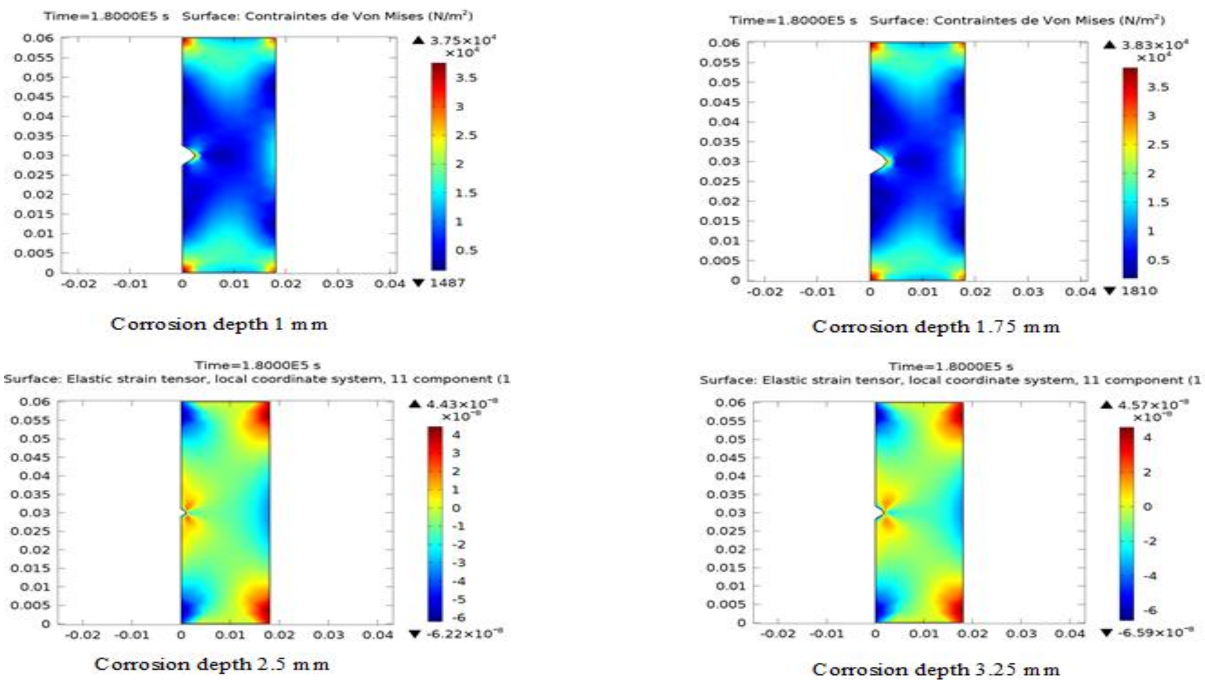

Figure 4: Distributions of Von Mises stress under various crevice corrosion.

4.2. Elastic strain under corrosion depth

Figure 5 shows the distributions of elastic strain tensor at the crevice corrosion under various corrosion depths. It is noticed, the local elastic strain level increases apparently at the opposite face of crevice corrosion as indicated by the red and dark red colors with minor change. It is seen that the strains is distributed symmetrically around the crevice that the highest stress locates at the center of crevice.

Figure 6 shows finite element simulating results of growth of von Mises stress values surrounding the crevice with increasing of depth corrosion in it. It is seen that the results obtained from simulation are well consistent with the experimental data, indicating the validity and reliability of the finite element model. The von mises stress is further enhanced becomes apparent, as indicated by vectors pointing from the crevice center to the sides. The deeper of corrosion crevice results the higher stress concentration.

Figure 7 shows also growth of elastic strain values surrounding the crevice with increasing of depth corrosion in it. It is seen that the results obtained from simulation are well consistent with the experimental data, indicating the validity and reliability of the finite element model. The elastic strain is further enhanced. The deeper of corrosion crevice results the higher strain concentration.

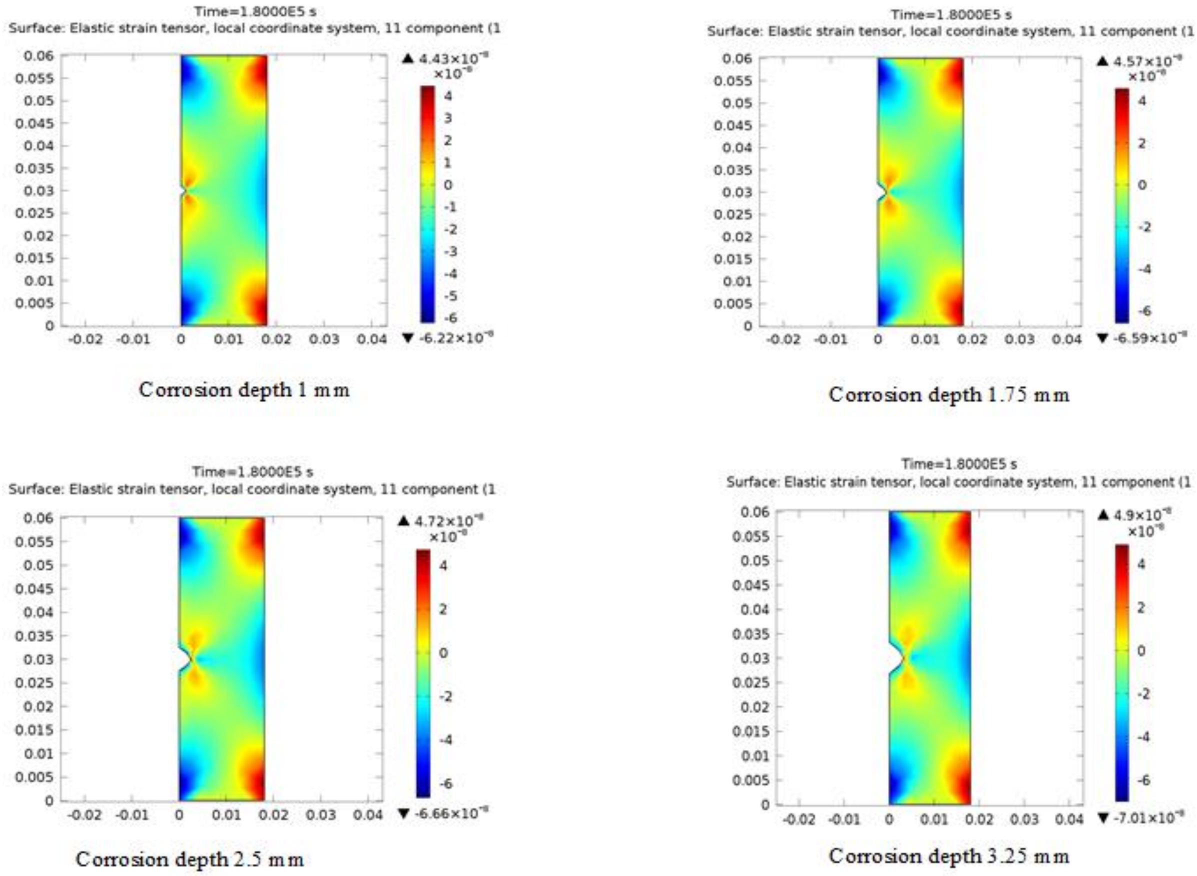

Figure 5: Distributions of elastic strain tensor under various crevice corrosion.

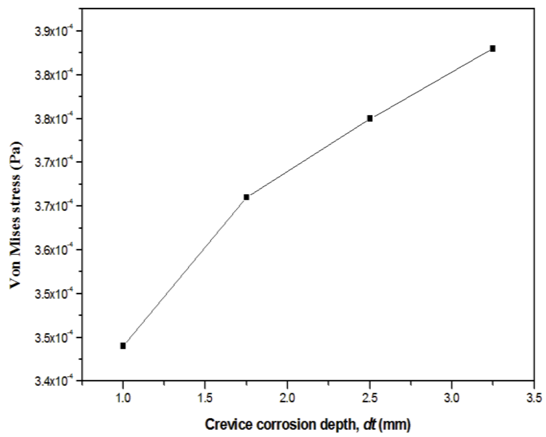

Figure 6: Linear distribution of von Mises stress along the bottom of crevice corrosion with various depths

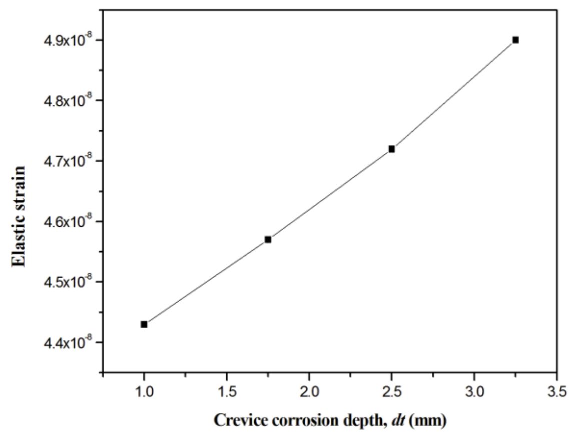

Figure 7: Linear distribution of elastic strain along the bottom of crevice corrosion with various depths.

4.3. .Von Mises stress under load

Figure 8 shows the distributions of Von Mises stress at fixed depth corrosion of 1mm under various applied load represented in active forces which is naturally variant along of high of sheet pile steel. It is seen that, the local Von Mises stress level increases apparently, and also it is distributed symmetrically to the center of the crevice, that the highest stress occurs at the crevice center.

4.4. Elastic strainunder load

Figure9 shows the distributions of elastic strain at the crevice corrosion under various applied load. The local elastic strain level increases apparently at the opposite face of crevice corrosion as indicated by the red and dark red colors.

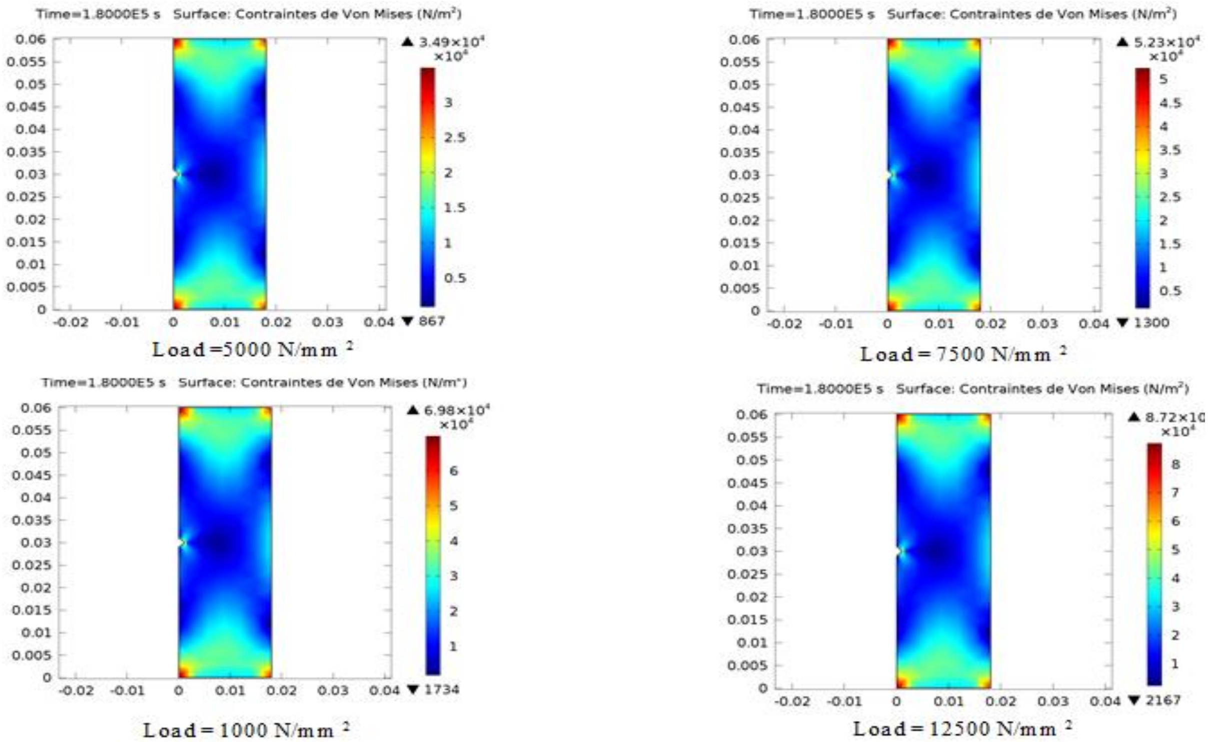

Figure 8: Distributions of von Mises stress at the corrosion crevice under various applied load.

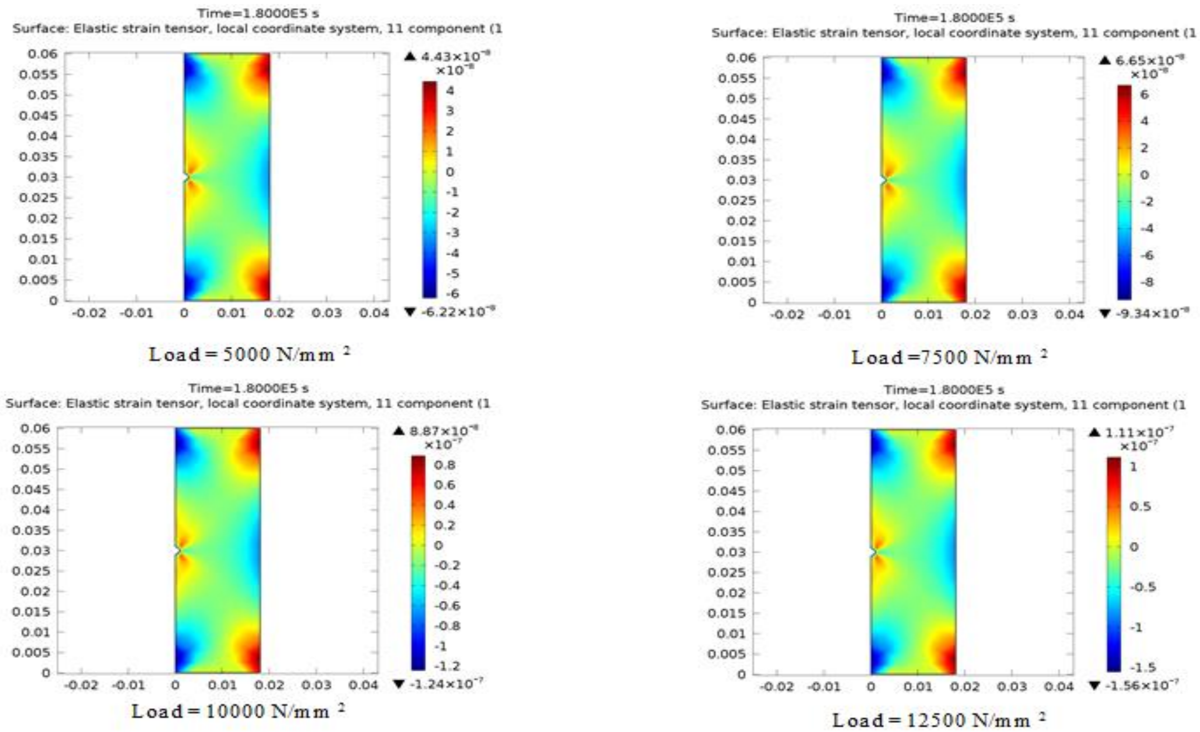

Figure 9: Distributions of elastic strain tensor at the corrosion crevice under various applied load.

Figures10,11 show finite element simulating results of growth of Von Mises stress and elastic strain values surrounding the corrosion crevice with increasing applied load. It is seen that the results obtained from simulation are well consistent, indicating the validity and reliability of the finite element model steel corrosion under mechanical–electrochemical interactions.

4.5. Electrolyte current density

Figure12 shows the distributions of electrolyte current *d*ensity at the crevice corrosion under various corrosion depths. The local electrolyte current *d*ensity level increases slightly at crevice corrosion as indicated by the red and dark red colors . It is seen that the electrolyte current *d*ensity is distributed symmetrically to the center of the crevice, and the highest electrolyte current *d*ensity occurs at the crevice center and the highest value 807 A/m^2 occurs at the small depth corrosion of 1mm, so there is inverse relationship between electrolyte current density and depth corrosion in steel.

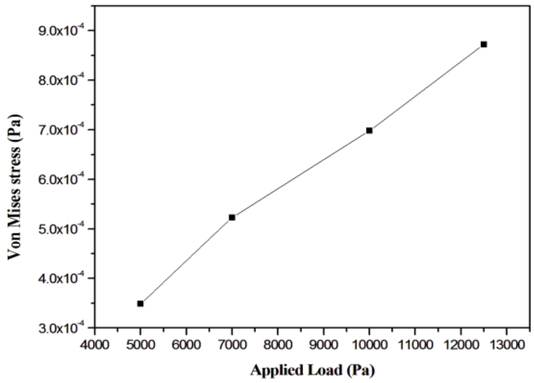

Figure 10: Linear distribution of von Mises stress along the bottom of crevice corrosion with various applied load.

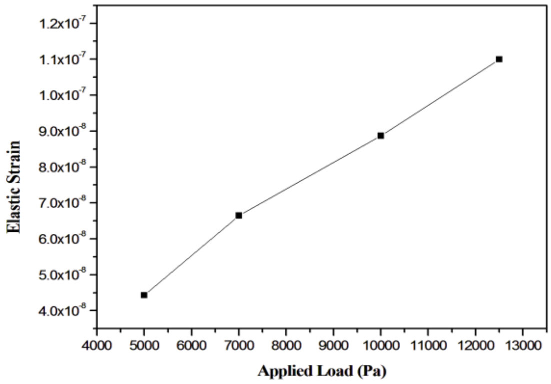

Figure 11: Linear distribution of elastic strain along the bottom of crevice corrosion with various applied load.

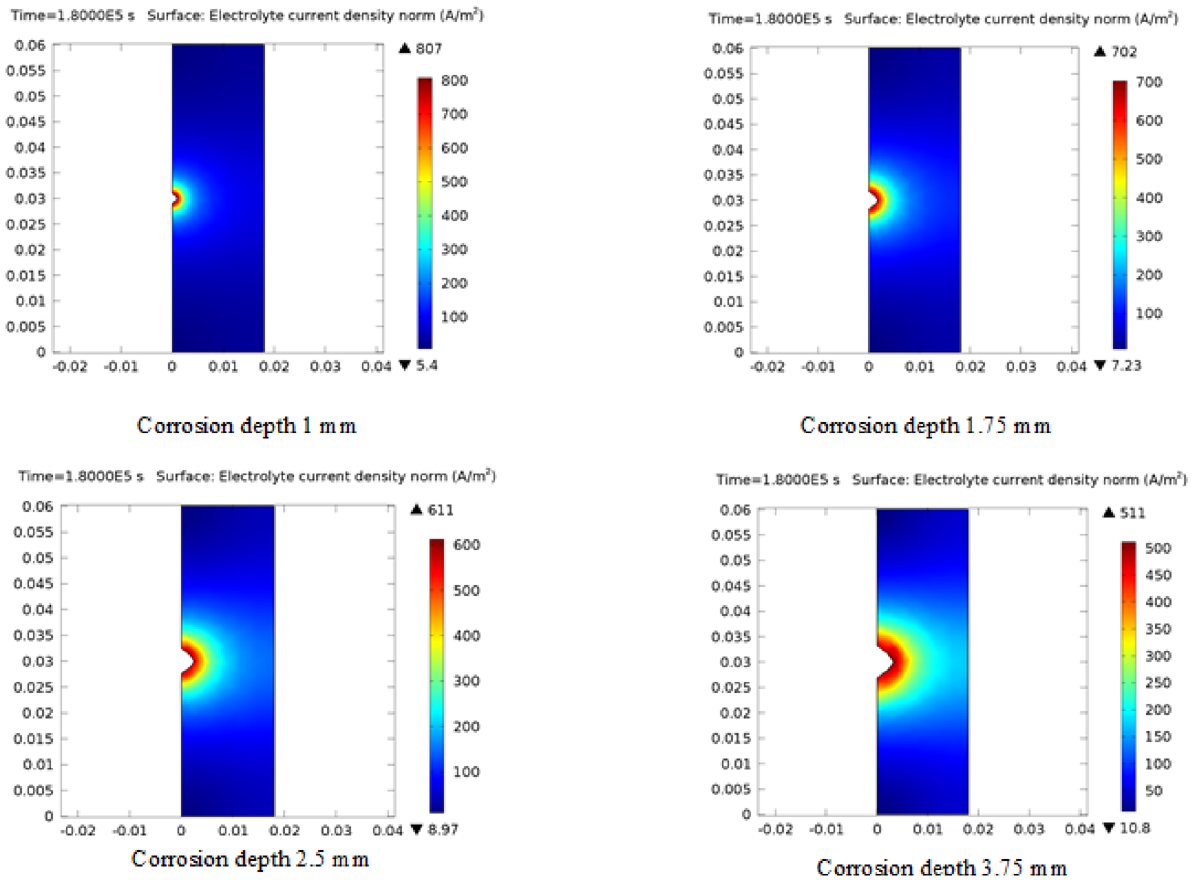

Figure 12: Distributions of electrolyte current density at the crevice corrosion.

4.6. Electrolyte potential

Figure 13 shows the distributions of electrolyte potential at the crevice corrosion under various corrosion depths. It is seen that, the local electrolyte potential level increases slightly at crevice corrosion as indicated by the red and dark red colors with minor change. While under growth of corrosion depth, it is recognized that the local electrolyte potential level increases remarkably surrounding the crevice corrosion as indicated by the red and dark red colors. It is seen that the electrolyte potential is distributed symmetrically to the center of the defect and the highest electrolyte potential occurs at the crevice center and the highest value 0.22 V occurs at the depth corrosion of 3.25 mm, so there is proportional relationship between electrolyte potential and depth corrosion in steel.

Figures14, 15 show finite element simulating results of current density and corrosion potential of corroded sheet pile steel model as a function of crevice corrosion depth, where the current density is decreased with crevice corrosion depth contrary what is concerning a corrosion potential which increase while a crevice corrosion is deepening.

Figures 16,17show finite element simulating results of current density and corrosion potential of corroded sheet pile steel model as a function of Von Mises stress, where the current density is the sum of anodic and cathodic current densities which also decrease with Von Mises stress contrary what is concerning a corrosion potential which increase with Von Mises stress.

It is seen that the results obtained from FE simulation are well consistent with the experimental data, indicating the validity and reliability of the FE model in prediction of sheet pile steel corrosion under mechanical–electrochemical interactions.

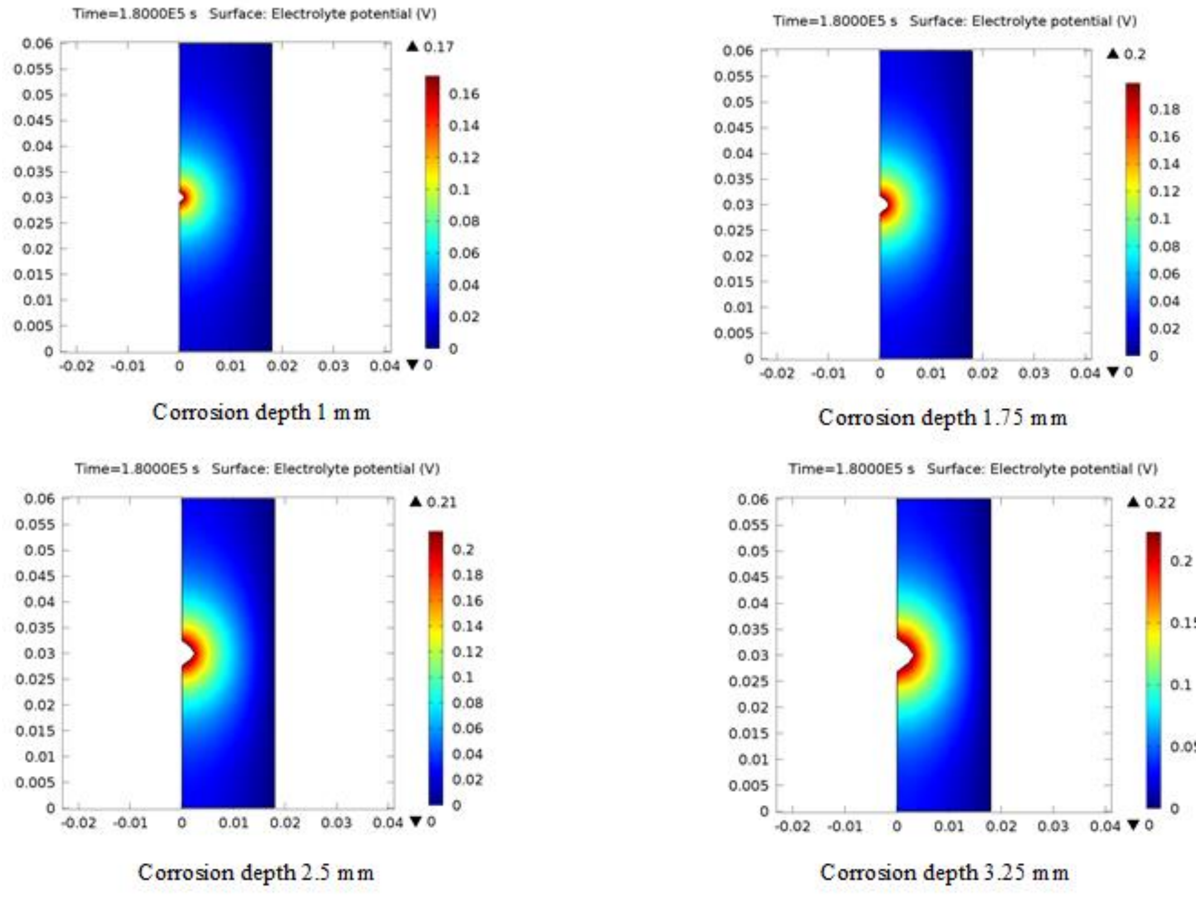

Figure 13: Distributions of electrolyte potential at the crevice corrosion.

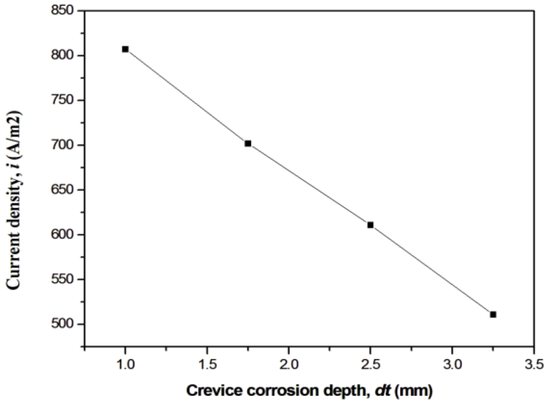

Figure 14: Linear distribution of current density along the bottom of crevice corrosion with various depth.

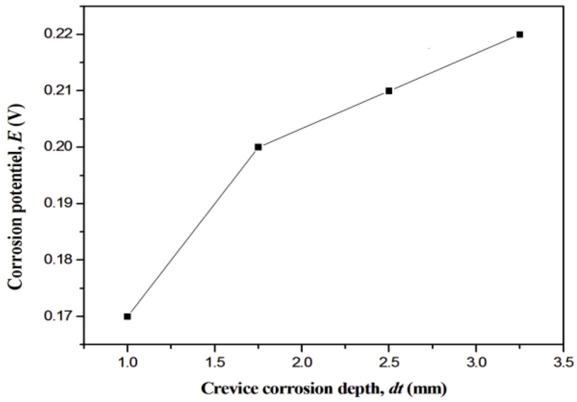

Figure 15: Linear distribution of corrosion potentiel along the bottom of crevice corrosion with various depth.

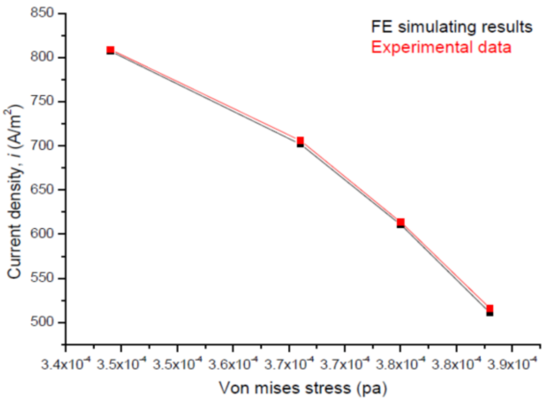

Figure 16: Linear distribution of Current density as a function of von Mises stress.

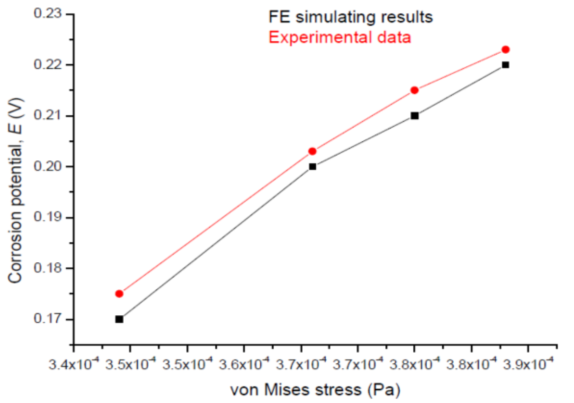

Figure 17: Linear distribution of corrosion potential as a function of von Mises stress.

5. Conclusions

- A finite element model is developed to study mechanoelectrochemical effect of corrosion crevice at sheet pile steel through a multiphysics coupling simulation. The model enables simulation of the synergism of stress concentration and localized corrosion in sheet pile steel, moreover there is no comparison between present study and previous work.
- An increase of longitudinal tensile strain and depth of crevice corrosion enhance local stress on sheetpile steel, However, their effects on stress distribution are not similar. While a tensile elastic strain results in an overall enhancement of stress through the sheet pile steel, the increasing corrosion depth causes a more concentrated stress at the crevice center. Stress at side of the crevice actually decreases.
- When corrosion depth is under local elastic deformation, there is no apparent mechanical–electrochemical interaction affecting local corrosion. When elastic strain or the corrosion depth is further increased to result in a local plastic deformation, the local corrosion activity is increased remarkably.
- The region with a high stress, such as the crevice center serves as anode, and that under low stress, such as the sides of the corrosion crevice, as cathode. Anodic dissolution at the crevice center is further accelerated, while it is mitigated slightly on the sides of crevice. The locally corrosion at the crevice center is further enhancedby the increasing depth of corrosion.
- An increasing depth of corrosion defect results in a concentrated stress at crevice corrosion. When the applied load on the side of geometry corrosion defect is sufficient to cause a plastic deformation at the crevice corrosion.

Acknowledgement

The research is supported by CNEPRU project. Our sincere thanks go to Civil Engineering & Environment Laboratory of Sidi Bel Abbes University and Smart Structures Laboratory at Ain Témouchent University Center, for the realization of this work.

References

[1] H. Shu,F.M. Al-Faqeer,H.W.Pickering,Pitting on the crevice wall prior to crevice corrosion: Iron in sulfate/chromate solution,Electrochimica Acta. 56(2011)1719-1728.

[2] E.Robert,A.Melchers,J.Robert,A.Jeffrey,M.Kayley,Localized corrosion of steel sheetpiling,CorrosionScience. 79 (2014)139-147.

[3] I.Beech,S.Campbell, Accelerated low water corrosion of carbon steel in the presence of a biofilm harbouring sulphatereducing and sulphur-oxidising bacteria recovered from a marinesediment,Electrochimica Acta. 54, 2008,14-21.

[4] H. Wall,L. Wadsö,Corrosion rate measurements in steel sheet pile walls in a marineenvironment, MarineStructure.33 (2013)21-32.

[5] European Committee for Standardization, Eurocode 3. Design of steel structures – part 5: piling, 2007

[6] G. Palumbo,J.Banaś,A.Bałkowiec,J.Mizera,U. Lelek-Borkowska,Electrochemical study of the corrosion behaviour of carbon steel in fracturing fluid,Journal of Solid State Electrochemistry. 18 (2014)2933-2945.

[7]E. Vannan, P. Vizhian,Corrosion Characteristics of Basalt Short Fiber Reinforced with Al-7075 Metal Matrix Composites, Jordan Journal of Mechanical and Industrial Engineering. 9 (2)2015,121-128.

[8] F.M.Song,Predicting the chemistry corrosion potential and corrosion rate ina crevice formed between substrate steel and a disbonded permeable coatingwith a mouth,CorrosionScience. 55 (2012)107-115.

[9] W.Sun,L.Wang,T.Wu,G.Liu,An arbitrary Lagrangian–Eulerian model for modelling the time-dependent evolution of crevice corrosion,CorrosionScience. 78 (2014)233-243.

[10] A.Turnbull,D.A.Horner,B.J. Connolly,Challenges in modeling the evolution of stress corrosion cracks from pits,Engineering Fracture Mechanic. 76 (2009)633-640.

[11] L.Y. Xu, Y.F. Cheng, Assessment of the complexity of stress/strain conditions of
X100 steel pipeline and the effect on the steel corrosion and failure pressure
prediction, in: Proc. 9th International Pipeline Conference, Calgary, Canada, (paper no. IPC2012-90087, 2012.

[12]F.P. Ijsseling, Survey of Literature on Crevice Corrosion, (1979–1998), Report EFC 30, The Institute of Materials, London, 2000.

[13] W.S. Tait, An Introduction to Electrochemical Corrosion Testing for Practicing Engineers and Scientist, 1st ed., PairODocs, Racine, WI, 1994.

[14] P.O. Gartland, Modeling crevice corrosion for Fe Ni Cr Mo in chloride solutions, in: 12th International Corrosion Congress, Houston, September,p. 1901, 1993

[15] G.A. Zhang, Y.F. Cheng, Micro-electrochemical characterization of corrosion of
pre-cracked X70 pipeline steel in a concentrated carbonate/bicarbonate solution,
Corrosion Science. 52 (2010) 960–968.

[16] Behrens D. DECHEMA Corrosion Handbook,Corrosive agents and their interaction with materials,Chlorine Dioxide and Seawater, 11,3-527-26662-3.Berlin ISBN, 1992.

[17] L.Y.Xu,Y.F.Cheng,Reliability and failure pressure prediction of various grades of pipeline steel in the presence of corrosion defects and pre-strain,International Journal of Pressure Vessels and Piping. 89 (2012)75-84.

[18] L.Y.Xu,Y.F.Cheng,Development of a finite element model for simulation and prediction of mechanoelectrochemical effect of pipeline corrosion,CorrosionScience. 73 (2013)150-160.

[19]GutmanEM.Mechanochemistry of Solid Surfaces. World Scientific Publication, Singapore; 1994

[20] G.R.Engelhardt,D.D.Macdonald,Possible distribution of potential and corrosion current density inside corroding crevices,Electrochimica Acta. 65 (2012)266- 274.

[21] J.C Walton,Mathematical Modeling of Mass Transport and Chemical Reaction in Crevice and Pitting Corrosion,CorrosionScience. 30 (8/9)(1990)915-928.

[22] Stewart K.Crevice Corrosion by Cathodic Focusing. PhD thesis, University of Virginia, 1999.

[23] http://www.virginia.edu/cese/research/crevicer.html;2002.

[24] COMSOL Multiphysics, version 4.3, www.comsol.com.

[25] L.Y.Xu,Y.F.Cheng,An experimental investigation of corrosion of X100 pipelinesteel under uniaxial elastic stress in a near-neutral pH solution,CorrosionScience. 59 (2012)103–109.

[26] L.Y.Xu,Y.F.Cheng, Corrosion of X100 pipeline steel under plastic strain in aneutral pH bicarbonate solution,CorrosionScience. 64 (2012) 145–152.

JJMIE

Jordan Journal of Mechanical and Industrial Engineering

Volume 12 Number 1, June. 2018
ISSN 1995-6665
Pages 33 - 43

Optimization Analyses of Parabolic Trough (CSP) Plants for the Desert Regions of the Middle East and North Africa (MENA)

Khaled M. Bataineh*, Ahmad Gharaibeh

Department of Mechanical Engineering, Jordan University of Science and Technology, Irbid- Jordan

Received 26 Nov 2017 *Accepted 21 June 2018*

Abstract

The objective of this study is to investigate the effectiveness of installing concentrating solar power plants in Middle East. A case study is performed for this purpose in the Ma'an area in southern Jordan. Due to water scarcity in most MENA region, contrasting analogy between hot and dry cooling is performed. The performance of CSP plant is simulated using SAM software. The simulation results predict that solar field size and thermal energy storage systems play major role in determining the energy cost. Moreover, it is found that larger plant size has lower values of levelized cost of energy (LCOE). Furthermore, LOCE for 50 MW using dry cooling ranges between 12.88 and 13.40 c$/kW, while it ranges between 11.23 c$/kW and 13.56 23 c$/kW for wet cooling. Finally, it is found that dry cooling option has a great economical potential for generating energy in water scare regions. Therefore, implementing optimal CSP plants in Maan area has great economic impact in Jordan's economic and reduces its dependent on imported oil.

Keywords: *Solar Energy; Electricity generation; Levelized Cost of Energy; LCOE, SAM..*

1. Introduction

Jordan depends on imported fossil fuels to meet its national energy demand [1]. The demand for primary energy has increased from 2.4 million toe in 1982 to 11.5 million toe in 2017. Jordan is experiencing an increased pressure on primary energy demand reaching up to 5.5%. It is expected that the demand for primary energy amounts will reach up to 15 million tons of oil equivalent in 2020 compared to 7.5 million tons of oil equivalent in 2008. The total electricity generation was approximately 8,447 GWh in 2004 while it reached 17,261 GWh in 2013 [5]. The electricity demand increase in Jordan is estimated around 7.4% [6]. On other word, an average of 300 MW per year of additional generated capacity is needed to meet the high electricity demand.

Jordan currently facing real challenges due to the high rates of energy demand, lack of available natural resources and the increase in the public debt which touched US$ 34 billion for the year of 2016 [7]. One promising way of facing these serious problems is utilizing renewable energy sources, which will help the government to achieve the national goals of a brighter future [8]. Jordan has great potential sources of renewable energy, particularly solar and wind energy. Until recently, Jordan experience in generating electricity from renewable energy sources is limited to laboratory scales [2-9]. It has been reported that only 2% of the total electricity is generated from renewable energy resources in 2005 [9-10]. Jordan's Energy Master Plan aims to increase the share of RE to 10% of Jordan's primary energy consumption by the year of 2020.The Jordanian government has estimated the size of investment in renewable energy to meet that share to 15 billion US$ [11].

The RE targets reported by the MEMR are 1000MW of Wind, 600MW of Solar, and 50MW by Biomass by 2020 [12]. According to annual report 2016 published by The Ministry of Energy and Mineral Resources MEMR, there are a long list of RE projects currently have been completed in the last few years (2013-2016) summarized as follows:

- 12 photovoltaic projects with a capacity of 200 MW to generate electricity have been achieved in 2016.
- The commercial operation of Philadelphia Solar Power Company PV project direct proposals Round I has been achieved in 22/10/2015 with a capacity of 10 MW in Mafraq.
- Jordan Wind Project Company JWPC has started the commercial operation of Tafila Wind Farm in 2015 with 117 MW of capacity
- Hundreds of small-scale renewable energy schemes (on-grid roof tops PV systemshave been installed reaching a total of 80 MW.

Other large RE generation projects of about 1600–2000 MWp are expected to follow before 2020 and the estimated capital investment in these projects exceeding US$ 3–4 billion [13].Figure 1 shows the energy mix in Jordan for the period between 2008 and 2020.

* Corresponding author e-mail: k.bataineh@just.edu.jo.

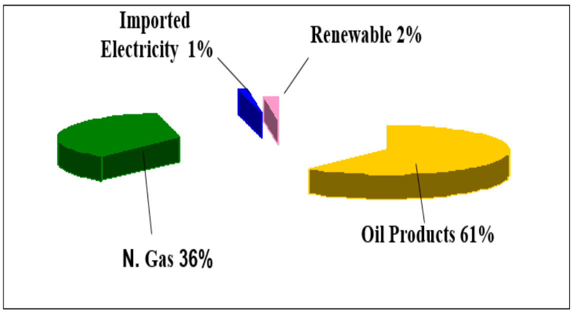

2008, Domestic Resources 4%, Imported 96%

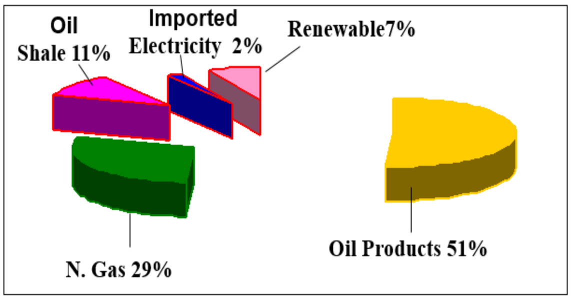

2015,Domestic Resources 25%, Imported 75%

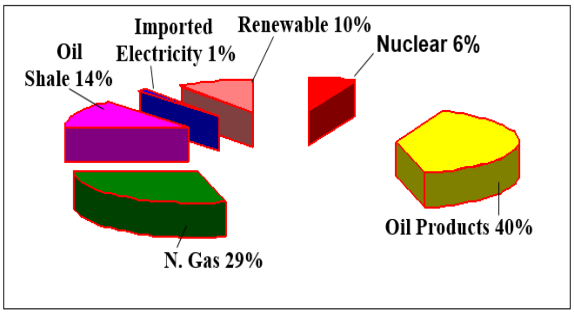

2020, Domestic Resources 39%, Imported 61%

Figure 1: The Energy Mix in Jordan (2008 – 2020) [12]

Recently, several studies for generating electricity utilizing different RE options are conducted in Jordan. Among all renewable energy resources available in Jordan to generate electricity, solar energy is found the most attractive option for generating electricity [14-16]. Although solar energy is totally renewable, but the solar power generates environmental impacts that need to be identified, quantified and evaluated. Life Cycle Assessment (LCA) has been successfully used to evaluate the environmental performance of renewable technologies [18, 19]. Furthermore, the environmental impacts of conventional CSP plants have been previously evaluated by the scientific based on LCAmethodology [20-25].

Electricity can be produced by different type of CSPP. The selection of CSP technologies depends mainly on working fluid, the desirable power output and the operating temperature [26-28]. The most widely used solar technology around the world is parabolic trough solar power plant (PTPP)[29]. It has been reported that for solar-thermal power plants operating at temperatures below 500°C, solar Rankine cycles using parabolic trough are appropriate [30-31].

The objective of this study is to assess the economic potential of installing parabolic trough solar power plant PTSPP in Jordan. For this purpose, a 50MW PTSPPis simulated using System Advisor Model program (SAM). Optimization of the main power plant components is carried out. The effect of thermal energy storage system (TES), type of cooling (dry or wet),and the size solar field on the plant performance and energy costare studied.Levelized cost of energy is used as the main criteria for optimization analysis. The objective of optimization is to determine the optimal configurations and components size that gives lowest LCOE.

2. Site

It has been reported that CSPP is economically viable when the average annual direct normal irradiation (DNI) above 2000 kWh/m2 [30]. Jordan is blessed with large amount of solar radiation reaching on average above 2000 kWh/m2 annually. The southern part of the country receives on average above 2500 kWh/m2[33]. Jordan is located in the middle east (31.5^0 N degree latitude, 36.1^0 E longitude), the annual average temperature and wind speed is 22°C,4 m/s at 10 m height respectively. Studying the map of solar irradiation over Jordan is a very crucial step in selecting potential sites for CSP plants.

Maan area which is located in the southern part of Jordan and receive around 2700 kWh/m2 is chosen for this study. The electricity transmission system in Jordan passes through this area. Considering the huge amount of solar radiation and the vicinity of the national electric grid, this selected site is considered the most attractive site in Jordan.

3. Methodology

The plant is geographically located at Maan city latitude 30.15^{0}N and longitude 35.75^{0}E. The elevation of the site ranges between 1065m and 1075m with flat terrain. A simulated CSP plant of 50 MW located in southern part of Jordan is considered in this study. The solar field size, the thermal energy storage size, and cooling options are considered optimization variables. The system advisor model (SAM) is used to simulate the CSP plant. It has been used by many researchers to simulate hourly transient behavior of CSP plant [34-37]. It allows investigating the effect of variations in physical, cost, and financial parameters on the performance outcome [34-35]. It produces comprehensive list of financial metrics for assessment[36]. The hourly data for the global, diffuse and direct irradiation, dew point, relative humidity, wind speed, atmospheric pressure and surface albedo are input to the SAM model. The measured weather data for the Maan for the year of 2014 is used in this study [31]. Results of solar radiation measurement are shown in Figure 2. The annual amount of global horizontal solar radiation is 6.46 Kwh/m²/day.

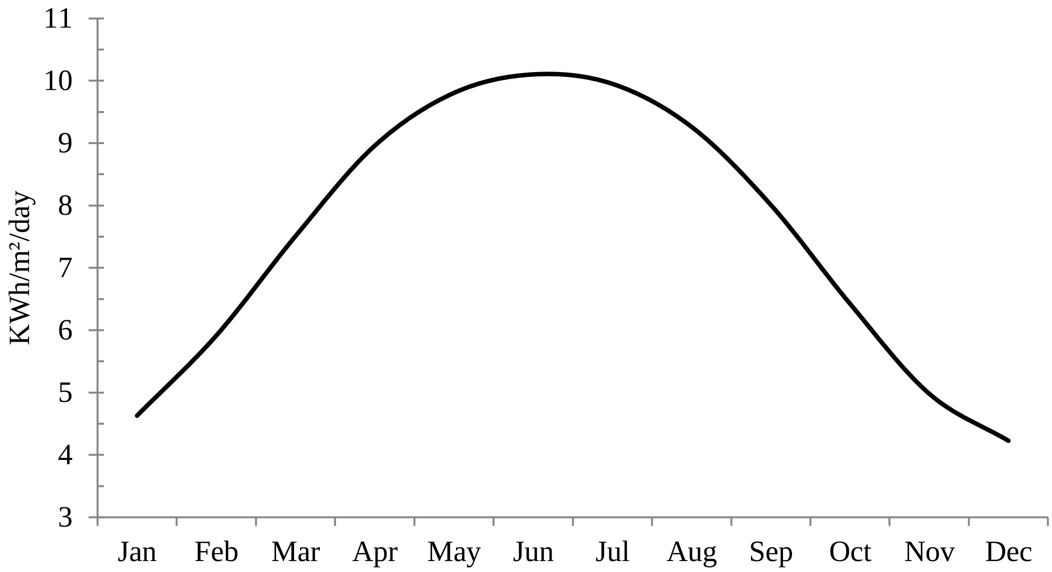

Figure 2: The amount of global horizontal solar radiation for each month.

4. Simulation and Optimization

A CSP plant with TES is simulated using SAM software. Table 1 lists the specifications for the main components of the simulated CSP plant in the selected site of Ma'an Jordan. A 50 MW plant capacity is considered. Dry and wet cooling are investigated. Table 2 lists the ranges of optimization variables simulated to determine the optimal configurations. The LCOE is taken as the objective function for the optimization problem. Furthermore, the relation between the plant size and the cost of energy production is studied. The plant costs for different configurations are listed in Table 3. High-performance cost effective Euro Trough parabolic trough collector models ET150 and ET151 have been chosen for solar collector assembly. Table 3 lists the cost of the main component of CSP. The cost of the components obtained from several sources have been updated in SAM. It is worth mentioning NREL's System Advisor Model (SAM) has updated the baseline cost for CSP plants in November 2015 [38]. According to the report the resulting new cost numbers reflect innovation and improvements in solar collector technology during the past several years. On the other hand, HTF, TES, and power block subsystems have been largely unchanged and have costs affected only by market and inflationary factors. Moreover, the site improvements and O&M fixed cost categories are dominated by labor costs. Construction and engineering labor cost indices have changed very little between 2012 and 2015.The Physical Trough Model "SkyTrough"was used to examine the impact of the revised cost values on LCOE, which is redefined in SAM 2015. This adjustment led to a change in the estimated real levelized power purchase agreement price from 14.9 ¢/kWh to 13.9 ¢/kWh.

The outputs of SAM simulation are validated against actual data obtained from Andasol plant located in Spain. Published plant data used is obtained from Herrmann et al. [34].To conduct plant simulations, all published plant specifications are simulated with SAM. Table 4 lists contrasting points between actual data and simulated data. It is clear that SAM was successfully able to predict actual data of the Andasol plant. Moreover, the percentage errors shown in the last column in table 4 indicate that SAM results are more conservative than actual data (all errors are negative).

Table 5 lists the LCOE values for each simulation runs. Figure 3 shows LCOE as function of SM for several values of a storage capacity in full load hours. As can be seen from table 5, for all TES sizes studied, the LCOE values decreases with increasing SM until certain value and starts rising again with further increase in SM. As can be seen from figure 3 for each TES size, there is an optimum value of SM where LCOE is minimum.

Table1: Specification for the main components of the CSP plants

Option	Heat Transfer Fluid	Collector	Receiver	Storage Media	Power Cycle
1	Molten Salt	Euro Trough ET150	Schott PTR70	Molten Salt	Nexant 450C HTF
2 ,3 &4	Molten Salt	Euro Trough ET151	Schott PTR71	Molten Salt	Dry Cooled SEGS Turbine

Table 2: Ranges of optimization variables

Option	Turbine Size (MW)	Cooling Option	Solar field size (solar multiple)	Thermal energy storage capacity (h)	Turbine gross efficiency (%)
1	50	Wet	1–2.5	0–12	39
2	50	Dry	1–2.5	0–12	37.3
3	100	Dry	1–2.5	0–12	38.1
4	150	Dry	1–2.5	0–12	38.25

Table 3: Cost data Input [34-38].

Economic inputs toSAM		
Direct Capital Cost	**Wet Cooling**	**Dry Cooling**
Site Improvements	30 \$/m²	30 \$/m²
Solar Field	150 \$/ m²	150 \$/ m²
HTF System	70 \$ / m²	70 \$ / m²
Storage	75 \$ / m²	75 \$ / m²
Power Plant	940 \$ /Kw	1160 \$/ Kw
Balance of plant	100 \$ / KWe	100 \$ / KWe
Contingency	6 % of direct capital cost	6 % of direct capital cost
Indirect Cost		
Engineer -Procure – Construct and owner cost	12% of direct capital cost	12% of direct capital cost
Land Cost	2 \$ / m²	2 \$ / m²
Sales Tax	6%	6%
Operation and maintenance Cost		
Fixed Cost By Capacity	60 \$ / KW – year	60 \$ / KW – year
Other Cost	60 \$ / KW – year	
Project Period (Year)	30	30
Discount rate %	6%	6%

Table 4: Simulation validation data.

Description	Unit	Simulated	Published data (Herrmann et al., 2002)	% (Simulated-published)/simulated
Annual DNI	KWh / m²	2052	2202	-7.31%
Annual electricity sold to the grid	MWh	153560	157,206	-2.37%
Annual parasitics received from the grid	MWh	0	4,307	Not applicable
Mean annual field efficiency	%	44.21	46.10	-4.28%
Annual overall efficiency	%	13.09	14.70%	-12.30%
Full load hours	h	3098	3144	-1.48%

Table 5: Optimization result.

LCOE Cent $ / KWhel		Solar Multiple - 50 MW / Wet Cooling								
		1	1.25	1.5	1.75	2	2.25	2.5	2.75	3
Number of storage full load hours	0	13.53	12.32	12.55	13.12	13.85	14.68	15.68	16.73	17.82
	1.5	14.04	12.53	12.34	12.67	13.18	13.85	14.61	15.45	16.37
	3	14.54	12.87	12.13	12.22	12.59	13.09	13.69	14.35	15.11
	4.5	15.00	13.22	12.13	11.92	12.14	12.51	13.00	13.55	14.18
	6	15.46	13.58	12.41	11.76	11.82	12.09	12.47	12.94	13.46
	7.5	15.92	13.93	12.71	11.86	11.62	11.76	12.06	12.44	12.88
	9	16.37	14.29	13.00	12.11	11.54	11.52	11.73	12.05	12.42
	10.5	16.83	14.65	13.29	12.36	11.73	11.40	11.52	11.77	12.09
	12	17.28	15.00	13.59	12.60	11.95	11.42	11.33	11.50	11.75
Number of loops		70	88	105	112	140	158	175	193	215

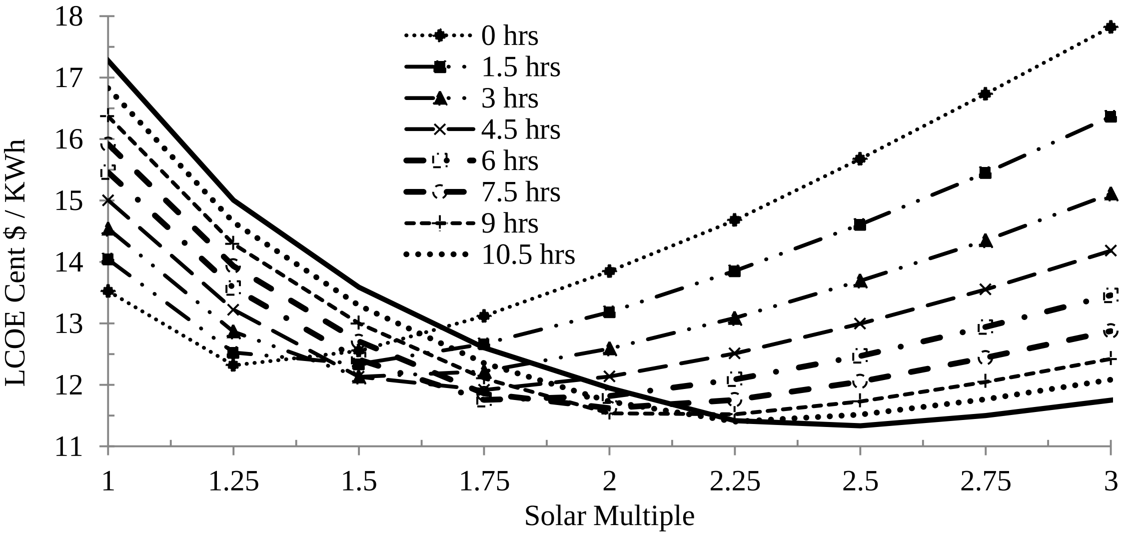

Figure 3: Variations of LCOE with solar field and TES sizes for wet cooling.

Simulation results presented in table 5 show that the minimum values of LCOE obtained for 1.5 <SM<2, and 6< TES< 9. The lowest value of LCOE is 11.54 c$/kWhel. Although practical optimum combination depends on operation schedule which are determined by national energy policy. Larger TES capacity should always be recommended. Therefore, combination of (SM = 2, TES = 9 full load hours) is considered the best combination in terms of energy cost.

Similar to the wet cooling optimization, a dry cooling optimization analyses are carried out for same plant size. Table 6 listssimulation results for several values of solar field and thermal energy storage sizes. The simulations results shown in figure 4 predict that wet and dry cooling have similar behavior. Generally, simulation runs predict that minimum values of LCOE can be obtained for combination of 1.5 <SM <2 and 6 hrs<TES< 9 hrs. Furthermore, optimal values for 50 MW that operates with dry cooling ranges between 13.08 and 14.85 c$/kWhel. The unit energy cost for dry cooling is only 1.5 c$/kWhel higher than those associated with wet cooling. Furthermore, this amount of cost should be considered when choosing between wet and dry cooling in dry hot regions.

In order to investigate the effect of size of the CSP plant on the energy cost and performance, optimizations of a dry cooled 100 and 150 MW CSP power plants are carried out. Procedure used for optimization analysis for 50 MW presented previously is repeated for larger plant size. Table7 shows the simulation results for 100 MW which are demontrated graphically in Fig.5. As can be seen in table 7 and figure5 minimum values of LOCE occur for 1.75 < SM< 2 and 6 <TES< 9. Simulation results predict that the lowest value of LCOE is 12.72 c$/kWhel for 100 MW plant. This value is lower than that corresponding to 50 MW plant size.

The simulation results for150 MW CSP plants are shown in Table 8 and Figure6. It is found that lowest values of LCOE occurs for 1.75 <SM< 2 and 6<TES<9. The LCOE varies from 12.69 to13.6 c$/kWhel, which shows a additional reduction in production costs with increasing plant size. It is worth mentioning that load management aspects and demand profiles should be considered when selecting the suitable plant size.

Table 6: Optimization results.

LCOE Cent $ / KWhel		Solar Multiple - 50 MW / Dry Cooling								
		1	1.25	1.5	1.75	2	2.25	2.5	2.75	3
Number of storage full load hours	0	15.59	14.14	14.39	15.02	15.87	16.84	18.00	19.24	20.54
	1.5	16.11	14.34	14.11	14.49	15.09	15.87	16.76	17.72	18.80
	3	16.69	14.73	13.85	13.95	14.38	14.95	15.65	16.42	17.30
	4.5	17.24	15.15	13.84	13.58	13.82	14.25	14.82	15.46	16.18
	6	17.78	15.57	14.17	13.38	13.45	13.76	14.20	14.74	15.33
	7.5	18.32	15.99	14.51	13.49	13.19	13.34	13.68	14.12	14.61
	9	18.86	16.41	14.85	13.78	13.08	13.05	13.28	13.64	14.06
	10.5	19.40	16.83	15.20	14.07	13.31	12.89	13.02	13.29	13.65
	12	19.94	17.24	15.54	14.36	13.56	12.90	12.79	12.97	13.25
Number of loops		70	88	105	112	140	158	175	193	215

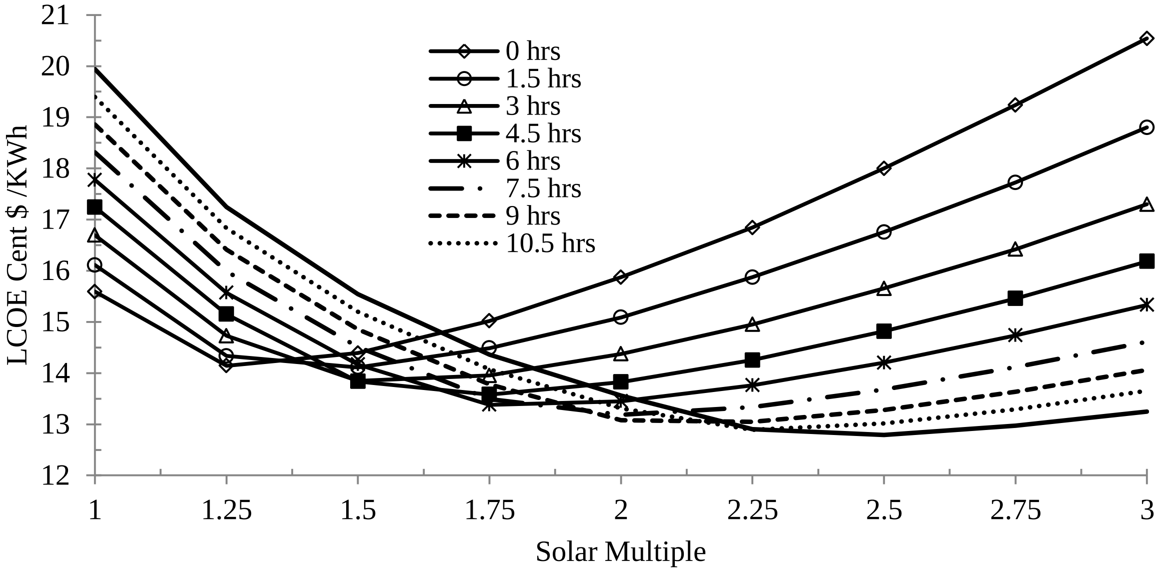

Figure 4: Variations of LCOE with solar field and TES sizes for dry cooling.

Table 7: Optimization results.

LCOE Cent $ / KWhel		Solar Multiple - 100 MW / Dry Cooling								
		1	1.25	1.5	1.75	2	2.25	2.5	2.75	3
Number of storage full load hours	0	15.58	14.13	14.38	15.01	15.86	16.83	17.99	19.23	20.53
	1.5	15.88	14.17	13.98	14.37	14.98	15.77	16.65	17.63	18.72
	3	16.42	14.53	13.71	13.83	14.27	14.86	15.57	16.34	17.22
	4.5	16.95	14.94	13.69	13.46	13.72	14.17	14.73	15.38	16.11
	6	17.48	15.36	14.02	13.26	13.34	13.66	14.10	14.64	15.24
	7.5	18.01	15.77	14.36	13.36	13.09	13.25	13.60	14.04	14.54
	9	18.54	16.19	14.70	13.65	12.98	12.96	13.21	13.57	13.99
	10.5	19.08	16.60	15.04	13.93	13.20	12.81	12.93	13.20	13.56
	12	19.61	17.02	15.38	14.22	13.45	12.81	12.72	12.90	13.18
Number of loops		128	159	191	223	255	287	318	350	392

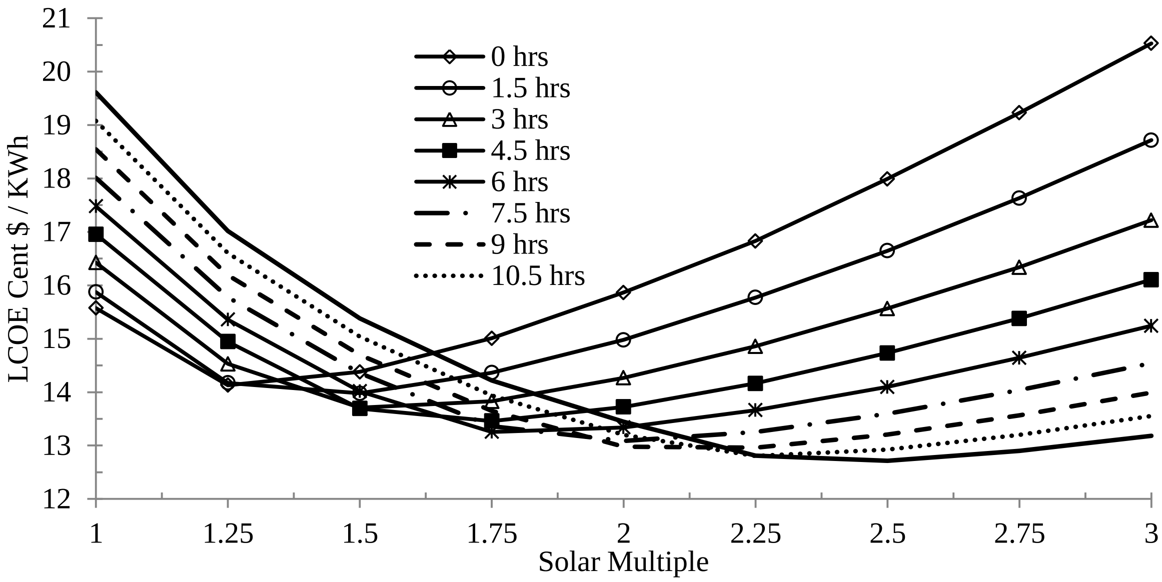

Figure 5: Variations of LCOE with SM and TES sizes for 100W plant (dry cooling).

Table 8: Optimization results.

LCOE Cent $ / KWhel		Solar Multiple - 150 MW / Dry Cooling								
		1	1.25	1.5	1.75	2	2.25	2.5	2.75	3
Number of storage full load hours	0	15.57	14.12	14.37	15.00	15.86	16.83	17.99	19.22	20.53
	1.5	15.79	14.11	13.93	14.32	14.94	15.74	16.62	17.60	18.69
	3	16.33	14.47	13.66	13.79	14.24	14.82	15.53	16.31	17.19
	4.5	16.87	14.88	13.64	13.42	13.69	14.13	14.70	15.36	16.08
	6	17.38	15.29	13.97	13.22	13.31	13.64	14.07	14.62	15.22
	7.5	17.91	15.71	14.30	13.32	13.06	13.23	13.58	14.02	14.52
	9	18.44	16.12	14.64	13.61	12.94	12.94	13.18	13.55	13.97
	10.5	18.97	16.53	14.98	13.89	13.16	12.78	12.90	13.18	13.53
	12	19.50	16.94	15.32	14.18	13.41	12.78	12.69	12.88	13.16
Number of loops		235	294	353	412	471	530	588	653	725

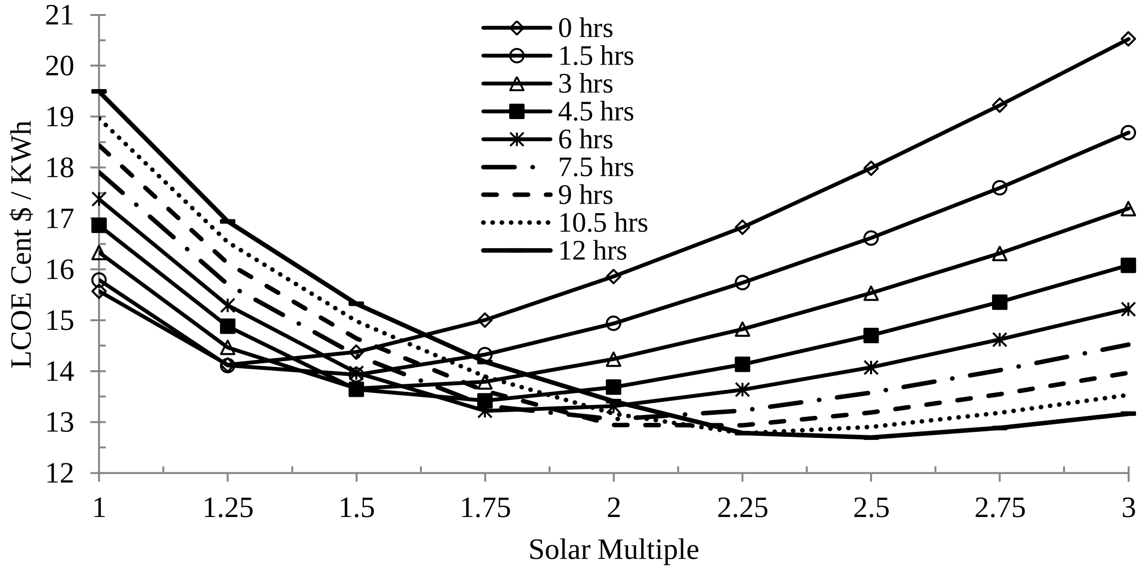

Figure 6: Variations of LCOE with SM and TES sizes for 150W plant (dry cooling).

5. Results and discussions

Simulation results presented in previous section indicate that CSP with a large TES has a great economic benefit. Generally, it is found that 9 hours of storage is the optimal size in terms of energy cost. Figure 7 shows the variation of LCOE with TES size. A large TES allows storing the surplus energy during daytime and reusing it during night. Therefore, TES has significant effect in increasing the capacity factor of the power plant and increase the economic attractiveness of CSP. Furthermore, due to high level of solar radiation in the considered site, LCOE values found attractive from economic point of view. Moreover, it is noticed that the LCOE for dry cooling is not significantly higher than the wet cooling, i.e. only in the range of 1.2 and 0.53 c$/kW h for the 150 and 50 MW CSP plants respectively as shown in Table 9. This slight increase in cost does not justify using wet cooling in dry hot arid regions.

Figure 8 shows the monthly specific net power generation (MW hel generated per MW installed) for optimized design options for all plant size studied. The simulation results predict that only small difference between cooling options in summer for different plant size, while the specific net power generation is same for the rest of the year. Figure 9 shows monthly overall plant efficiency. Simulation results show that for all power block sizes, the overall plant efficiency ranges between 7% to 20%. Moreover, simulations predict that larger power blocks have higher efficiency. This can be explained due to lower specific losses.

Due to the scarce of water in the study site, the cost of water is expected to be significant and should be included in the financial analyses. Water is used for wet cooling and cleaning of the collector mirrors. The cost of water delivery is 1.75$/m^3 (WAJ, 2015). Water cost should be added to the LCOE for both wet and dry cooled power blocks. It is assumed that washing takes place 65 times per year with amount of 0.7 L/m^2 of collector aperture area. The specific water cost for each option is calculated and added to the previously calculated LCOEs. LCOEs including water cost are shown in Table 9. For 50 MW plant, simulations predicts that about 92.6% of water use can be saved if dry cooling option is chosen. Results presented in Table 9 show that LCOEs for dry cooling is not significantly higher than that for wet cooling. Beside the water cost, the availability of water is a major problem in the waterless regions. Based on these results, dry cooling option is more economically appealing than wet cooling in hot sunny arid regions. This statement is very critical for Jordan which extremely suffers from lack of water.

Table 9 summarizes simulation results for the four different power plant options studied. Simulation predicts that the annual net electricity output for 50 MW CSP power plant for the two cooling options almost similar. The investment cost per installed kW for the four studied power plant options are shown in table 9. Including the cost of water, dry cooling option is lower than wet cooling option. The specific cost goes down as the size of the plant increases.

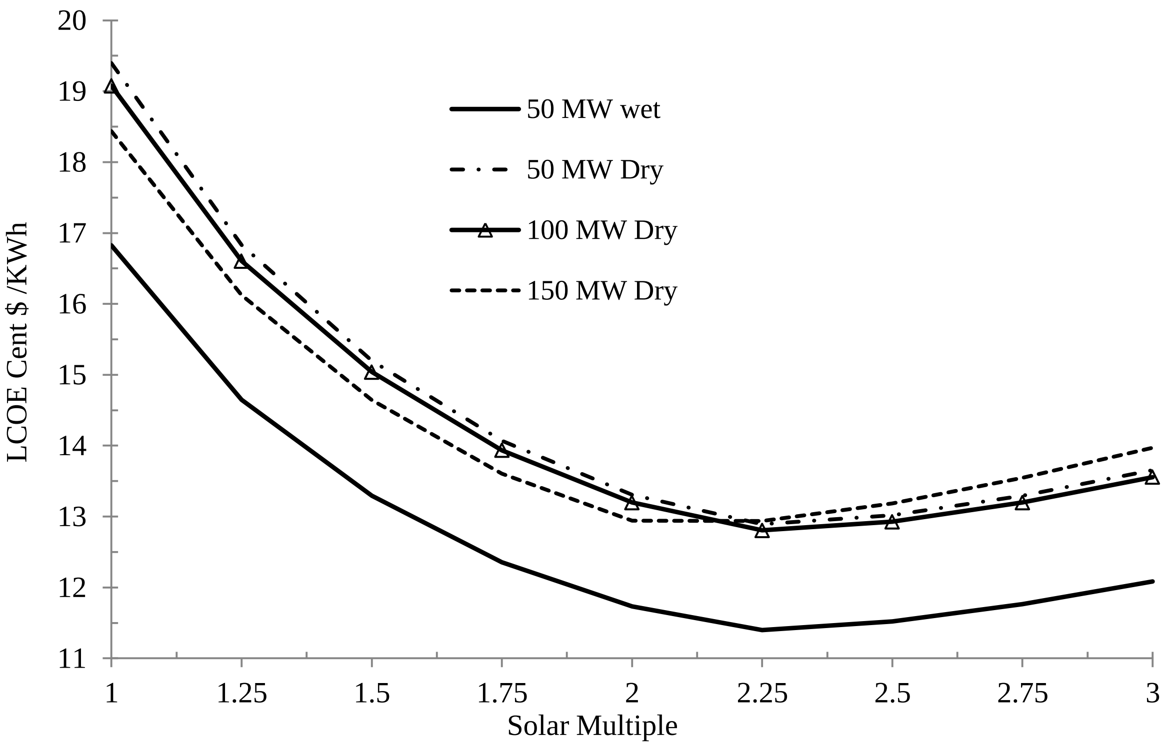

Figure7: Variation of LCOEwith SM (9 hour storage size)

Table 9: Results for different configurations

Description/ Cooling type	Unit	Plants in Maan - Jordan			
		50 MW wet	50 MW dry	100 MW dr	150 MW dry
		503,580	523,201	1,036,590	1,543,440
Collector area	m²	639,373	646,775	1,036,590	1,543,440
Annual thermal power	MWhth	210,993	206,968	1,302,438	1,972,709
Annual electricity output	MWhel	210,993	206,968	416,780	631,267
Capacity factor	%	48.2	47.6	47.7	48.1
Annual water consumption	m³	846868	61525	122571	183175
Levelized electricity cost	c$/KWh	11.54	13.08	12.98	12.94
Levelized electricity costs incl. water cost	c$/KWh	12.7	13.1	13	12.98
Net investment cost	$	277,758,272	292,801,600	577,758,272	857,715,008
Net investment cost /KW	$ / KWh	5,555	5,777	5,718	5,718
Net investment cost costs incl. water cost	$	319,678,238	295,847,088	583,825,537	866,782,171
Net investment cost /KW costs incl. water cost	$ / KWh	6393.56	5916.94	5838.26	5778.55

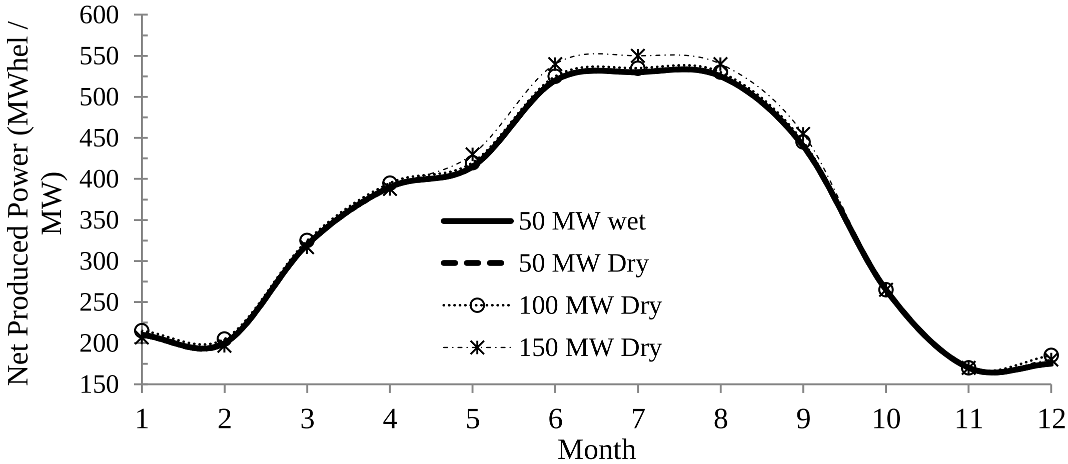

Figure 8: Monthly variations of net power generation at optimal values.

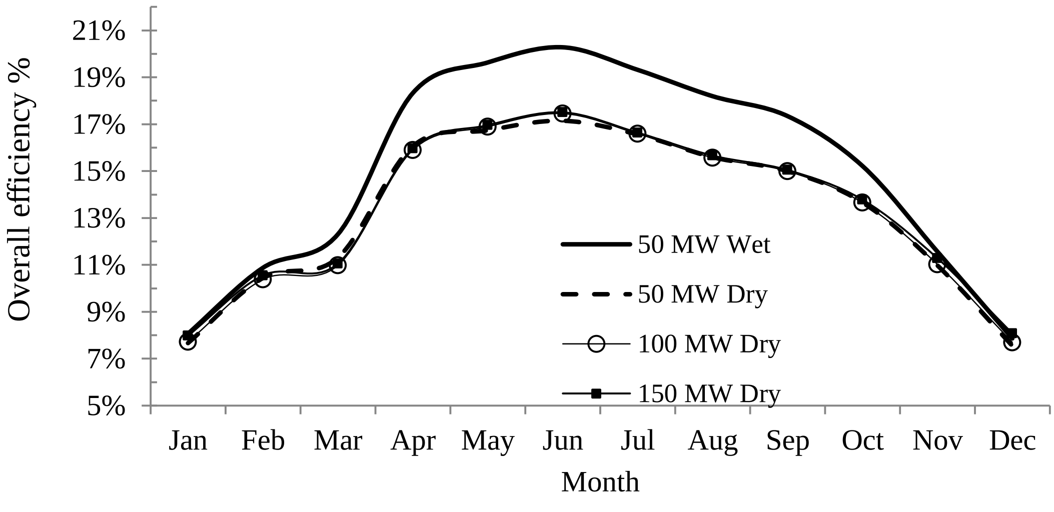

Figure 9: Overall efficiency for reference plant in Ma'an.

6. Conclusion

Optimization analyses for CSP plant located in southern part of Jordan using SAM software are presented. Size of solar field, thermal storage size, size of the power block, and type of cooling are considered the main design factors. The objective of optimization is to minimize the cost of energy production. It is found out that the thermal energy storage (TES) system has the greatest impact on CSP plants performance. It can be concluded that lowest values of LCOE and high capacity factor can be obtained when selecting 6<TES <9. Furthermore, LCOE decreases with increasing plant size. Moreover, dry cooling option is found feasible for regions with water scarcity. Finally, the study concluded that implementing optimal configuration of CSP plants in southern part of Jordan has great benefit to Jordan's economy, and thus it reduces its energy import.

References

[1] J. Jaber, A. Al-Sarkhi, B. Akash, M. Mohsen,"Medium-range planning economics of future electrical-power generation options". Energy Policy Vol. 32 (2004), 357–66.

[2] R. Mamlook,B. Akash, S. Nijmeh, "Fuzzy sets programming to perform evaluation of solar systems in Jordan". Energy Conversion and Management, Vol. 42 (2001),1717–26.

[3] E. Hrayshat, M. Al-Soud, "Solar energy in Jordan: current state and prospects". Renewable and Sustainable Energy Reviews, Vol.8(2) (2004),193–200.

[4] E. Hrayshat,"Analysis of renewable energy situation in Jordan". Energy Sources, Part B, Vol. 3 (2008), 89–102.

[5] J. O. Jaber, F. Elkarmi, E. Alasis, and A. Kostas, "Employment of renewable energy in Jordan: Current status, SWOT and problem analysis". *Renew. Sustain. Energy Rev.*, Vol. 49 (2015), 490–499

[6] O. Badrana, E. Abdulhadi, R. Mamlook, "Evaluation of Solar Electric Power Technologies in Jordan".Jordan Journal of Mechanical and Industrial Engineering, Vol. 4 (2010), 121 – 128.

[7] General Budget Department, Ministry of Finance, Draft Budget Law – 2016, Amman, Jordan (〈http://www.gbd.gov.jo/〉).

[8] J. Jaber, W. Awada, T. Rahmeha, A. Alawina, S. Al-Lubania, S. Abu Dalua, A. Dalabiha, A. Al-Bashirb, "Renewable energy education in faculties of engineering in Jordan: Relationship between demographics and level of knowledge of senior students". Renewable and Sustainable Energy Reviews, Vol.73 (2017), 452-459.

[9] National Electric Power Co. Annual report. Amman: NEPCO Press;(2005).

[10] Annual report, http://www.memr.gov.jo/echobusv3.0/SystemAssets/505997da-c229-4f65-8139-9ae8e45b0c78.pdf, retrieved in June, 2018.

[11] Central Electricity Generation Co. Annual report. Amman: CEGCO Press; 2005.

[12] Jordanian Ministry of Energy and Mineral Resources (MEMR), Updated Master

[13] Strategy of Energy Sector in Jordan for the Period (2007–2020), [Online Available]: ⟨http://www.nerc.gov.jo/Download/english%20-energy%20strategy.pdf⟩.

[14] F. El-Karmi,N. Abu-Shikhah, "Promoting renewable energy in Jordan by employing economic incentives". J Fundam Renew Energy Appl, Vol.4 (2014), 3–7.

[15] R. Mamlook, B. Akash,M. Mohsen, "A neuro-fuzzy program approach for evaluating electric power generation systems". Energy,Vol. 26 (2001), 619–32.

[16] B. Akash, R. Mamlook, M. Mohsen, "Multi-criteria selection of electric power plants using analytical hierarchy process". Electric Power Systems Research,Vol. 52 (1999), 29–35.

[17] J. Jaber, T. Sladek, S. Mernitz, T. Tarawneh, "Future Policies and Strategies for Oil Shale Development in Jordan". Jordan Journal of Mechanical and Industrial Engineering, Vol. 2 (2008), 31–44.

[18] M. Al-Soud, E. Hrayshat, "A 50 MW concentrating solar power plant for Jordan." Journal of Cleaner Production, Vol.17(2009), 625-635.

[19] E. Buonocore, L. Vanoli, A. Carotenuto, S. Ulgiati, "Integrating life cycle assessment and energy synthesisfor the evaluation of a dry steam geothermal power plant in Italy". Energy, Vol.86, (2015),476–487.

[20] M. Repele, G. Bazbauers,"Life Cycle Assessment of Renewable Energy Alternatives for Replacement of Natural Gas in Building Material Industry". Energy Procedia, Vol. 72, (2015), 127–134.

[21] Y. Lechon, C. Rua, R. Saez, "Life cycle environmental impacts of electricity production by solar thermalpower plants in Spain". J. Sol. Energy Eng. Trans., Vol. 130, (2008), 021012.

[22] J. Burkhardt, G. A. Heath, G.S. Turchi, "Life cycle assessment of a parabolic trough concentrating solar power plant and the impacts of key design alternatives". Environ. Sci. Technol. (2011), 45, 2457–2464.

[23] S.J. Klein, E. S. Rubin, "Life cycle assessment of greenhouse gas emissions, water and land use for concentrated solar power plants with different energy backup systems". Energy Policy, Vol. 63, (2013), 935–950.

[24] I.A. S. Ehtiwesh, M.C. Coelho, A.C. M. Sousa, "Exergetic and environmental life cycle assessment analysis ofconcentrated solar power plants". Renew. Sustain. Energy Rev., Vol. 56, (2016), 145–155.

[25] O. Behar, A. Khellaf, K. Mohammedi, "A review of studies on central receiver solar thermal power plants". Renew. Sust. Energy Rev., Vol. 23 (2013), 12–39.

[26] S. Kuravi, J. Trahan, D.Y. Goswami, M.M. Rahman, E.K. Stefanakos, "Thermal energy storage technologies and systems for concentrating solar power plants". Prog. Energy Combust. Sci., Vol. 39 (2013), 285–319.

[27] V. Siva Reddy, S.C. Kaushik, K.R. Ranjan, S.K. Tyagi, "State-of-the-art of solar thermal power plants—A review". Renew. Sust. Energy Rev. 27 (2013), 258–273.

[28] http://www.torresolenergy.com/TORRESOL/gemasolar-plant/enS.

[29] G. Franchini, A. Perdichizzi, S. Ravelli, G. Barigozzi, A comparative study between parabolic trough and solar tower technologies in Solar Rankine Cycle and Integrated Solar Combined Cycle plants." Sol. Energy, Vol. 98 (2013), 302–314.

[30] J. Liu, H. Chen, Y. Xu, L. Wang, C. Tan, "A solar energy storage and power generation system based on supercritical carbon dioxide". Renew. Energy, Vol. 64 (2014), 43–51.

[31] T. Markvart. Solar electricity. NY: John Wiley; (2002).

[32] F. Trieb, Concentrating solar power for the Mediterranean region. Stuttgart: German Aerospace Center; (2005).

[33] T. Key, Solar Thermal Electric Technology: (2006). Electric Power Research Institute. 2007.

[34] N. Blair, Cost and Performance System Advisor Model for All Solar Technologies. National Renewable Energy Laboratory, 2010.

[35] U. Herrmann, M. Geyer, R. Kistner, "The Andasol project-Workshop on Thermal Storage for Trough Power systems. SolarMillennium AG", FLABEG Solar International GmbH, 2002.

[36] Messai, Y. Benkedda, S. Bouaichaoui, M. Benzerga, " Feasibility Study of Parabolic Trough Solar Power Plant under Algerian Climate". Energy Procedia, Vol. 42 (2013), 73-82.

[37] Liqreina, L. Qoaider, "Dry cooling of concentrating solar power (CSP) plants, an economic competitive option for the desert regions of the MENA region." Solar Energy, Vol. 103 (2014), 417-424.

[38] L. Guzman, A. Henao, R. Vasquez, "Simulation and Optimization of a Parabolic Trough Solar Power Plant in the City of Barranquilla by Using System Advisor Model (SAM)". Energy Procedia, Vol. 57 (2014), 497-506.

[39] Parthiv Kurup and Craig S. Turchi,Parabolic Trough Collector Cost Update for the System Advisor Model (SAM), National Renewable Energy Laboratory, 2015, www.nrel.gov/publications.

JJMIE

Volume 12 Number 1, June. 2018
ISSN 1995-6665
Pages 45 - 50

Jordan Journal of Mechanical and Industrial Engineering

Effect of Water Column Height on the Aeration Efficiency Using Pulsating Air Flow

Ahmed A. Alkhafaji[a], Ammar A. T. Alkhalidi[b,*], Ryoichi S. Amano[a]

[a] *Department of Mechanical Engineering - University of Wisconsin-Milwaukee*

[b] *Energy Engineering Department - German Jordanian University*

Received 6 Dec 2017 *Accepted 21 June 2018*

Abstract

According to the United States environmental protection agency (EPA), a wastewater treatment plant is expected to remove at least 85% of the suspended solids and dissolved organic compounds from the wastewater before discharging it to a river or a lake. The aeration process is an integral part of any wastewater treatment plant, where suspended particles and dissolved organics are removed. The cost for aerating the wastewater is significant compared to other processes that take place in the wastewater treatment process. The normal operation of the aeration process is by compressing air continuously to basin diffusers, where the air is brought into contact with the water to provide the necessary oxygen for the microbial growth in the wastewater. Aeration systems utilize compressed air in pulsating flow mode have been proven to be more efficient than that of continuously compressed air. This study employs the wavy flow generated because of compressing the air alternatively (pulsating airflow) and investigate the effect of water column height on the oxygen transfer efficiency. Three water column heights are considered in this study, 0.6, 1.2 and 1.8 m, to investigate the effect of each water column on the SOTE at different airflow rates and pulsating times. The highest water column (1.8 m) gave better standard oxygen transfer efficiency (SOTE) results, but a better trend was observed for the lower water column at higher flow rates. The 1.2 m water column standard oxygen transfer efficiency was always taking an intermediate trend between the 0.6 m and the 1.8 m water columns SOTE. In addition, it was clearly shown that the best SOTE results for all water columns occur when the pulsating time equals 0.5 seconds.

Keywords: *wastewater treatment, aeration, standard oxygen transfer efficiency, pulsating airflow, mixing in the aeration ta*.

Nomenclature

AAA	Amano Alkhafaji Alkhalidi parameter, $4Q/\pi D^2 H$, 1/s
Co	Dissolved oxygen concentration at t = 0, mg/liter.
C∞	Dissolved oxygen concentration at saturation, mg/liter.
D	Diameter of water reservoir, m.
DO	Dissolved oxygen, mg/liter.
H	Height of the water column, m.
KLa	Overall mass transfer coefficient, 1/s.
KLa20	Overall mass transfer coefficient at 20ºC, 1/s.
OTE	Oxygen transfer efficiency.
OTR	Oxygen transfer rate, mg/s.
Q	Flow rate, L/min.
SOTE	Standard oxygen transfer efficiency.
SOTR	Standard oxygen transfer rate, mg/s.
t	Time, seconds.
T	Temperature, ºC
V	Volume of the water, liter.
$\dot{m}_{O_2}$	Mass flow rate of oxygen, mg/s.

1. Introduction

In secondary wastewater treatment, the aeration process has taken an important role, where the need for oxygen becomes vital to promote the microbial growth to suspend and efficiently separate the dissolved and suspended organic particles from the wastewater in the secondary clarifying treatment. Therefore, air and water need to be brought in contact in some container to have the transfer of oxygen molecules from the air to the water and provide the wastewater with the necessary oxygen for the aeration process. Two methods have been used in industry [1] to bring the air and water in contact; air diffusing systems and surface agitating systems. In the air diffusing systems, air diffusers are installed in a reservoir base. The compressed air is flowing out of these diffusers into the water in the reservoir. Surface agitating systems utilize the use of surface agitators to mix the water with the atmospheric air.

The air diffusing aeration system can be considered more efficient than the aeration system using surface agitation [1]. Nevertheless, both air diffusion and surface

* Corresponding author e-mail: Ammar.alkhalidi@gju.edu.jo.

agitation are consuming the most significant portion of the energy for any wastewater treatment process as shown in figure 1, [2]. Therefore, the best aeration system is an aeration system that requires the minimum energy to operate, and such aeration system can have a significant impact on the energy cost of the aeration process and hence the water treatment process. The EPA [3] reported that not less than 85% of the biodegradable and total suspended solids should be removed from the wastewater before discharging it to the lakes or rivers. Due to the population increase and the expansion in industry, the wastewater capacity that needs to be treated increases. The EPA's suggested technology increases the energy requirement for the aeration process to fulfill the EPA regulations. In other words, the energy consumption trend of the aeration process is growing with time. Therefore, it will be necessary to reduce that energy consumption by adopting new aeration design.

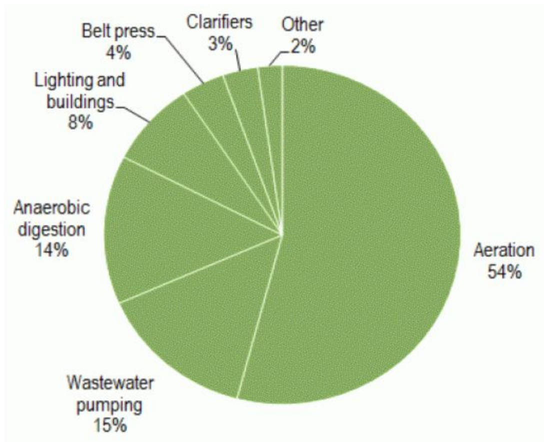

Figure 1: Energy consumption of a wastewater treatment process [3].

Many studies were made to optimize the aeration systems, but most of these studies discuss the effect of bubble size on the oxygen transfer rate between the air and water. The bubble formation is a very complicated process, and many mass transfer models have focused on the free rising of the bubble to determine the shape, surface area and the hydrodynamic behavior of the bubble. Higbie's [4] penetration theory combines a hydrodynamic and mass transfer model to determine the shape and mass transfer of a single growing bubble.

The effect of gas flow rate on the bubbles frequency was studied by Das et al [5]. A needle-type conductivity probe was used to estimate the bubbles frequency. The study showed that the bubbles frequency is increased by increasing the gas flow rate.

Colombet et al. [6] considered the liquid side mass transfer coefficient in a dense bubble swarm for a range of gas-liquid volume ratio between 0.45 and 16.5%. This study was performed in a square water column to measure the bubble size, shape and velocity at different gas flow rates by using a high speed-camera. It showed that the bubble velocity decreases when increasing the volume fraction.

Dani et al. [7] used a non-intrusive technique consisting of a planar laser-induced fluorescence to measure the oxygen concentration of a bubble as it rises in the liquid. The study showed a distinguished increase in oxygen concentration at the bubble rising column while it is decreasing everywhere else.

Ashley et al. [8] conducted a bench-scale experimental study to examine the effect of four design variables on the oxygen transfer rate in aeration systems that uses fine pore diffuser. The study showed that the oxygen transfer rate is increased when increasing the airflow rate. A comparison between using a single diffuser and two diffusers for the same airflow rate showed that the oxygen transfer efficiency is higher when using two diffusers. The study used two different diffusers to create bubbles of 0.4 and 0.42 mm; there was no consistent effect of airflow rate on the bubble size.

Fujie et al. [9] investigated the spiral liquid circulation in a conventional aeration tank. The spiral liquid circulation rate at the liquid surface in the aeration tank was correlated as functions of the superficial gas feed rate, diffuser depth, and bubble diameter. It was concluded that the spiral liquid circulation rate increases the bubble velocity that increases the gas-liquid oxygen transfer.

Bubble size, bubble release rate and mixing within the tank was investigated by researchers [10-14]. It was found that the smaller bubble size, increased bubble release rate and improved and induced mixing to enhanc the oxygen transfer efficiency.

Recent research conducted by Alkhalidi et al. [15], have proven that pulsating airflow can enhance the oxygen transfer efficiency more than continuous airflow. The improvement is due to the generating waves because of the pulsating effect, which increases the mixing process between the air and water.

Alkhafaji et al. [16], considered the effect of pulsating airflow on the aeration efficiency for a range of airflow rate between 14 and 56 LPM. The study was conducted at different pulsating times. It was concluded that when using 0.5 seconds of pulsating time, the SOTE increased to about 50% more than that of continuous air flow.

The current study also focuses on how to increase the oxygen transfer rate between the air and water, but by augmenting the wavy flow in a water reservoir instead. This augmentation can be induced by using the pulsating air flow instead of the continuous airflow in the water reservoir and investigate the effect of the water column height on the oxygen transfer efficiency.

2. Methodology

The experimental set up for this study can be illustrated as shown in figures 2 and 3. The supplied air flows through a flow meter and a pressure gauge. Before it passes through the diffusers, the air passes through a control circuit, figure 2, this control circuit acts as an on/off switch to create the pulsating effect. Therefore, the air will diffuse alternatively from two air diffusers into the water. These are fine pore diffusers made of rubber, installed at the bottom of the water tank. The control circuit programmable software can control the time the air takes to diffuse into the water. The diffusers are connected with upstream solenoid valves, which are part of the control circuit, when one of the solenoids on, the other one is off and vice versa. This is the method used to create the pulsating or the alternating effect.

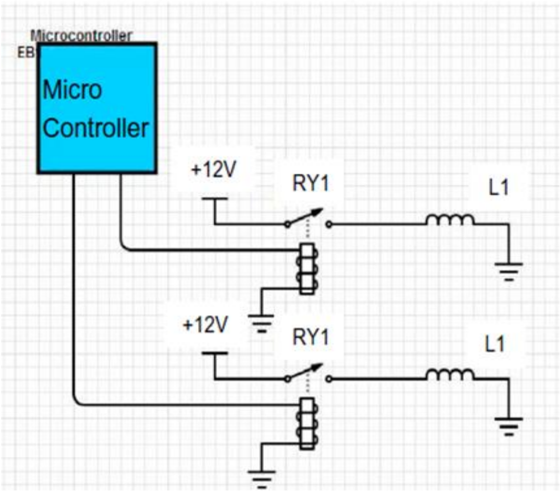

Figure 2: Control circuit [15, 16].

Three dissolved oxygen (DO) probes (see figure 3) were installed at different elevations along the water tank at different heights with an intermediate radial position between the two diffusers. These DO probes are used to measure the dissolved oxygen concentration in the water with 1 Hz frequency. They can measure oxygen concentration up to 20 mg/l within ±2% accuracy.

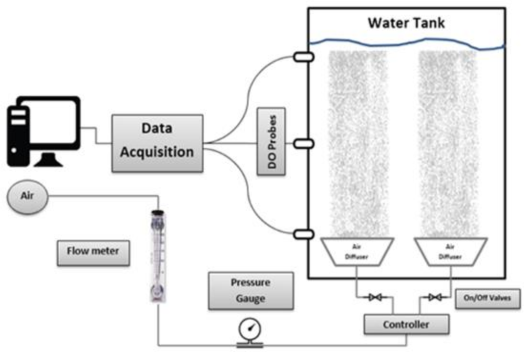

Figure 3: Experimental set up [15].

The oxygen concentration results obtained from these three DO probes were averaged for better accuracy to achieve the oxygen transfer efficiency (OTE). All the measurements are conducted under standard conditions, which include tap water, zero salinity, atmospheric pressure and 20ºC. Therefore, SOTE is the transfer parameter to be obtained in this analysis.

To obtain SOTE, the overall mass transfer coefficient needs to be determined first. This can be done by measuring the dissolved oxygen concentration in the water. In measuring the dissolved oxygen in the water, measurements should start with zero oxygen water; this means that oxygen should be removed from the water. The addition of sodium sulfite (Na_2SO_3) is used here to extract the dissolved oxygen and leaving the water with zero oxygen. Then, the overall heat transfer coefficient can be calculated by:

$$KLa = \ln((C\infty - C)/(C\infty - C0)/t \tag{1}$$

Equation 1 is used to calculate the overall mass transfer coefficient for the conditions when the water temperature is 20ºC. For temperatures less or greater than 20ºC, equation 1 should be corrected according to the following equation [17]:

$$KLa_{20} = KLa\theta^{(20-T)} \tag{2}$$

Where θ = 1.02.

Then, the oxygen transfer rate (OTR), can be obtained by:

$$OTR = KLa\, V(C_\infty - C_0) \tag{3}$$

Finally, The OTE can be calculated by using:

$$OTR = OTR/\dot{m}_{O_2} \tag{4}$$

SOTE is the transfer parameter used for this study, which is the measure of how efficient the aeration system is. Therefore, equation 4 becomes:

$$SOTE = SOTR/\dot{m}_{O_2} \tag{5}$$

3. Results

The SOTE is the transfer parameter that reflects the effectiveness of the aeration process. Therefore, the goal of the current study is to obtain the SOTE results for each water column at different pulsating times. Three pulsating times are considered: 0.5, 1.5 and 2.5 seconds. Increasing water column on top of air membrane includes an increase in water tank volume, larger water tank volume requires higher airflow rate to aerate this water. A ratio parameter between airflow to tank size parameter, called Amano Alkhafaji Alkhalidi (AAA), will be introduced for best data rendering. The AAA, see Eeq. (6), the parameter will be used to compare the SOTE results for different water column heights in the first part of the results discussion (figures 4 to 6). The second part (figures 7 to 9) relates the SOTE with the flow rate at different pulsating times.

$$AAA = 4Q/(\pi D^2 H) \tag{6}$$

Where:

Q= Airflow rate, L/min.

D= Tank diameter, m.

H= Tank high, m

First, the SOTE investigation was carried for each water column at different pulsating times, SOTE results will be compared to different water columns at each pulsating time. Figures 4, 5 and 6, show the SOTE variation with AAA for 0.6, 1.2 and 1.8 m water columns respectively.

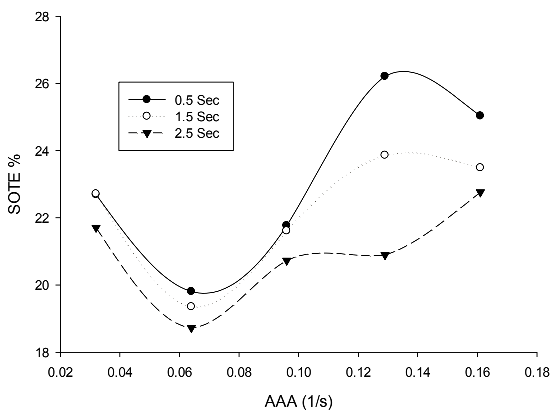

Figure 4: SOTE variation with AAA parameter for 0.6 m water column.

Relatively similar behavior for all pulsating times can be noted from figure 4, where the SOTE decreases as AAA increases from 0.03 to 0.064 1/min. The SOTE keep increasing between 0.064 and 0.13 1/min. Beyond 0.13 1/min, the SOTE decreases again for all the pulsating time cases except the 2.5 seconds pulsating time case, where the SOTE increases.

Figure 5, shows the SOTE variation with AAA when the water column equal to 1.2 m. Figure 5 gives similar behavior to that of Fig. 4, except for the region when AAA ranges between 0.074 and 0.093 1/min. The SOTE is increasing for the 0.5 and 1.5 seconds cases, but it decreases for the 2.5 seconds pulsating time.

The last figure to show in the first part of the results in figure 6, which is the case when the water column is 1.8 m. In this figure, the SOTE follow a similar trend as in figures 4 and 5 between 0.012 and 0.046 1/min, except the case when the pulsating time is 2.5 seconds. Beyond 0.046 1/min, the SOTE is decreasing for all pulsating times.

Figures 7, 8 and 9, show the SOTE variation with flow rate for the three water columns when the pulsating time equals to 0.5, 1.5 and 2.5 seconds, respectively.

Figures 7 and 8 show similar trend, where the SOTE decreases when the flow rate increases from 14 to 28 L/min and then it increases between 28 and 56 L/min. When the flow rate increases from 56 to 70 L/min, the SOTE for both the 0.6 and 1.8 m water column is decreasing while it is increasing for the 1.2 m water column.

When comparing figures 7 through 9, they clearly show similar trends when the flow rate increases from 14 to 42 L/min. After that, the SOTE trend tends to be less steep for the higher water column as the pulsating time increase. However, the case is opposite to the lower water column.

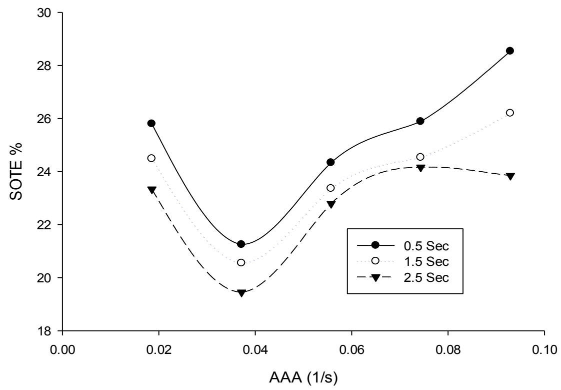

Figure 5: SOTE variation with AAA for 1.2 m water column.

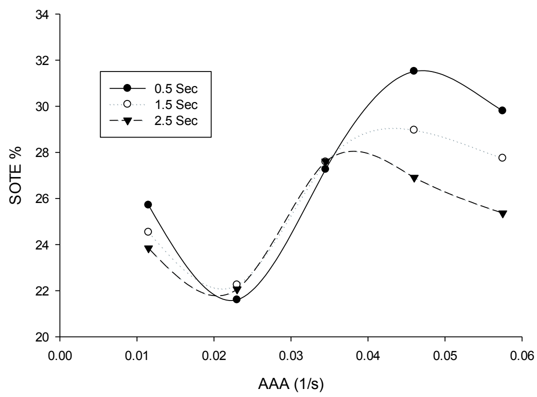

Figure 6: SOTE variation with AAA for 1.8 m water column.

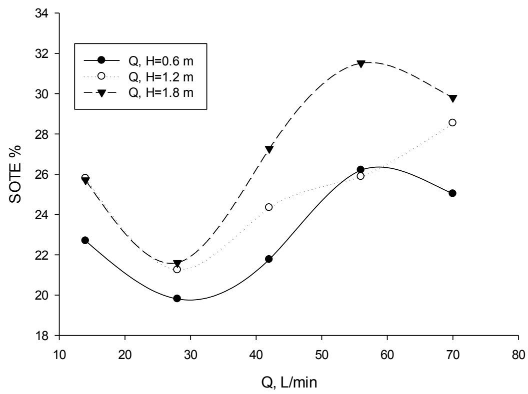

Figure 7 SOTE variation with flow rate for 0.5 seconds pulsating time.

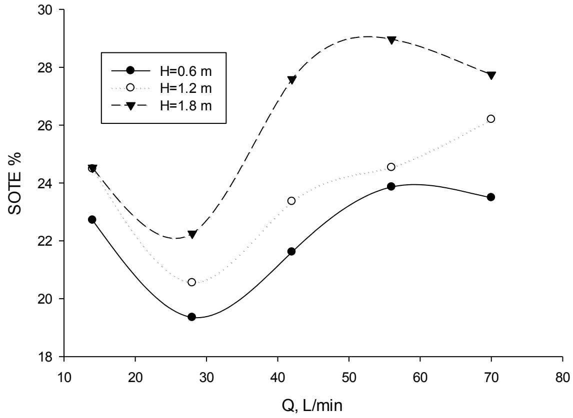

Figure 8: SOTE variation with flow rate for 1.5 seconds pulsating time.

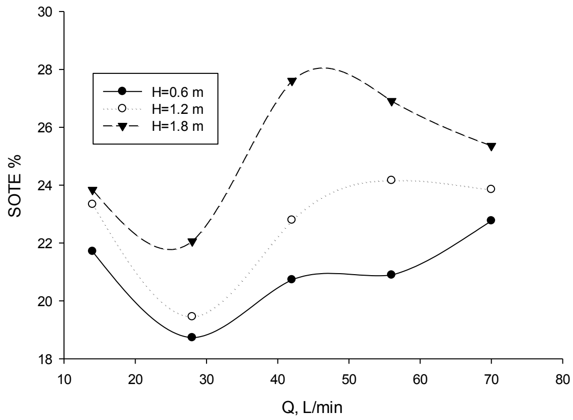

Figure 9: SOTE variation with flow rate for 2.5 seconds pulsating time.

It is noted from the SOTE results that they all start with high SOTE then it decreases. This pattern is because, at a very low flow rate, the SOTE is relatively high since the SOTE is inversely proportional to the oxygen flow rate and hence the air flow rate. Then the SOTE experience an increase when the flow rate increases beyond 28 L/min, which is attributed to the mixing contribution due to the wave generated from increasing the flow rate that helps to increase the mass transfer between the air and the water.

Based on figures 7 through 9, it is noted that the higher SOTE can be considered to occur when using a higher water column (1.8 m). The lowest SOTE is given when using the lowest water column 0.6 m. Nevertheless, it is evident from figures 7, 8 and 9 that, the SOTE trend is increasing for the lowest water column while it is decreasing for the highest water column at higher flow rates and vice versa at lower flow rates. This means that the waves created in the lower water column case (0.6 m) can be considered to have a more significant effect than those produced in the highest water column (1.8 m) at higher flow rates. This behavior is particularly observed when the pulsating time is 2.5 seconds, where all the SOTE results are tending to approach each other. In addition, it is noted that, in the case of the 1.2 m water column, the SOTE always represents a median between that of the higher and the lower water column for all ranges of flow rates and at any pulsating time.

Figures 10 and 11 show the surface waves generated for the 0.6 and 1.2 water columns when the pulsating time is 2.5 seconds. The 0.6 m water column gives the highest surface wave that can be measured approximately 7 cm high. For the 1.2 m water column, the surface wave is a little lower than that of the 0.6 m water column, which is approximately 3 cm. The 1.8 water column showed very low surface waves that can be insignificant.

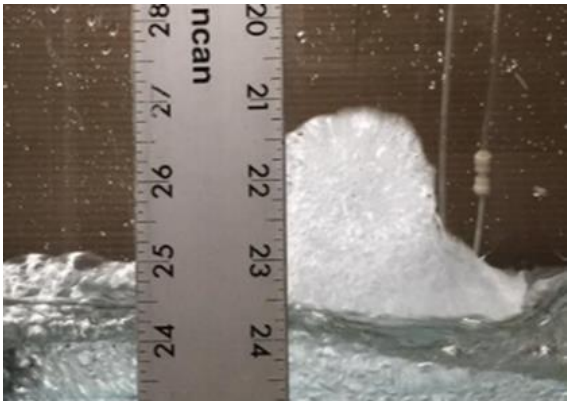

Figure 10: Surface wave generated for the 0.6 m water column

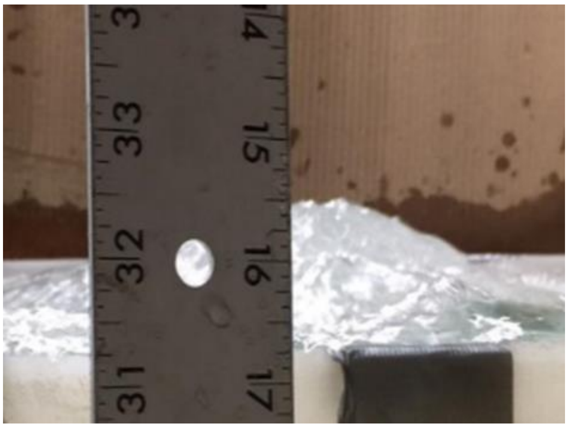

Figure 11: Surface wave generated for the 1.2 m water column

Therefore, the surface wave generation is depending on the height of the water column. It is attributed to the balance between the lift and the drag forces acting on the bubbles [18], which determines the resident time of the bubbles in the water. A study to determine the relation between the resident time and the water column height is suggested since this study is not discussed in the current paper.

SOTE measurements uncertainty analysis was performed for the 1.2 m water column height. The uncertainty of the measurements for that case is ranging between ± 3.9 and ± 0.05 % as shown from Table 1.

Table 1: Measurement uncertainty of SOTE for the 1.2 m water column

		Pulsating time (seconds)		
		0.5	**1.5**	**2.5**
Flow rate (L/min)	**14**	± 0.032	± 0.023	± 0.013
	28	± 0.012	± 0.002	± 0.039
	42	± 0.025	± 0.0005	± 0.015
	56	± 0.015	± 0.035	± 0.038
	70	± 0.023	± 0.021	± 0.033

4. Conclusion

The SOTE results for the 1.8 m water column is the highest among all the water columns. The lowest SOTE results are obtained with the 0.6 m water column. An intermediate behavior is observed when considering the 1.2 m water column. Also, the highest SOTE can be found when the pulsating time is 0.5 seconds; this applies to all the water column cases. The higher SOTE when using, the higher water column can be attributed to the rising velocity of the bubbles, which becomes low compared with the lower water column. In this case, the bubbles will stay longer in the water, and the oxygen transfer process from the bubble to the water will take longer time. Therefore, better oxygen transfer rate is experienced as the water column becomes higher than 0.6m. On the other hand, another important factor that has been observed to affect the results, particularly for the lower water column, that is the effect of the airflow rate. The SOTE results tend to trend better than that of the higher water column at higher flow rates. Therefore, there can be a better potential for improvement when considering lower water column with higher flow rates.

References

[1] M. Davis, "Water and wastewater engineering". McGraw-Hill Science, New York, NY.

[2] "Madison gas and electric company". www.mge.com.

[3] "Wastewater technology fact sheet,". Environmental Protection Agency, Washington, D.C, 1999.

[4] R. Higbie, "The rate of absorption of a pure gas into a still liquid during a short time of exposure". Transactions of the AICHE, Vol. 31 (1935), 365– 389.

[5] A. Das, P. Das, P. Saha, "Formation of bubbles at submerged orifices – experimental investigation and theoretical prediction". Experimental Thermal and Fluid Science, Vol. 35(4) (2011), 612-627.

[6] D. Colombet, D. Legendre, A. Cockx, P. Guiraud, F. Risso, C. Daniel, S. Galinat, "Experimental study of mass transfer in a dense bubble swarm". Chemical Engineering Science, Vol. 66(14) (2011), 3432-3440.

[7] A. Dani, P. Guiraud, A. Cockx, "Local measurement of oxygen transfer around a single bubble by planar laser-induced fluorescence". Chemical Engineering Science, Vol. 62(24) (2007), 7245-7252.

[8] K. Ashley, K. hall, D. Mavinic, "Factors influencing oxygen transfer in fine pore diffused aeration". Water Research, Vol. 25(12) (1991), 1479-1486.

[9] K. Fujie, K. Urano, H. Kubota, T. Kasakura, "Hydrodynamics and oxygen transfer characteristics in activated sludge aeration tanks". Water Science and Technology, Vol. 26(3-4) (1992), 791-800.

[10] A. Alkhalidi, and R. Amano, "Bubble deflector to enhance fine bubble aeration for wastewater treatment in space usage". 50th AIAA Aerospace and Sciences Meeting Including the New Horizons Forum and Meeting Aerospace Exhibition, 999, 2012.

[11] A. Alkhalidi and R. Amano, "Study of air bubble creation for aerospace application". AIAA Paper, 2011-5742.

[12] R. Amano, A. Alkhalidi, B. Miletta and J. Li, "Study of air bubble creation for aerospace applications". 9th Annual International Energy Conversion Engineering Conference, 2011- 5742.

[13] A. Alkhalidi, and R. Amano, "Factors affecting fine bubble creation and bubble size for activated sludge". water and environment journal, Vol. 29(1) (2015), 105-113.

[14] A. Alkhalidi, P. Bryar, and R. Amano, "Improving mixing in water aeration tank using innovative self-powered mixer and power reclamation from aeration tank". JJMIE, Vol. 10(3) (2016).

[15] A. Alkhalidi, H. Alba'aba'a, R. Amano, 2012, "Wave generation in subsurface aeration system: A new approach to enhance mixing in the aeration tank in wastewater treatment". Desalination and Water Treatment, 57(56), 27144-27151, http://dx.doi.org/10.1080/19443994.2016.1172263.

[16] A. Alkhafaji, A. Alkhalidi, and R. Amano, "Study of aeration by using pulsating air flow". AIAA Paper, 2017-1837

[17] ASCE, Front Matter, and Software, 1993, "Measurement of oxygen transfer in clean water". ANSI/ASCE 2-91, pp. i–x, doi: 10.1061/9780872628854.fm

[18] W. Haberman, R. Morton, "An Experimental Study of Bubbles Moving in Liquids". Proc. ASCE, Vol. 80 (1954), 379-427.

JJMIE

Volume 12 Number 1, June. 2018
ISSN 1995-6665
Pages 51 - 58

Jordan Journal of Mechanical and Industrial Engineering

Validation of Jordanian Green Building Based on LEED Standard for Energy Efficiency Methodology

Abdullah A. Alshorman*, Khalideh Al bkoor Alrawashdeh, Malek Alshorman, Nesrin T. Talat

Al-Balqa' Applied University- Al-Huson University College, Mechanical Engineering Department, P.O.Box 50 - Al-Huson 19117- Irbid – Jordan

Received 11 Jan 2017 *Accepted 21 June 2018*

Abstract

In this research, validation of Jordanian green building model (JGBM) based on Leadership in Energy and Environmental Design (LEED) standards was investigated. Different items were studied for energy efficiency analysis. Photovoltaic systems, thermal insulation, shading, appliance, lighting and residential people were the items included in this research study. The field work of JGBM covered about 115 apartments and 73 houses in 4 Jordanian cities (Amman, Irbid, Zarqa, and Aqaba). Based on the technical analysis calculations and model validation, it is suggested that Jordanian green building model can save about 68% of energy needed for cooling, reaching 69 points out of the total 110 points, this JGBM rated the gold class according to the LEED-nominal classification.

Saving energy was investigated in terms of different parameters of a proposed model of the architectural side, which were showed high efficiency of saving energy; 63.11% of polystyrene insulation, 14.12% of PV system, 7.26% of double glazed, 6.89% of LED light, 5.1% of overhangs and 3.46 % light color stone.

Keywords: *Validation, Jordanian green building model, energy saving, LEED, BD+C System*.

1. Introduction

The future of renewable energy supply is an essential concern for many developing countries [1,2], especially in the Middle East. Recently, the need for energy security has increased even more because of the political and economic conditions relating to the energy crisis in the region. Moreover, the environment issue requires considerable efforts by decision makers and researchers to reduce the side effects of fossil fuels [3]. In this context, countries and organizations are presenting various mechanisms across different sectors to improve energy efficiency, one of which is the building and construction sector [4]. Many studies on the building sector reveal an intense consumption of energy resources [5, 6]. In fact, buildings account for 40 % of global energy use [7]. Therefore, due to the fact that buildings are physical structures, the possibility of achieving savings in this sector is enormous [8].

Based on Environmental Protection Agency (EPA), green building is defined as "the practice of creating structures and using processes that are environmentally responsible and resource-efficient throughout a building's life-cycle from siting to design, construction, operation, maintenance, renovation and deconstruction. This practice expands and complements the classical building design concerns of economy, utility, durability, and comfort. Green building is also known as a sustainable or 'high performance' building" [9].

For Jordan, the construction sector is under pressure to meet the increasing demands for energy. Jordan imports about 98% of energy from other countries, in addition to a rapidly growing need for housing and commercial space [10]. Those require many measures that comply together with sustainable energy technologies, which can be achieved by the construction and building management codes. According to UNEP, (2007) building sector consumption accounts for more than 33% of total energy consumption, it is also responsible for the high emission of CO_2. In fact, Jordan suffers from serious challenges and most of which are a scarcity of supply of natural resources and unsteady energy supply, that required encouraging and providing incentives for green building application. The Jordan Green Building Guide (JGBG) was developed in 2009 and was initiated in 2013, and after that it was launched on the 3rd of September 2015 [11], which includes comprehensive technical standards. It focuses on the requirement of energy efficiency, water efficiency, healthy indoor environment and Green Building (GB) management, to create a noticeable shift in construction practices, which lead to saving energy and the cost [12].

GB sector has a wide range implication on other sectors in addition to energy field, such as waste management, economic activities, and potable water. GB leads to an integrated systematic approach which explores ideal

* Corresponding author e-mail: mshorman86@gmail.com.

opportunities for the comfort of human and economic development. Moreover, improving the energy efficiency of building is among the most cost-effective ways of improving climate change, and decrease greenhouse gas rate [13]. Some studies reported that environmental design features should not be more expensive than those of traditional low-income housing [14]. Kats et al (2003) investigated the average cost premium for building, they concluded that can be saved of 20% of the construction energy cost by applying less than 2% of the code [15]. Kibert (2005) reported that to build GB, the building professionals should be qualified with skills and experiences needed, by taking into consideration important issues, such as: ventilation system, isolated system and construction items [16]. Till now, more than 31 GB certification programs and 55 schemes are used in over 30 countries around the world, and some programs LEED are used in most countries [17]

A rating system for Neighborhood Development Rating Systems is created in the United States, it is known as Leadership in Energy and Environmental Design (LEED). It primarily functions to evaluate the sustainable building through building scale assessment in terms of the developed area according to sustainability criteria which included environmental, social, economic, site/land activities, in addition to communication, transportation and the assessment of building forms for housing performance [18]. One of the most categories which required an assessment by IEEE, is the Indoor Air Quality (IAQ). Generally, IAQ is related to pollutants that can affect the human health, the indoor air of the space, and the sources contributing to the indoor air pollution [19].

The Leadership in Energy and Environmental Design (LEED) specifications will be adopted on display of the design and construction characteristics where the more cost-effective measures will be shown, these measures can be considered to qualify for certification under LEED-NC for Retail 2009, so a better experience on the green building can be achieved.

To evaluate the performance of insulation of energy issues, there are two factors used to specify the best products that suit for the building; R-value and U-values. R-value related to resistance issues while a U - value is used to measure the rate of heat transfer. For efficient energy performance, and to reduce the energy consumption, a system with the highest R-efficiency is the best effective performance-based value for the insulation products being installed, especially because the overall energy performance of the building is clearly influenced by the issues associated with the selection and installation of the insulation system. In response to achieving lower energy consumption, the regulations of building that focus on reducing energy and heat transfer through higher insulation levels increase air tightness [20]. One of the most essential materials used as the insulation is the polystyrene, it is widely used for building envelopes, roofs and below-grade foundations. However, the efficiency of polystyrene as an insulator is based on its thickness [22].

This program is concerned with greening the retail sector, so a number of criteria and standards are based on it to ensure that any building has the LEED certified will be in the allowable range on achieving this standard. Operators of the project had selected a certain number of points for each category that LEED is interested in. These categories and points of distributions are summarized in Table 1.

Table 1: LEED for retail 2009 System

Category	Total points	Issues Evaluated by the LEED-NC 2009 System
Sustainable Sites	26	Avoiding sensitive sites; locating to facilitate use of public transportation, reducing site impacts of construction, creating open space; enhancing storm water management; lowering the urban heat island effect; controlling light pollution.
Water Efficiency	11	Encouraging water conservation in landscape irrigation and building fixtures; promoting waste water reuse onsite sewage treatment.
Energy Efficiency	33	Energy conservation; using renewable energy systems; Building commissioning; reduced use of ozone depleting chemicals in HVAC systems; energy monitoring; green power use.
Materials/Resources	13	Use of existing buildings; facilitating construction waste recycling; use of salvaged materials, recycled-content materials, regionally produced materials, agricultural-based materials and certified wood products.
Indoor Environment	16	Improved ventilation and indoor air quality, use of non-toxic finishes and furniture; greenhouse keeping; daylighting and views to the outdoors; thermal comfort; individual control of lighting and HVAC systems.
Innovation in design; Regionally Appropriate Measures.	10	Exemplary performance in exceeding LEED standards; use of innovative approaches to green design and operations; four points for addressing regionally significant issues.

From these classifications which are based on 110 available points to evaluate any building to have a LEED certified, the following table shows the nominal classification based on the number of points the building had achieved.

Table 2: Nominal classification for Green Building from LEED

Number	Classification	Points
1	Certified	40 to 49
2	Silver	50 to 59 points
3	Gold	60 to 79 points
4	Platinum	≥80 points

This research aims to contribute to a better understanding of the concept of green building rating system and its role in achieving sustainable development, and to improve the sustainable practices. In addition, it aims to validate the Jordanian green building based on LEED V4 Standard. Also, to verify cooling and heating load and critical factors to the success of sustainable development.

2. Methodology

To improve the consumed energy and increase renewable energy uses, energy measures were analyzed in four cities in Jordan. The categories performed in this study included: measures of energy efficiency based on available renewable energy in sites using the thermal numerical computerized model that is designed exclusively for this study as comprehensively explained in reference [21].

2.1. Location selection

In fact, Jordan is divided into three zones in the terms of climatic issues, as reported in Jordan Thermal Insulation Code, Appendix (B) [22]. As shown in Figure. 1, Zone- 1 the Rift Valley in the west, zone-2 the highland in the center and the zone-3 desert in the east where the chosen cities in this study within these regions, and these are the most densely populated regions where the average temperature is 8 - 27℃ in Amman, 15 – 45℃ in Aqaba, 7 – 33℃ in Irbid and 9 to 44℃ in Zarqa. Between day and night, the climate varies dramatically, as well as from summer to winter. This variation leads to different approaches for analysis of energy efficiency and insulation factor.

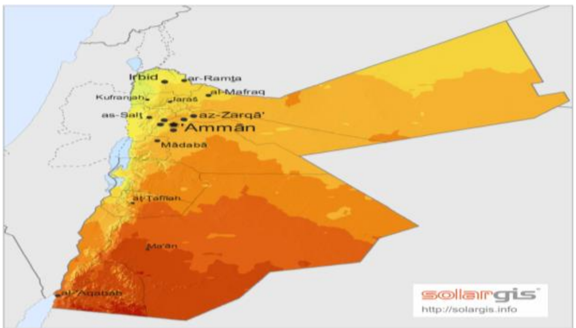

Figure 1: Jordan three climatic regions.

* Corresponding author e-mail: alshormana@asme.org.

Samples

Based on the design characteristics of green buildings that are available in LEED standard, and the results of the Jordanian building characteristics will be combined in the Jordanian green building model with Architectural design and Construction materials. Random samples were taken from apartments and houses in different cities in Jordan, including: Amman, Irbid, Zarqa and Aqaba. One hundred and fifteen apartments with average areas 154 m^2 and 73 houses with average areas 415 m^2.

Different items were used to assess the energy consumption in the building; these factors are Photovoltaic systems, Insulation, Shading, Appliance, Lighting and people. The results in terms of residential flats can be summarized by the following table:

Table 3: Mean area of residential flats:

Location	**Number of samples**	**Average area (m^2)**
Amman	42	170
Zarqa	29	156
Irbid	23	140
Aqaba	21	134
	Total: 115	Average:154

Table 4 shows the same procedure had applied to a sample of houses in various locations in Jordan to find out the average area for it, the results were as follows:

Table 4: Summary of data resources referenced in this study.

Location	Number of samples	Average area (m^2)
Amman	27	455
Zarqa	16	444
Irbid	19	345
Aqaba	11	389
	Total: 73	Average:415

To recognize the effectiveness of the green buildings installation in Jordan, the total saving of the proposed model of green building will be compared with a general house (non-green building) in terms of cooling and heating load requirements using thermal computerized model that is designed exclusively for this study as comprehensively explained in reference 21. This study sample was chosen from various grade construction, the results were analyzed.

Different suggested considerations related to energy consumption and energy saving were studied in an attempt to find both quality and quantities of energy saving methods. Based on the field survey and data collected the proposed model of green building for Jordanian climate succeed in reducing the cooling load requirements by 68% and the heating load requirements by 65%.

On the basis of LEED v4 for Building Design and Construction (BD+C) System (i.e., (B) for Building, (D) for design and (C) for construction); the suggested model of the Jordanian green building had achieved 69 points from the total 110 points, and from the LEED-nominal classification, this Jordanian green building model deserved the gold class.

The focus was on the field of energy, in terms of increasing the energy efficiency and reducing the requirements of heating-ventilating -air-conditioning (HVAC) systems. To improve the Jordanian green building model, several features (several green building standards, certifications, and rating systems were publicized in the last two decades) and should be studied and considered.

Measures for heat gains reduction, including radiant barrier, shading, heat dissipation contributed the highest energy use reduction in cooling dominated locations. The development in the chosen cities (Amman, Irbid, Zarqa, and Aqzba) shows that building measures that resulted in large heating energy savings increased the cooling energy use exceeded the heating energy use. A certain green practice and green products could improve indoor air quality, by focusing on ventilation control and openings control.

3. Results and discussion

3.1. Energy consumption factors of buildings

As mentioned before, there are different items shares to specify the quantity of energy consumption, such as insulation thickness, PV panels with different of installing area, overhang width, different types of windows, lighting, appliances and masonry stone color. To address the heat loss and improve energy efficiency, a model of the components of the architectural side was proposed as shown in Table 5.

Table. 5: Components of the architectural side of the proposed model

Element	Number	Orientation	Area of windows (m^2)
House entrances	2	South, North	-
Guestrooms	1	East, North	1.5 x 1
Bedrooms	1	South, West	2 x 1
Bathrooms	3	East, South, West	0.5 x 0.5
Kitchens	3	South, West	2 x 1

The effect of the thickness of polystyrene on the amount of heat loss is shown in Fig. 2. With the increase of thickness, the amount of heat loss decreases. This agrees with recent studies have demonstrated that polystyrene insulation is the most energy-effective way to reduce significantly heat losses [21, 22, 24].

To evaluate the insulator effect on the heat efficiency, and to address the heat loss, an innovative polystyrene is used as a potential solution. Using polystyrene is important to increase the thermal performance in the building sector, in addition, to reduce the impact of urban noise. In this study, was highlighted on the effect of the thickness of polystyrene on the energy efficiency, the result was agreed with [25, 26]. Yu et al, (2009) was concluded that the optimum insulation thicknesses conjunction with higher saving energy, it varied in a wide range, and expanded polystyrene was the most effective insulation [26]. Referring to Fig.2 it is clear that the optimal insulation thickness range was (5-10) cm (i.e., 7-cm) to have functional heat saving and minimum heat losses through building walls.

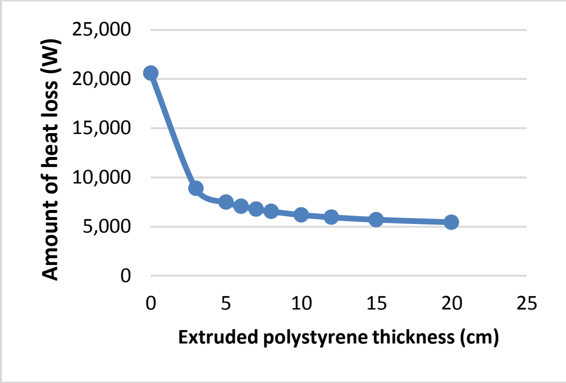

Figure.2: performance of polystyrene versus heat loss .

Also, as the increase insulation thickness, the energy performance increase as shown in Table 6, Installing more insulation in the building increases the R-value and the resistance to heat flow.

Table. 6: The effect of insulation thickness VS heat gain and energy saving

Insulation thickness (cm)	Heat Gain (KW)	Energy Saving (%)
0	25.5458	0 .0
1	14.2959	39.5971 %
2	10.3489	53.5190 %
3	8.3355	60.6268 %
4	7.1142	64.9401 %
5	6.2945	67.8362 %
6	5.7061	69.9151 %
7	5.2633	71.4800 %
8	4.9180	72.7004 %
9	4.6412	73.6789 %
10	4.4143	74.4809 %
11	4.2250	75.1502 %
12	4.0646	75.7172 %
13	3.9270	76.2037 %
14	3.8077	76.6258 %
15	3.7031	76.9953 %
16	3.6108	77.3217 %
17	3.5288	77.6119 %
18	3.4553	77.8717 %
19	3.3891	78.1057 %
20	3.3292	78.3175 %
21	3.2748	78.5101 %
22	3.2250	78.6860 %
23	3.1794	78.8473 %
24	3.1374	78.9957 %
25	3.0987	79.1328 %
26	3.0628	79.2598 %
27	3.0294	79.3777 %
28	2.9984	79.4875 %
29	2.9694	79.5900 %
30	2.9423	79.6859 %

Table 7 presents the electrical power production can be produced through PV system that based on the PV installing area. The energy consumption in the building was assessed according to different items: insulation thickness, PV panels with different of installing area, overhang width, overhang width, different types of windows Energy consumption was investigated with installing a PV system, which cover a part of required energy of the building. The results were consistent with Hwang et al. [27]. That they reported the PV systems can cover in the range of 1- 5% of electrical energy consumption of the office building.

Table. 7: The effect of area of insulation on the monthly acquired power from PV

Percentage-of ceiling area (%)	PV installing area (m^2)	Output power (kWh)
10 %	15.5	172.2
20 %	31.0	344.4
30 %	46.5	516.6
40 %	62.0	688.8
50%	77.5	861.1
60 %	93.0	1033.3
70 %	108.5	1205.5
80 %	124.0	1377.7
90 %	139.5	1549.9

A range of exposed overhang width was investigated to evaluate energy saving. As reported in Table 8, the heat gain decreasing with overhang width increasing. Actually, overhang width is an effective factor on energy performance and can be considered it as a passive cooling option on the building [21, 29]. Table 9, shows the effect of window width on the energy efficiency of buildings.

Table. 8: Heat gain and energy saving vs. Overhang width.

Overhang width (cm)	Solar Heat gain (KW)	Saving (%)
20	6.8269	0.0 %
32	6.4173	6.0 %
44	5.8029	15.0 %
56	5.2567	23.0 %
68	4.7788	30.0 %
80	4.3692	36.0 %
92	4.0279	41.0 %
104	3.6865	46.0 %
116	3.4135	49.0 %
128	3.1745	53.5 %
140	2.9697	56.5 %

Recently, triple glazing is increasingly being presented as the best solution for energy saving, and as the results shown in Table 9, it was better than doubled glazing. Switching to triple requires higher cost and material production has an impact on the environment. The optimum insulation material for filling gaps between the glass is the Krypton in both cases of double and triple glazing. The quantity of producing electrical power from photovoltaic (PV), for each sample, was based on the installed area, inclination and direction of the PV panels. As shown in Table 10, the quantity of saving energy is 14.2%, considering the seasons, Longitude and latitude of all sites for samples the percentage of saving energy it

is agreed with A. Alshorman and M. Alshorman (2017)[21]. Also, Using LED light system achieved

about 6.9, which is characterized with long cycle life respect to traditional type, in addition to it is considered as Eco-friendly

Table. 9: windows type and insulation material for filling gaps impact on energy saving..

Number	Windows type	U-value	Saving (%)
1	Single glazing	5.6000	0.0
2	Double glazing (Air)	2.3280	58.4286 %
3	Double glazing (Argon)	1.8170	67.5536 %
4	Double glazing (Krypton)	1.2490	77.6964 %
5	Triple glazing (Air)	1.4760	73.6429 %
6	Triple glazing (Argon)	1.0790	80.7321 %
7	Triple glazing (Krypton)	0.6810	87.8393 %

Table. 10: Proportion of each parameter saving.

No.	Parameter of energy saving	Proportion of saving (%)
1	Extruded Polystyrene insulation	63.11 %
2	Solar Photovoltaic panels	14.12 %
3	Double glazed windows	7.26 %
4	LED light bulbs	6.89 %
5	Windows Overhangs	5.15 %
6	Light color stone	3.46 %

One of the most important files that need to be discussed is the water efficiency, where the water resources of Jordan are very scarce. In addition, the water efficiency field is an important category in the green building considerations. Different ways can improve water efficiency such as greywater installation and reuse treated water in irrigation in gardens or flushes in bathrooms. Also, the innovation side needs more search and development to achieve more feasibility and ability to meet the various residential needs.

3.2. Scaling of Jordanian Green Building Model according to LEED Standard

According to the technical details of LEED-NC for retail 2009 [29], it is possible to introduce the main architectural features of the Jordanian green building model. This side of model can be described as detailed in Table 11 below according the structural design Methodology.

To avoid solar gain in the summer which requires increasing the cooling load and increasing heating load in winter, the openings require improved glass surfaces and shading matter. Considering passive and active heating, to reduce energy load all single pane windows should be replaced with double pane $2 \times 1.1\ m^2$ (U $2.kW/m^2$, air space 12mm), also, requires Venetian blinds and overhangs along it.

Table 11: Main Architectural parameters of buildings according to green building considerations

Category	Result
Outside door	Off-white
Outside construction	Stone
Presence of garden house	Found
Windows area	$(2.0x1.1)\ m^2$
Number of bedrooms	Three
Number of guest house	One
Number of living rooms	One
Number of bathroom	Three
Number of kitchen	One
Average area of apartments	$154\ m^2$
Average area of houses	$415m^2$

One of the major architectural is orientation; as known of the sun path diagram that the southern facing side receives the most amount of solar radiations. For Jordan the wind direction is northwest, based on these facts and to achieve maximum energy saving the following considerations were taken:

Table 12: The achieved considerations in terms of best orientation.

Category	Considerations
Living room windows facing side	In the proposed model, living room windows are oriented to south, so those large amounts of solar radiation and good passive lighting have been achieved.
Kitchen windows facing side	The kitchen windows should not be in the face of the prevailing wind direction because gases and odors that release of kitchen will spread to other spaces in the house, and this is achieved in the proposed model, where kitchen windows are oriented to south and east.
Bedrooms windows facing side	It is preferable with bedrooms windows to be oriented toward western or southern side.
House entrance orientation	Where the main entrance of the house is preferred to orient toward the public street, and this is applied in the suggested model where the street is proposed to locate in the northern facing side.

Different types of construction material were used in Jordan for walls and ceiling structure. The common building construction in Jordan will be adopted for this model, but one layer will be added which is: polystyrene insulation with 5 cm thickness (which is available in Jordanian market). The main characteristics of the proposed model are summarized in the Table 13.

Table 13: The main suggested considerations of the proposed Jordanian green building model (JGBM)

Category	The suggested considerations
Construction insulation	Using Extruded Polystyrene as an inside insulation material of walls and ceiling.
Glass insulation	A double glazing glass with 100% air filled is used.
Energy efficiency	Solar Photovoltaic panels are used as a renewable source of energy.
Lighting	-Natural lighting is successfully achieved by orientation the living room and kitchen to the south.
	-GE energy smart LED is used as energy saving lamps.
Shading	Windows overhangs to be installed in terms of reducing the solar heat gain through the windows glazing. These overhangs can oppose the summer solar noon radiations.
Stone color	The preferred color of the stone is the white degrees (which is given with low absorbance values).

Based on the analysis and data collection from field work different items for energy efficiency were studied, validation of the Jordanian green building model against to the LEED v4 green buildings criteria can be summarized in Table 14.

Table 14: Evaluation of the JGB on the basis of LEEDv4 for BD+C System.

Category	The stated Points from	The achieved points for the
	LEED – NC	JGB model
Location and Transportation	16	13
sustainable Sites	10	6
Water efficiency	11	1
Energy and Atmosphere	33	24
Materials and Resources	13	9
Indoor Environmental Quality	16	13
Innovation	6	0
Regional Priority	4	2
Total	110 points	69 points

To recognize the effectiveness of the green buildings installation in Jordan, the total saving of the proposed model of green building was compared with a general house (non-green building) in terms of cooling and heating loads requirements. This study sample was chosen from various grade construction, the results were analyzed.

Different suggested considerations related to energy consumption and energy saving were studied in aim to find the both quality and quantities of energy saving methods. Based on the field survey and data collected the proposed model of green building for Jordanian climate succeed in reducing the cooling load requirements with the proportion of 68% and the heating load requirements with the proportion of 65%.

The Evaluation of the JGB on the basis of LEEDv4 for BD+C System; the suggested model of the Jordanian green building had achieved 69 points from the total 110 points, and from the LEED-nominal classification, this Jordanian green building model deserved the gold class. Where the number of earned points according to LEED certification refers that it achieved a gold class (60-79 point) to be consistent in Table 1.

The Focus was on the field of energy, in terms of increase the energy efficiency and reduces the requirements of HVAC systems. But in order to improve the Jordanian green building model several files should be studied and taken into account.

4. Conclusion

Jordan has their own established GB assessment systems to assess for sustainability which are driven from LEED assessment. However, every aspect of the sustainability factors must be assessed to ensure a more conservation of the energy and health issues. The assessment tools of LEED are used as guidelines during the evaluation process of proposed Jordanian Green Building Model (JGBM).

The collected data through field survey in four Jordanian cities, in addition to the results of JGBM thermal investigations showed that Jordanian climate plays a role in reducing the cooling load requirements with the proportion of 68% and the heating load requirements with the proportion of 65%. The suggested model of the Jordanian green building had achieved 69 points from the total 110 points, and from the LEED-nominal classification, this Jordanian green building model deserved the gold class.

Proposed model of the components of the architectural side was investigated to address the energy consumption. The percentage of saving energy through proposed parameters are: 63.11% of polystyrene insulation, 14.12% of PV system, 7.26% of double glazed, 6.89% of LD light, 5.1% of overhangs and 3.46% light color stone.

References

[1] Chan, E.H.W. and Lee, G.K.L., A sustainability evaluation of government-led urban renewal projects. Journal of Facilities, Emerald Group Publishing Limited, 26(13/14), 2008, 526-541.

[2] Berke, P. R. and Conroy, M. M., Are We Planning for Sustainable Development. Journal of the American Planning Association, 66(1), 2000, 21-33.

[3] EPA, US Environmental Protection Agency Definition of Green Building, 2016. Available: https://archive.epa.gov/greenbuilding/web/html/about.html.

[4] A Sustainable Housing Forum Report (2003). Building Sustainability: How to Plan and Construct New Housing for the 21st Century, October 2003. Publication by WWF-UK and Town & Country Planning Association (TCPA). Available at: http://www.wwf.org.uk/filelibrary/pdf/buildingsustainably.pdf [January 2010].

[5] WCED, World Commission on Environment and Development. Our Common Future, (Chapter 2): Towards Sustainable Development. 1987, Available: http://www.un-documents.net/ocf-02.htm.

[6] Tosics, I., European urban development: Sustainability and the role of housing. Journal of Housing and the Built Environment, 19, 2004, 67-90.

[7] WBCSD 2009. Energy Efficiency in Buildings. World Business Council for Sustainable Development.http://www.wbcsd.org/DocRoot/Ge2Laeua8uu2rkodeu7q/91719_EEBReport_WEB .pdf. Accessed 17 July 2011.

[8] UNEP, (2011b). Buildings: investing in energy and resource efficiency. In: "Towards a green economy: pathways to sustainable development and poverty reduction". United Nations Environment Program (UNEP), (http://www.unep.org/greeneconomy/Portals/88/documents/ger/GER_9_Buildings.pdf. Retrieved on 28th Dec. 2013).

[10] UN-Habitat, (2008). "Urban Indicators". United Nations (UN). (http://www.unhabitat.org/stats/Default.aspx. Retrieved on 10th Dec. 2010.

[9] EPA "Sustainable Design and Green Building Toolkit for Local Governments" EPA 904B10001, June 2013.

[13] Enkvist, P.A., Naucler, T., and Rosander, J., "A cost curve for greenhouse gas reduction". The McKinssey Quarterly, 2007,1: 35-45.

[14] CSBE, (2010). "Affordable Housing for the Future Competition: A Call for Innovative Ideas for the Design of a Model Water- and Energy- Efficient Low-Income Apartment Building in Abu Alanda, Jordan". (http://www.csbe.org/competitions/abu-alanda_apartments/competition_entries_two_rounds.html. Retrieved on 28th, Dec. 2013).

[11] d'évaluation des mesures - Energy Efficiency Policies and Jordan Energy Building Code (JEBC), 2015 - https://wec-policies.enerdata.net/Documents/cases-studies/CountryCaseStudies-EBC-Jordan.pdf.

[12] JNBC, Thermal Insulation Code, Jordanian National Building Council, 2nd edition, Amman, Jordan, 2009.

[14] CSBE, (2010). "Affordable Housing for the Future Competition: A Call for Innovative Ideas for the Design of a Model Water- and Energy- Efficient Low-Income Apartment Building in Abu Alanda, Jordan". (http://www.csbe.org/competitions/abu-alanda_apartments/competition_entries_two_rounds.html. Retrieved on 28th, Dec. 2013).

[15] Kats, G., The Costs and Financial Benefits of Green Buildings: A Report to California's Sustainable Building Task Force. California, USA, 2003, .

[16] Kibert, C. J. (2005). Sustainable construction: Green building design and delivery. New York: John Wiley & Sons, Inc. LEED (n.d.). Leadership in Energy and Environmental Design for Neighborhood Development Rating System, US Green Building Council. Available at: http://www.usgbc.org/ShowFile.aspx?DocumentID=5275 [15 May 2009]

[17] Wei, W., Ramalho, O., Mandin, C., Indoor air quality requirements in green building certifications, Build. Environ. 92 10e19, 2015

[18] Soo Cheen, S.K. and Abu Bakar, A.H., Incorporating sustainable management system into housing development practice in Malaysia', Int. J. Sustainable Development, 15(3), 2012, 277–291.

[19] P.M. Bluyssen, P. M., Towards an integrative approach of improving indoor air quality, Build. Environ. 44 1980e1989, 2009.

[20] IEA. Technology roadmap - energy efficient building envelopes. International Energy Agency; 2013.

[21] Alshorman, A and Alshorman, M., Green Buildings Analysisfor Energy Efficiency Enhancement– Jordanian Concept. International Journal of Emerging Trends in Engineering and Development, 2017, Issue 6 (7).

[22] Cai.. S., Zhang.. B., Cremaschi.. L., Review of moisture behavior and thermal performance of polystyrene insulation in building applications. Building and Environment Volume, 123, 2017, 50-65.

[23] S. Zawaydeh, Implementing Codes and Regulations as a Driver to Low Energy Buildings – Case Study. Sustainable Vital Technologies in Engineering & Informatics, 8-10 Nov 2016.

[24] Comakli, K., Yuksel, B., Optimum insulation thickness of external walls for energy saving. Appl. Therm. Eng, 23, 2003, 473–479.

[25] Kaynakli, O. A., Study on residential heating energy requirement and optimum insulation thickness. Renew. Energy, 2008, 33, 1164–1172.

[26] Yu, J., Yang., Tian, L., Liao, D., A study on optimum insulation thicknesses of external walls in hot summer and cold winter zone of China. Appl. Energy, 86, 2009, 2520–2529.

[27] Hwang, T., Kang, S., & Kim, J. T., Optimization of the building integrated photovoltaic system in office buildings – Focus on the orientation, inclined angle and installed area. Energy and Buildings, 46, 2012, 92–104.

[28] Raeissi. S., Taheri. M., Optimum overhang dimensions for energy saving. Building and Environment, 33 (5), 1998, 293-302.

[29] LEED 2009 for Retail. (2011): New Construction and Major Renovations Rating System USGBC Member Approved March 2010 (Updated November 2011), Docs7956.pdf.

JJMIE

Volume 12 Number 1, June. 2018
ISSN 1995-6665
Pages 59 - 67

Jordan Journal of Mechanical and Industrial Engineering

A Comprehensive Model of Reliability, Availability, and Maintainability (RAM) for Industrial Systems Evaluations

Mohamed F. Aly[a], Islam H. Afefy[a], Ragab K. Abdel-Magied[b], Eman K. Abd Elhalim[c*]

[a] Industrial Engineering Department, Faculty of Engineering, Fayoum University, Egypt.
[b] Mechanical Engineering Department, Faculty of Engineering, Beni-Suef University, Egypt.
[c] Industrial Engineering Department, Faculty of Engineering, Misr University for Science and Technology (MUST), Egypt.

Received 29 April 2018 Accepted 21 June 2018

Abstract

Reliability, availability, and maintainability are considered as a crucial metrics that are used to evaluate the performance of the industrial systems. In this work, an integrated reliability, availability, and maintainability (RAM) model of the 3-out-of-4 system was proposed to quantify the values of RAM indices and to identify the most critical equipment which mainly affects the system performance. The Markovian approach was adopted to model the system behavior. A transition diagram for the proposed model was constructed and differential equations of the proposed model were formulated to obtain the state probability. The availability at steady state, reliability at transient state and maintainability were analyzed and investigated. The proposed model was verified and validated. A real data of industrial system in Oil and Gas Egyptian Company was applied to validate the proposed model and the effect of failure and repair rates at different mission time was presented and discussed. The results of the applied proposed system revealed that the system availability at steady state is 99 %, the system reliability is 0.59%, and the system maintainability is 0.99%. On the other hand Turbine no. three was found the most critical item in the system and need more attention to improve the system performance. It could be said that the proposed model is considered an excellent tool for industrial systems performance evaluations.

Keywords: *Reliability; Availability; Maintainability; Markov approach*.

1. Introduction

RAM is an important performance metrics in system analysis and considered a good starting point for system improvements [1]. The Oil and Gas industry has consistently increased its requirements, combined with the rise in technological systems, and increased competitiveness of service providers to implement adequate management strategies for these systems to improve their availability and productivity to comply with those most demanding standards. One important point in this regard is to have knowledge about the RAM of the main equipment in this industry [2]. Evidentially, a fault-based (Breakdown) maintenance system in the Oil and Gas industry is a costly and time-consuming process, resulting in a substantial and intangible loss to system operators.

Corvaro, et al. [3], assesses operational performance of reciprocating compressors used in Gas and Oil industry using RAM model. The study aimed to evaluate the effect of different factors related to RAM and devoted to collaborating with the private sector aiming continuous quality improvement. Aoudia, et al. [4], studied the economic impact of maintenance management ineffectiveness of one of the main industrial plants of a major Oil and Gas group. Sharma and Kumar, [5] built a RAM model applied to a process industry using the Markovian approach in steady state. Parametric computations and indices of RAM to assess system performance in repairable industrial systems using Genetic Algorithm (GA) and the Markovian approach were presented [6, 7].

Evidently, the integration of reliability, availability and maintainability of investigation tends to good results. However, reliability, Availability, and maintainability were investigated individually or two of them in the other industries. Much effort has been made by the researchers providing performance modelling and availability analysis applied on different industrial systems as Paper Plant, Paint, and thermal power plant Industry [8-10].

Aggarwal, et. al. [11] presented a model using Markov birth-death process, the concept of fuzzy reliability and availability. A numerical method with the assumption that the failure and repair rates of each subsystem follow the exponential distribution has been developed. In which a mathematical modeling of the system is carried out using the mnemonic rule to derive Chapman–Kolmogorov differential equations and solved it by Runge-Kutta fourth-order method Which is considered one of the most common methods that are used in solving the differential equations as well as it is considered one of the oldest and the best method in numerical analysis moreover; it

* Corresponding author e-mail: emankhtab2005@gmail.com.

provides a popular way to solve the differential equations. When the system includes a large numbers of differential equations, MATLAB program could be used to solve these large equations. For this, the MATLAB software is considered one of the multi programs that could be used for numerical computations.

Lin, et al. [12] presented a reliability study using both classical and Bayesian semi-parametric frame-works, they illustrated how a wheel- set's degradation data can be modeled and analyzed to ease the calculation of system reliability during applying preventive maintenance. Singh, and Goyal, [13] developed methodology to study the transient behaviour of repairable mechanical biscuit shaping system on a biscuit manufacturing plant for determining the availability of the system based on Markov modelling. The differential equations have been solved using Laplace Transforms. Laplace Transform commonly used in the transient state to obtain the state probabilities, in which the differential equations are converted to algebraic equations to simplify the system solution.

The K-out-of-N system is the most important type for the repairable system according to reliability theory and, it is used in many applications such as petroleum industry. An investigation of a 2-out-of-3 system has been presented recently in published work in which the reliability and availability have been evaluated and analyzed for the system using Kolmogorov's equations and applied on some particular cases. In this analysis, mean time to system failure (MTSF), steady-state availability, busy period and profit function were derived to evaluate the system reliability and availability [14-15]. Preeti, [16] presented an analysis which considered as a powerful tool to analyze reliability of a linear consecutive 2-out-of-3-F system with common cause shock failure in which the transient equations of the reliability and steady equations of the availability have been investigated. Yusuf, [17] evaluate the system reliability indices of a repairable 3-out-of-4 system with preventive maintenance involving four types of failures using Kolmogorov equations.

Apparently, the literature review -up to our reading- revealed the following points:

- The researchers concentrated, to more extent, on the investigation of availability and reliability of the industrial systems.
- Oil and Gas industry need more attention to improve and maintain its system performance.
- A little attention is paid to investigate the integration of RAM for different industrial application.
- No more work on studying of RAM analysis for a multi-component system such as 3-out-of-4 system.

Moreover, the applications of RAM analysis as an adopted approach for maintenance policies for Oil and Gas Industrial systems could be proposed and applied for increasing customer satisfaction, reduce the frequency of failures and maintenance costs. This is a motivation of the present work.

The aim of this work is to develop a comprehensive RAM model for industrial systems evaluation. This study has two main parts, as presented in Fig.1; the first is to develop 3-out-of-4 system RAM model based on the Markovian approach. Availability at steady state, reliability at transient state and maintainability are analyzed and investigated. The differential equations are solved using Rung-Kutta method with aided of MATLAB software to get the system availability at steady state (A_{ss}) and solved by Laplace transform to get reliability at transient state. The second is to apply the proposed model for the performance measure of a real case of Oil and Gas industrial system. This model provides results for a complete reliability, availability, and maintainability (RAM) analysis utilizing data sets from a production system in an Oil and Gas plant. A parametric investigation of various values of system failure rates and repair rates on system reliability (R_s), availability, and maintainability and their effects on the system performance are presented. The results of that analysis help the designers/engineers and managers to quantify and measure the system performance; conversely, suitable maintenance policies/strategies can be selected to enhance the productivity of the plant.

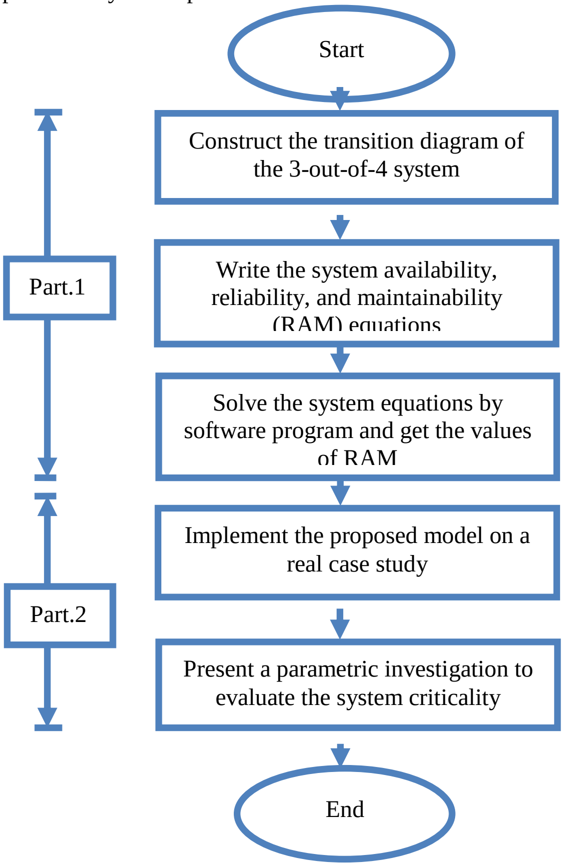

Figuer1: Steps of the presented work.

2. System Description

In this section, the 3-out-of-4 system is described. The system consists of four units in which one unite is standby (sb) and the other three units must be in the operating state (o) for the system to work. The system failed (F) when two units failed and the other two units are in good state (g). Based on Markov assumption [18], differential equations that describe the proposed system are written to analyze the probability for each state. These equations are further solved for determining the RAM indices. The states of the system according to Markov are shown below in Table (1), and the transition diagram in Fig.2 depicts a model showing all the possible states of the system.

Table 1: System states

State	Component state		System condition
	Available and standby	Failed	
S_0	T_1, T_2, T_3, T_4	-	Working
S_1	T_2, T_3,T_4	T_1	Working
S_2	T_1, T_3, T_4	T_2	Working
S_3	T_1, T_2, T_4	T_3	Working
S_4	T_3, T_4	T_1, T_2	Failed
S_5	T_2, T_4	T_1, T_3	Failed
S_6	T_2, T_3	T_1, T_4	Failed
S_7	T_1, T_4	T_2, T_3	Failed
S_8	T_1, T_3	T_2, T_4	Failed
S_9	T_1, T_2	T_3, T_4	Failed

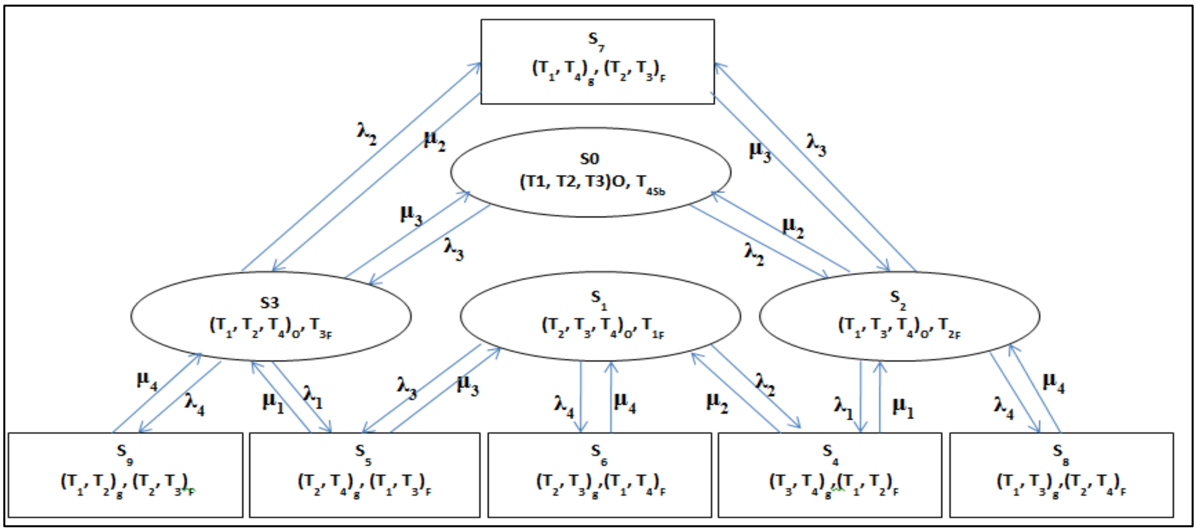

Figure 2: State transition diagram.

Where: : Unit working at full capacity : Failed state

3. Model Proposed

The differential equations associated with the transition diagram are derived on the basis of Markov birth-death process. Various probability considerations generate the following sets of differential equations:

$[(d/dt) + \lambda_1+ \lambda_2 +\lambda_3]\ P_0(t) = \mu_1 P_1(t) + \mu_2 P_2(t) + \mu_3 P_3(t)$ (1)

$[(d/dt) + \mu_1 +\lambda_2 + \lambda_3 + \lambda_4]\ P_1(t) = \mu_2\ P_4(t) + \mu_3\ P_5(t) + \mu_4\ P_6(t) + \lambda_1\ P_0(t)$ (2)

$[(d/dt) + \lambda_1 + \lambda_3 + \lambda_4 + \mu_2]\ P_2(t) = \mu_1\ P_4(t) + \mu_3\ P_7(t) + \mu_4\ P_8(t) + \lambda_2\ P_0(t)$ (3)

$[(d/dt) + \lambda_1+ \lambda_2 + \lambda_4 + \mu_3]\ P_3(t) = \mu_1\ P_5(t) + \mu_2\ P_7(t) + \mu_4\ P_9(t) + \lambda_3\ P_0(t)$. (4)

$[(d/dt) + \mu_1 + \mu_2]\ P_4(t) = \lambda_1 P_2(t) +\lambda_2\ P_1(t)$ (5)

$[(d/dt) + \mu_1 + \mu_3]\ P_5(t) = \lambda_1\ p_3(t) + \lambda_3\ P_1(t)$ (6)

$[(d/dt) + \mu_4]\ P_6(t) = \lambda_4\ P_1(t)$ (7)

$[(d/dt) + \mu_2 +\mu_3]\ P_7(t) = \lambda_2\ P_3(t) + \lambda_3\ P_2(t)$ (8)

$[(d/dt) + \mu_4]\ p_8(t) = \lambda_4 P_2(t)$ (9)

$[(d/dt) + \mu_4]\ P_9(t) = \lambda_4\ P_3(t)$ (10)

Where, the initial conditions at time t = 0 are:

$$p_i(t) = \begin{cases} 1, & \text{ifi} = 0 \\ 0, & \text{ifi} \neq 0 \end{cases} \quad (11)$$

Where:

d /dt: derivative with respect to t.,P0 (t): probability that the system is working at full capacity at time t, Pi (t): state probability that the system is in the ith state at time t, λi: failure rate for unit i, μi: repair rate for unit i.

3.1. Availability Equations

To get the steady state availability of the system (A_{SS}), (i.e., time independent performance behavior) which is mean d/dt =0 and t → ∞, the above equations (eq. 1 to 10) become:

$(\lambda_1 + \lambda_2 + \lambda_3)\ P_0 = \mu_1 P_1 + \mu_2 P_2 + \mu_3 P_3$ (12)

$(\mu_1 + \lambda_2 + \lambda_3 + \lambda_4)\ P_1 = \mu_2\ P_4 + \mu_3\ P_5 + \mu_4\ P_6 + \lambda_1\ P_0$ (13)

$(\lambda_1 + \lambda_3 + \lambda_4 + \mu_2)\ P_2 = \mu_1\ P_4 + \mu_3\ P_7 + \mu_4\ P_8 + \lambda_2\ P_0$ (14)

$(\lambda_1 + \lambda_2 + \lambda_4 + \mu_3)\ P_3 = \mu_1\ P_5 + \mu_2\ P_7 + \mu_4\ P_9 + \lambda_3\ P_0$ (15)

$(\mu_1 + \mu_2)\ P_4 = \lambda_1\ P_2 + \lambda_2\ P_1$ (16)

$(\mu_1 + \mu_3)\ P_5 = \lambda_1\ p_3 + \lambda_3\ P_1$ (17)

$(\mu_4)\ P_6 = \lambda_4\ P_1$ (18)

$(\mu_2 + \mu_3)\ P_7 = \lambda_2\ P_3 + \lambda_3\ P_2$ (19)

$(\mu_4)\ p_8\ (t) = \lambda_4\ P_2$ (20)

$(\mu_4)\ P_9 = \lambda_4\ P_3$ (21)

These equations were solved using Rung-Kutta Forth order method and MATLAB, the values of steady state probabilities are as follows:

$P_1 = (\lambda_1/\mu_1) P_0$, $P_2 = (\lambda_2 / \mu_2) P_0$, $P_3 = (\lambda_3 / \mu_3) P_{0m}$,

$P_4 = (\lambda_1\lambda_2) / (\mu_1\mu_2) P_0$, $P_5 = (\lambda_1\lambda_3) / (\mu_1\mu_3) P_0$,

$P_6 = (\lambda_1\lambda_4) / (\mu_1\mu_4) P_0$, $P_7 = (\lambda_2\lambda_3) / (\mu_2\mu_3) P_0$,

$P_8 = (\lambda_2\lambda_4) / (\mu_2\mu_4) P_0$, $P_9 = (\lambda_3 \lambda_4) / (\mu_3 \mu_4) P_0$

The probability of full working capacity (P_0) is determined using normalizing conditions (i.e.,$\sum_{i=0}^{9} P_i = 1$) as follows:

$$P_0 = [(\mu_1 \mu_2 \mu_3 \mu_4) / (\lambda_1 \mu_2 \mu_3 \mu_4 + \lambda_2\mu_1\mu_3 \mu_4 + \lambda_3 \mu_1 \mu_2 \mu_4 + \lambda_1\lambda_2 \mu_3 \mu_4 + \lambda_1\lambda_3 \mu_2 \mu_4 + \lambda_1\lambda_4 \mu_2 \mu_3 + \lambda_2\lambda_3 \mu_1 \mu_4 + \lambda_2\lambda_4 \mu_1 \mu_3 + \lambda_3\lambda_4 \mu_1 \mu_2)] \quad (22)$$

Having the values of probabilities (P_0-P_9) determined, A_{SS} is calculated as a summation of all working state probabilities as follows:

$$A_{SS} = P_0 + P_1 + P_2 + P_3 \quad (23)$$

3.2. Reliability Equations.

To get the reliability (R_S) of the system under consideration at any time, the equations (1 to10) are solved taking Laplace transform and the probability transform are as follows:

$$[S + \lambda_1 + \lambda_2 + \lambda_3] P_0(S) = \mu_1P_1(S) + \mu_2P_2(S) + \mu_3P_3(S) \quad (24)$$

$$[S + \mu_1 + \lambda_2 + \lambda_3 + \lambda_4] P_1(S) = \mu_2 P_4(S) + \mu_3 P_5(S) + \mu_4 P_6(S) + \lambda_1 P_0(S) \quad (25)$$

$$[S + \lambda_1 + \lambda_3 + \lambda_4 + \mu_2] P_2(S) = \mu_1 P_4(S) + \mu_3 P_7(S) + \mu_4 P_8(S) + \lambda_2 P_0(S) \quad (26)$$

$$[S + \lambda_1 + \lambda_2 + \lambda_4 + \mu_3] P_3(S) = \mu_1 P_5(S) + \mu_2 P_7(S) + \mu_4 P_9(S) + \lambda_3 P_0(S). \quad (27)$$

$$[S + \mu_1 + \mu_2] P_4(S) = \lambda_1 P_2(S) + \lambda_2 P_1(S) \quad (28)$$

$$[S + \mu_1 + \mu_3] P_5(S) = \lambda_1 p_3(S) + \lambda_3 P_1(S) \quad (29)$$

$$[S + \mu_4] P_6(S) = \lambda_4 P_1(S) \quad (30)$$

$$[S + \mu_2 + \mu_3] P_7(S) = \lambda_2 P_3(S) + \lambda_3 P_2(S) \quad (31)$$

$$[S + \mu_4] p_8 (S) = \lambda_4 P_2(S) \quad (32)$$

$$[S + \mu_4] P_9(S) = \lambda_4 P_3(S) \quad (33)$$

Where S is the Laplace transform variable.

To determine R_S, a verification model is applied. It could be noted that the probabilities of the failed states haven't any effect on the system reliability, so the system reliability could be calculated considering only the working states (i.e., excluding the failed states). Based on this result, the probability of failed states could be neglected during solution of the complex systems and the probabilities of operating states are only considered.

The previous equations (24 to 33) are solved using MATLAB 2015 at the following initial conditions at time t= 0 where,

$$p_i(t) = \begin{cases} 1, & \text{if } i = 0 \\ 0, & \text{if } i \neq 0 \end{cases} \quad (34)$$

After solving these equations, the probabilities of operating states for the system, under consideration, are calculated as follows:

$$P_0 = (C\ A\ B) / D \quad (35)$$

$$P_1 = (\lambda_1\ A\ B) / D \quad (36)$$

$$P_2 = (\lambda_2\ C\ B) / D \quad (37)$$

$$P_3 = (\lambda_3\ C\ A) / D \quad (38)$$

Where:

$$A = \mu_2 + S + \lambda_1 + \lambda_3 + \lambda_4 \quad (39)$$

$$B = \mu_3 + S + \lambda_1 + \lambda_2 + \lambda_4 \quad (40)$$

$$C = \mu_1 + S + \lambda_2 + \lambda_3 + \lambda_4 \quad (41)$$

D= see appendix A (42)

Having the values of probabilities of working states determined, R_S is calculated as follows:

$$R_s(S) = P_0(S) + P_1(S) + P_2(S) + P_3(S) \quad (43)$$

Taking the inverse of Laplace transforms then, P_0, P_1, P_2, and P_3, are calculated as F(t) and the system reliability is calculated at time t as follows:

$$R(t) = P_0(t) + P_1(t) + P_2(t) + P_3(t) \quad (44)$$

3.3. Maintainability Equations

For any system, the system maintainability (M_S) is calculated as follows:

$$M_S(t) = 1 - e^{(-\mu t)} \quad (45)$$

Where(μ) is the repair rate (μ= 1 / *MTTR*), *MTTRs* is a mean time to repair of the system and is calculated as a function in mean time to repair (*MTTR*) and mean time between failure (*MTBF*) of system component i where:

$$MTTR_S = \frac{\sum_{i=1}^{n} MTTRi/MTBFi}{\sum_{i=1}^{n} 1/MTBFi} \quad (46)$$

4. Implementation of Proposed Model

Fig. 3 depicts the block diagram of the real industrial system in Egyptian Petrol Company. This system is consists of two unites of fuel supply connected in parallel with each other; in which the natural gas unit is active and the diesel unit is standby. The fuel supply units are connected in series with four turbines which are connected in parallel with each other (3-out-of-4); three of them are in operating state while the fourth is in the standby state and the system fails when two components (Turbines) fail.

The turbines are considered the most critical items in that system because it is used to operate four plants as shown in the block diagram. Whereas the actual output for each turbine is 3.8 MW and the total power required must be not lower than 11.4 MW; otherwise, the system will stop working which tends to big losses.

The transition diagram of this system is built based on the Markov, as explained previously (in section 2). Table (2) illustrates the number of failures, the repair time, and the operating time of this real system that were collected from historical data during year 2015. These data are applied to validate the proposed model. The RAM analysis and discussions are presented in this section.

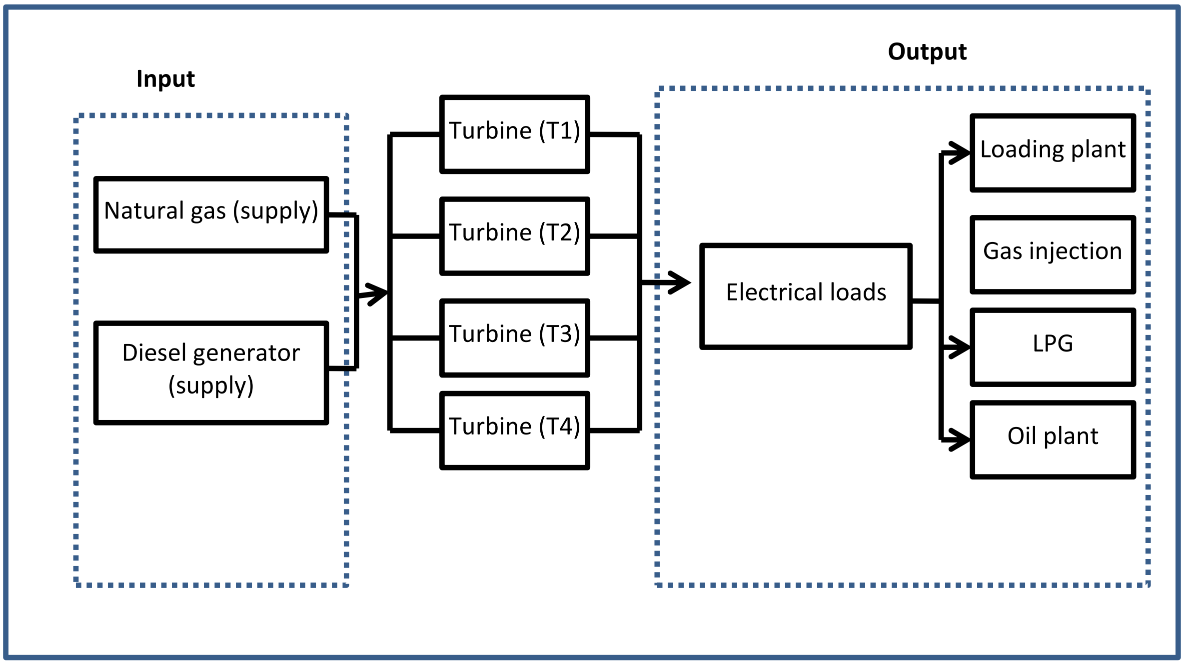

Figure 3: Block diagram of the industrial real system of Egyptian Petrol Company (Turbines of power generation).

The value of the failure rate and repair rate for each turbine is illustrated in Table (3) where:

Failure rate = number of failures / operating time (47)

Repair rate = number of failures/ repair time (48)

As an example for T_1;

Failure rate (λ) = 11/ 6471= 0.0017 (49)

Repair rate (μ) = 11 / 88 = 0.125 (50)

Table 2: The collected historical data of the considered system for year 2015.

	Number of failures	Repair time (hours)	Operating time (hours)
T_1	11	88	6471
T_2	8	53	6509
T_3	6	38	6526
T_4	9	105	6456

Table 3: Failure and repair rates of the considered system.

	T_1	T_2	T_3	T_4
Failure rate (λ)	0.0017	0.0012	0.001	0.0014
Repair rate (μ)	0.125	0.15	0.15	0.08

4.1. System Availability

By substituting values of failure and repair rates in system equations from (Eq.12 to 21) the state probabilities are calculated as a function in P_0 as follows:

P_1= 0.0136 P_0, P_2= 0.008 P_0, P_3= 0.006 P_0,
P_4= 0.000011 P_0, P_5 =0.00001P_0, P_6 =0.0002 P_0
P_7= 0.000005 P_0, P_8 = 0.00014 P_0, P_9 = 0.00001 P_0

Where, P_0 and $_{Ass}$ are calculated from equations (22) and (23) and equal 0.97 and 0.9995 respectively.

4.2. System Reliability

R_S is calculated as follows:

- Substitute about λ and μ from Table (3) in equations (39 to 42), the variables A, B, C and D could be calculated as follows:

A = 10000.0S + 1541.0 (51)

B = 10000.0S + 1543.0 (52)

C = 2500.0(5000.0S + 643.0) (53)

D = ($1.25e^{15}S^4$ + $5.5112e^{14}S^3$ + 8.075e13S^2 + $3.9329e^{12}S$ + $4.1045e^8$) (54)

- Substitute about the variables A, B, C, and D in (eq., 35-38) to get the probability of the working states.
- Taking the inverse Laplace of system reliability (eq., 35 - 38) to get :

P_0 (t) =0.97e $^{(-0.0001t)}$ + 0.015e $^{(-0.15t)}$ + 0.00003e $^{(-0.15t)}$ + 0.01e $^{(-0.13t)}$ (55)

P_1 (t) =0.01e $^{(-0.0001t)}$ - 0.0001 e $^{(-0.15t)}$ – 2 e^{-6}e $^{(-0.15t)}$ – 0.012e $^{(-0.13t)}$ (56)

P_2 (t) =0.0075e $^{(-0.0001t)}$ - 0.007e $^{(-0.15t)}$ - 0.0003e $^{(-0.15t)}$ + 0.0005e $^{(-0.13t)}$ (57)

P_3 (t) =0.006e $^{(-0.0001t)}$ - 0.007e $^{(-0.15t)}$ + 0.0003e $^{(-0.15t)}$ + 0.0004e $^{(-0.13t)}$ (58)

- Substitute about P0, P1, P2 and P3in equation (44) to get RS as follows:

R_s= 0.9935 e $^{(-0.0001t)}$ + 0.0009 e $^{(-0.15t)}$ + 0.000028 e $^{(-0.15t)}$ - 0.0011e $^{(-0.13t)}$ (59)

 © 2018 Jordan Journal of Mechanical and Industrial Engineering. All rights reserved - Volume 12, Number 1 (ISSN 1995-6665)

4.3. System maintainability

$MTTR_s$ is calculated from equation (46) based on the historical data of the system components which is illustrated in Table.2, (i.e., μ_s= 0.1196, $MTTR_S$= 8.36 hr) where,

MTTR= repair time / number of failure (60)

MTBF= 1/ failure rate (61)

So, $MTTR_S = \sum_{i=1}^{4} \underline{((88/11+53/8+38/6+105/9)/(1/0.0017+1/0.0012+1/0.001+1/0.0014))} =$ 8.36 h

$\sum_{i=1}^{4}(0.0017+0.0012+0.001+0.0014)$ (62)

Then the system maintainability at time t is as follows:

$M(t) = 1 - e^{(-0.1196\, t)}$ (63)

5. Results Discussion

An analysis of system performance has been carried out at different values of failure and repair rates of system components. The effects of these values on the system availability, reliability, and maintainability are discussed in the following sections.

5.1. Availability analysis

The A_{SS} was calculated at different values of failure rate and repair rate as follows:

Fig. (4) Shows the effect of failure rate for each turbine on the system availability at different values of failure rate (i.e., λ=0.001, 0.002, 0.003, 0.004, 0.005, 0.006) without changing repair rate values mentioned in Table (3). It could be seen from this Figure that the system availability decreases, slightly, with increasing failure rate of the system component. Moreover, it is observed that turbine (T_4) has the lower availability than the other turbines.

On the other hand Fig. (5) depicts the effect of repair rate for each turbine on system availability at different values of repair rate (i.e., μ=0.06, 0.09, 0.12, 0.15, 0.18, 0.21) without changing failure rate values mentioned in Table (3). It is observed that the system availability increases, slightly, with increasing repair rate of turbines, and (T_4) has the higher availability than the other turbines this because it has the lower value of repair rate. This revealed that increasing the failure rate reduces the availability while increasing the repair rate leads to increasing the availability.

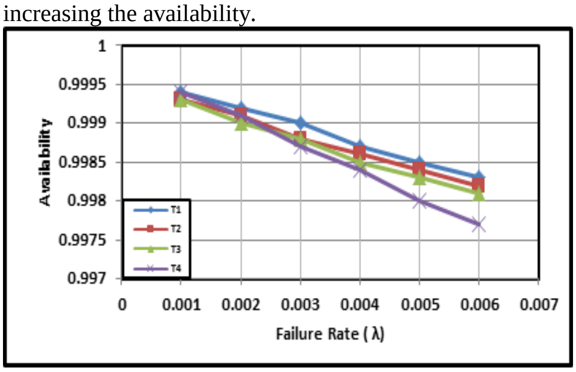

Figure 4: Effect of turbines failure rate (λ) on system availability at steady state.

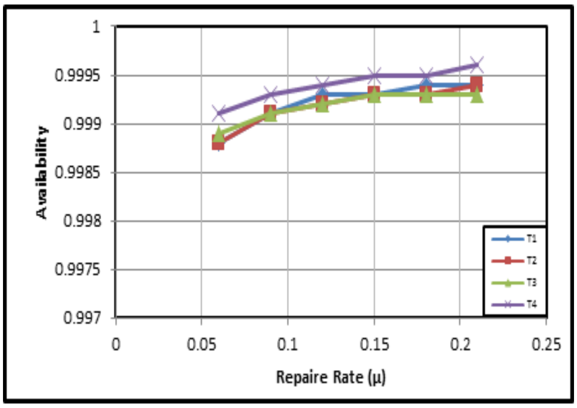

Figure 5: Effect of turbines repair rate (μ) on system availability at steady state.

5.2. Reliability Analysis

Fig. (6), depicts R_S of the system under consideration at real data of λ and μ mentioned previously in Table (3), along operating time and it is concluded that the system reliability decreases with time and the system reliability after 5000 running hours is 0.59%.

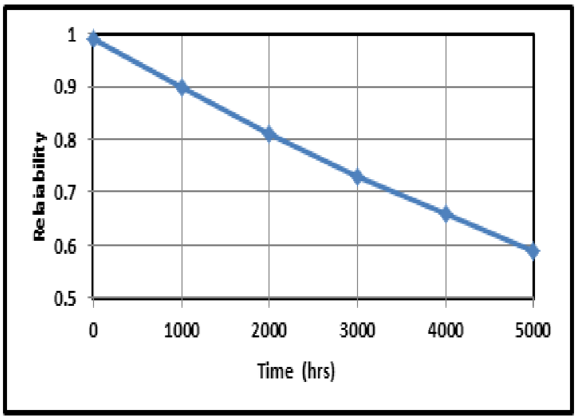

Figure 6: Effect of time on reliability of the system.

To investigate the effect of the failure rate of system components individually on R_S at different mission time, the failure rate of each turbine is changed within range (0.001 to 0.006 with incremental value 0.001) while, the values of rapier rates for all turbines and failure rates of the other turbines are the same real data.

Fig. (7), Illustrates the criticality of the system components, i.e., which turbine decreases R_S. It could be noted with comparing the cases of (λ = 0.001) for each turbine that T_3 has the higher effect on the system reliability and therefore it is the critical component as shown in Fig. (7-a), furthermore, with increasing λ to 0.006 for the same cases, it is also still the critical one as shown in Fig (7-b).

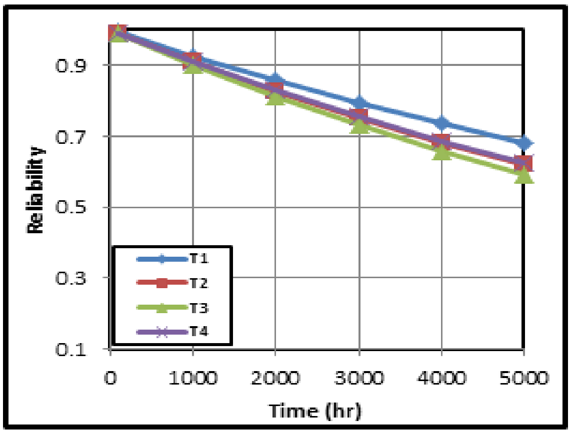

(a) λ =0.001

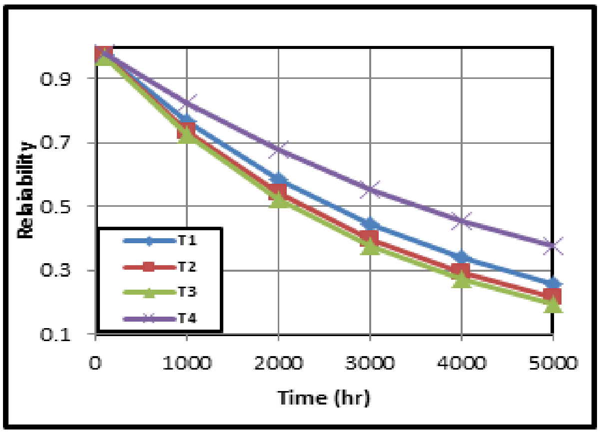

b: λ =0.006

Figure 7:(a) and (b) Effect of failure rate (λ) on the system reliability at transient state.

5.3. Maintainability Analysis

Fig. (8) Illustrates the maintainability of each turbine as well as *Ms* of the overall system at real data along first 100 operating hours. It could be seen that the maintainability of T_4 is lower than the maintainability of the other components; this is due to the lower value of its repair rate than the others.

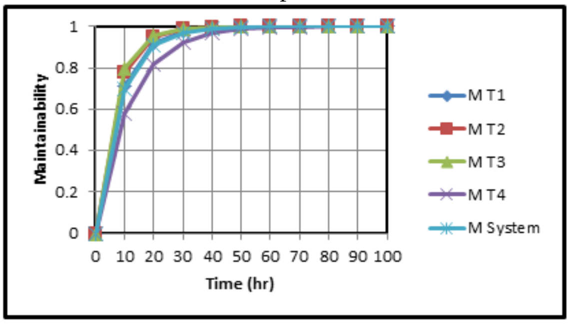

Figure 8: Maintainability of each turbine and the overall system versus time.

To investigate the effect of repair rate of overall system on *Ms* along the first 100 hrs of operating time, the repair rate of the system is assumed within range (0.0 to 0.21 with incremental value 0.03) as shown in Fig. (9). It could be seen that the increase in the system repair rate increases *Ms*.

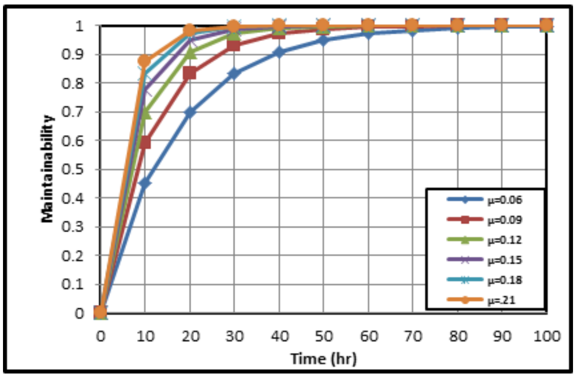

Figure 9: Effect of Repair Rate on Maintainability of the Overall System at Different Mission Time.

6. Conclusion

A RAM model of a 3-out-of-4 system has been proposed based on the Markovian approach. Availability at steady state, reliability at transient state and maintainability equations have been formulated. A real data of Oil Gas Egyptian Company was applied to obtain the system reliability, availability, and maintainability. A parametric investigation of various values of system failure and repair rates on system reliability, availability, and maintainability, as well as their effects on the system performance, are presented. The finding of this study could be concluded as follows:

- The proposed RAM model could be used as an integrated model, to investigate system reliability, availability, and maintainability of 3-out-of-4 system.
- It could be also used to determine the most critical component of the system.
- The proposed model helps maintenance engineers and designers to evaluate the system performance and carried out modification.
- The implementation of the proposed model revealed that the system availability at steady state is 99%, and the system maintainability is 0.99% but the system reliability after 5000 running hours is 0.59%. This means that, an enhancement required improving the system reliability and reducing the system down time. It is observed that T_3 is the most critical component in the system and need special attention with careful observation to reduce it's down time and increase the system performance.

References

[1] S. Saraswat and G.S. Yadava, "An overview on reliability, availability, maintainability and supportability (RAMS) engineering", International Journal of Quality & Reliability Management Vol. 25 No. 3, 2008, 330-344.

[2] D. Sanctis, C. Paciarotti, and O. D. Giovine, "Integration between RCM and RAM: a case study", International Journal of Quality & Reliability Management, Vol. 33 Issue: 6, 2016, 852-880.

[3] F. Corvaro, G. Giacchetta, B. Marchetti, and M. Recanati, "Reliability, Availability, Maintainability (RAM) study, on reciprocating compressors API 618 Petroleum", Vol. 3, 2017, 266-272.

[4] M. Aoudia, O. Belmokhtar, G. Zwingelstein, "Economic impact of maintenance management ineffectiveness of an oil and gas company", Journal of Quality in Maintenance Engineering, Vol. 14, 2008, 237-261.
[5] R. K. Sharma, and S. Kumar, “Performance modelling in critical engineering systems using RAM analysis”, Reliability Engineering & System Safety, Vol.93, Issue 6, 2008, 913–919.
[6] Komala, S.P. Sharma, and D. Kumar, “RAM analysis of repairable industrial systems utilizing uncertain data’, Applied Soft Computing, Vol. 10, 2010, 1208–1221.
[7] S. K. Rajiv, and S. Pooja, “Computing RAM Indices For Reliable Operation of Production Systems”, Advances in Production Engineering & Management, Vol. 7, 2012, 245-254.
[8] R. Khanduja, P.C. Tewari, R.S.Chauhan, and D. Kumar, “Mathematical Modeling and Performance Optimization for the Paper Making System of a Paper Plant”, Jordan Journal of Mechanical and Industrial Engineering, Vol. 4 No 4, 2010, 487 – 494.
[9] M. Kumar, V. Modgil, and V.Singla, “Mathematical Modelling and Availability Analysis of Packaging Section in a Paint Industry: A Case Study”, International Journal of Engineering Technology Science and Research, Vol. 2, 2015, 179 – 185.
[10] S. Gupta, P. C. Tewari, and A. Sharma, ”A probabilistic model for performance evaluation of steam and water system of a thermal power plant”, International Journal of Management Science and Engineering Management, Vol. 4 No.3, 2009,177-187.
[11] Aggarwal, S. Kumar, V. Singh, “Mathematical modelling and fuzzy availability analysis for serial processes in the crystallization system of a sugar plant”, Journal of Industrial Engineering International, Vol.13, 2017, 47–58.
[12] J. Lin, J. Pulido, M. Asplund, “ Reliability analysis for preventive maintenance based on classical and Bayesian semi-parametric degradation approaches using locomotive wheel-sets as a case study”, Reliability Engineering and System Safety, Vol. 134, 2015, 143–156.
[13] P. Singh and A. Goyal,” Behaviour Analysis of a Biscuit Making Plant using Markov Regenerative Modelling”, International Journal on Theoretical and Applied Research in Mechanical Engineering (IJTARME), Volume-2, 2013, 2319 – 3182.
[14] I.Yusuf, and N. Hussaini,’ Evaluation of Reliability and Availability Characteristics of 2-out of -3 Standby System under a Perfect Repair Condition”, American Journal of Mathematics and Statistics, Vol. 2, 2012, 14-119.
[15] Yusuf, and F. Koki,” Analysis of Stochastic Reliability Characteristics of a Repairable 2-out-of-3 System with Minimal Repair at Failure”, Applied Mathematics, Vol. 4, 2013, 1115-1124.
[16] Preeti,” Analysis of a Linear Consecutive k-out-of-N System with Common Cause Shock Failure”, International Journal of Technology Innovations and Research (IJTIR), Vol.16, 2015.
[17] Yusuf, ”Availability and Profit Analysis of 3-out-of-4 Repairable System with Preventive Maintenance”, International Journal of Applied Mathematical Research, Vol. 1(4), 2012, 510-519.
[18] Elsayed A. Elsayed, “Reliability Engineering 2nd Edition”, John Wiley & Sons, Hoboken, United States, 2012.

Appendix (A)

$$
\begin{aligned}
D= (&\mu_1 S^3 + \mu_2 S^3 + \mu_3 S^3 + S \lambda_1^3 + 3.0S^3 \lambda_1 + S \lambda_2^3 + 3.0S^3 \lambda_2 + S \lambda_3^3 + 3.0S^3 \lambda^3 + S \lambda_4^3 + 3.0S^3 \lambda^4 + \lambda_1 \lambda_2^3 + \lambda_1^3 \\
&\lambda^2 + \lambda_1 \lambda_3^3 + \lambda_1^3 \lambda_3 + \lambda_1 \lambda_4^3 + \lambda_2 \lambda_3^3 + \lambda_1^3 \lambda_4 + \lambda_2^3 \lambda_3 + \lambda_2 \lambda_4^3 + h_2^3 \lambda_4 + \lambda_3 \lambda_4^3 + \lambda_3^3 \lambda_4 + S^4 + 3.0S^2 \lambda_1^2 + 3.0S^2 \lambda_2^2 \\
&+ 3.0S^2 \lambda_3^2 + 3.0S^2 \lambda_4^2 + 2.0 \lambda_1^2 \lambda_2^2 + 2.0 \lambda_1^2 \lambda_3^2 + 2.0 \lambda_1^2 \lambda_4^2 + 2.0 \lambda_2^2 h_3^2 + 2.0 \lambda_2^2 \lambda_4^2 + 2.0 \lambda_3^2 \lambda_4^2 + \mu_1\mu_2 S^2 + \\
&\mu_1\mu_3 S^2 + \mu_2\mu_3 S^2 + \mu_1 S \lambda_1^2 + 2.0 \mu_1 S^2 \lambda_1 + \mu_1 S \lambda_2^2 + 2.0 \mu_1 S^2 \lambda_2 + \mu_2 S \lambda_1^2 + 2.0 \mu_2 S^2 \lambda_1 + \mu_1 S \lambda_3^2 + 2.0 \mu_1 S^2 \lambda_3 + \\
&\mu_2 S \lambda_2^2 + 2.0 \mu_2 S^2 \lambda_2 + \mu_3 S \lambda_1^2 + 2.0 \mu_3 S^2 \lambda_1 + \mu_1 S \lambda_4^2 + 2.0 \mu_1 S^2 \lambda_4 + \mu_2 S \lambda_3^2 + 2.0 \mu_2 S^2 \lambda_3 + \mu_3 S \lambda_2^2 + 2.0 \mu_3 S^2 \lambda_2 \\
&+ \mu_2 S \lambda_4^2 + 2.0\mu_2 S^2 \lambda_4 + \mu_3 S \lambda_3^2 + 2.0 \mu_3 S^2 \lambda_3 + \mu_3 S \lambda_4^2 + 2.0 \mu_3 S^2 \lambda_1 + \mu_1 \lambda_1 \lambda_2^2 + \mu_1 \lambda_1^2 \lambda_2 + \mu_1 \lambda_1 \lambda_3^2 + \mu_1 \lambda_1^2 \lambda_3 \\
&+ \mu_2 \lambda_1 \lambda_2^2 + \mu_2 \lambda_1^2 \lambda_2 + \mu_1 \lambda_2 \lambda_3^2 + \mu_1 \lambda_2^2 \lambda_3 + \mu_2 \lambda_1 \lambda_3^2 + \mu_2 \lambda_1^2 \lambda_3 + \mu_3 \lambda_1 \lambda_2^2 + \mu_3 \lambda_1^2 \lambda_2 + \mu_1 \lambda_2 \lambda_4^2 + \mu_1 \lambda_2^2 \lambda_4 + \\
&\mu_2 \lambda_1 \lambda_4^2 + \mu_2 \lambda_2 \lambda_3^2 + \mu_2 \lambda_1^2 \lambda_4 + \mu_2 \lambda_2^2 \lambda_3 + \mu_3 \lambda_1 \lambda_3^2 + \mu_3 \lambda_1^2 \lambda_3 + \mu_1 \lambda_3 \lambda_4^2 + \mu_1 \lambda_3^2 \lambda_4 + \mu_3 \lambda_1 \lambda_4^2 + \mu_3 \lambda_2 \lambda_3^2 + \mu_3 \\
&\lambda_1^2 \lambda_4 + \mu_3 \lambda_2^2 \lambda_3 + \mu_2 \lambda_3 \lambda_4^2 + \mu_2 \lambda_3^2 \lambda_4 + \mu_3 \lambda_2 \lambda_4^2 + \mu_3 \lambda_2^2 \lambda_4 + 5.0S \lambda_1 \lambda_2^2 + 5.0S \lambda_1^2 \lambda_2 + 7.0S^2 \lambda_1 \lambda_2 + 5.0S \lambda_1 \lambda_3^2 \\
&+ 5.0S \lambda_1^2 \lambda_3 + 7.0S^2 \lambda_1 \lambda_3 + 5.0S \lambda_1 \lambda_4^2 + 5.0S \lambda_2 \lambda_3^2 + 5.0S \lambda_1^2 \lambda_4 + 5.0S \lambda_2^2 \lambda_3 + 7.0S^2 \lambda_1 \lambda_4 + 7.0S^2 \lambda_2 \lambda_3 + 5.0S \\
&\lambda_2 \lambda_4^2 + 5.0S \lambda_2^2 \lambda_4 + 7.0S^2 \lambda_2 \lambda_4 + 5.0S \lambda_3 \lambda_4^2 + 5.0S \lambda_3^2 \lambda_4 + 7.0S^2 \lambda_3 \lambda_4 + 4.0 \lambda_1 \lambda_2 \lambda_3^2 + 4.0 \lambda_1 \lambda_2^2 \lambda_3 + 4.0 \lambda_1^2 \lambda_2 \\
&\lambda_3 + 4.0 \lambda_1 \lambda_2 \lambda_4^2 + 4.0 \lambda_1 \lambda_2^2 \lambda_4 + 4.0 \lambda_1^2 \lambda_2 \lambda_4 + 4.0 \lambda_1 \lambda_3 \lambda_4^2 + 4.0 \lambda_1 \lambda_3^2 \lambda_4 + 4.0 \lambda_1^2 \lambda_3 \lambda_4 + 4.0 \lambda_2 \lambda_3 \lambda_4^2 + 4.0 \lambda_2 \\
&\lambda_3^2 \lambda_4 + 4.0 \lambda_2^2 \lambda_3 \lambda_4 + \mu_1 \mu_2 \mu_3 S + \mu_1\mu_2 S \lambda_1 + \mu_1 \mu_2 S \lambda_1 + \mu_1 \mu_3 S \lambda_1 + \mu_1 \mu_2 S \lambda_3 + \mu_1 \mu_3 S \lambda_2 + \mu_2 \mu_3 S \lambda_1 + \mu_1 \mu_2 S \lambda_4 + \\
&\mu_1 \mu_3 S \lambda_3 + \mu_2 \mu_3 S \lambda_2 + \mu_1 \mu_3 S \lambda_4 + \mu_2 \mu_3 S \lambda_3 + \mu_2 \mu_3 S \lambda_4 + \mu_1 \mu_2 \lambda_1 \lambda_3 + \mu_1 \mu_3 \lambda_1 \lambda_2 + \mu_1 \mu_2 \lambda_2 \lambda_3 + \mu_2 \mu_3 \lambda_1 \lambda_2 + \mu_1 \mu_3 \lambda_2 \\
&\lambda_3 + \mu_2 \mu_3 \lambda_1 \lambda_3 + \mu_1 \mu_2 \lambda_3 \lambda_4 + \mu_1 \mu_3 \lambda_2 \lambda_4 + \mu_2 \mu_3 \lambda_1 \lambda_4 + 3.0 \mu_1 S \lambda_1 \lambda_2 + 3.0 \mu_1 S \lambda_1 \lambda_3 + 3.0 \mu_2 S \lambda_1 \lambda_2 + 2.0 \mu_1 S \lambda_1 \\
&\lambda_4 + 3.0 \mu_1 S \lambda_2 \lambda_3 + 3.0 \mu_2 S \lambda_1 \lambda_3 + 3.0 \mu_3 S \lambda_1 \lambda_2 + 3.0 \mu_1 S \lambda_2 \lambda_4 + 3.0 \mu_2 S \lambda_1 \lambda_4 + 3.0 \mu_2 S \lambda_2 \lambda_3 + 3.0 \mu_3 S \lambda_1 \lambda_3 + 3.0 \\
&\mu_1 S \lambda_3 \lambda_4 + 2.0 \mu_2 S \lambda_2 \lambda_4 + 3.0 \mu_3 S \lambda_1 \lambda_4 + 3.0 \mu_3 S \lambda_2 \lambda_3 + 3.0 \mu_2 S \lambda_3 \lambda_4 + 3.0 \mu_3 S \lambda_2 \lambda_4 + 2.0 \mu_3 S \lambda_3 \lambda_4 + 2.0 \mu_1 \lambda_1 \lambda_2 \\
&\lambda_3 + 2.0 \mu_1 \lambda_1 \lambda_2 \lambda_4 + 2.0 \mu_2 \lambda_1 \lambda_2 \lambda_3 + 2.0 \mu_1 \lambda_1 \lambda_3 \lambda_4 + 2.0 \mu_2 \lambda_1 \lambda_2 \lambda_4 + 2.0 \mu_3 \lambda_1 \lambda_2 \lambda_3 + 2.0 \mu_1 \lambda_2 \lambda_3 \lambda_4 + 2.0 \mu_2 \lambda_1 \lambda_3 \\
&\lambda_4 + 2.0 \mu_3 \lambda_1 \lambda_2 \lambda_4 + 2.0 \mu_2 \lambda_2 \lambda_3 \lambda_4 + 2.0 \mu_3 \lambda_1 \lambda_3 \lambda_4 + 2.0 \mu_3 \lambda_2 \lambda_3 \lambda_4 + 11.0S \lambda_1 \lambda_2 \lambda_3 + 11.0S \lambda_1 \lambda_2 \lambda_4 + 11.0S \lambda_1 \lambda_3 \\
&\lambda_4 + 11.0S \lambda_2 \lambda_3 \lambda_4 + 9.0 \lambda_1 \lambda_2 \lambda_3 \lambda_4)
\end{aligned}
$$

المملكة الأردنية الهاشمية

الجامعة الهاشمية

المجلة الأردنية
للهندسة الميكانيكية والصناعية

JJMIE

مجلة علمية عالمية محكمة

تصدر بدعم من صندوق البحث العلمي

http://jjmie.hu.edu.jo/

ISSN 1995-6665

المجلة الأردنية للهندسة الميكانيكية والصناعية

مجلة علمية عالمية محكمة

المجلة الأردنية للهندسة الميكانيكية والصناعية: مجلة علمية عالمية محكمة تصدر عن الجامعة الهاشمية بالتعاون مع صندوق دعم البحث العلمي في الأردن

ترسل البحوث إلى العنوان التالي

رئيس تحرير المجلة الأردنية للهندسة الميكانيكية و الصناعية

الجامعة الهاشمية

كلية الهندسة

قسم الهندسة الميكانيكية

الزرقاء - الأردن

هاتف : 3903333 5 00962 فرعي 4217

Email: jjmie@hu.edu.jo

Website: www.jjmie.hu.edu.jo